DISS. ETH NO. 21531

Catalysis Under Extreme Conditions: in situ Studies of the Reforming of Organic Key Compounds in Supercritical Water

A dissertation submitted to

ETH ZURICH

for the degree of

Doctor of Sciences

presented by

MARIAN DREHER

Diplom-Chemiker, Universität Konstanz

born on January 15, 1983

citizen of Germany

accepted on the recommendation of

Prof. Alexander Wokaun

Prof. Christophe Copéret

Prof. Frédéric Vogel

Dr. Maarten Nachtegaal

2013

Für meine Familie,

in Dankbarkeit für 30 Jahre Unterstützung, Vertrauen und Liebe.

„Bemüht euch nicht um das Trügerische, nicht um Besitz, nicht um Titel: Das wird mit den Nerven bezahlt, in Jahrzehnten erworben und in einer einzigen Nacht konfisziert. Lebt in ruhiger Überlegenheit gegenüber dem Leben – fürchtet nicht das Unglück und sehnt euch nicht nach Glück ‚s ist ja einerlei.“

Alexander Solschenizyn, Der Archipel Gulag

Abstract of this thesis

Chemistry in supercritical water (SCW) plays an increasingly important role in waste and energy conversion technologies presently under development. Examples for such processes are the supercritical water oxidation (SCWO) for the destruction of toxic wastes and the hydrothermal gasification of biomass, producing methane and hydrogen. The catalytic hydrothermal gasification of biomass – a process being developed at PSI – aims at producing a methane-rich product gas (synthetic natural gas, SNG) at low temperatures and is a prime example for catalysis in supercritical water. The efficiency of this process is currently limited by catalyst deactivation, mainly due to sulfur poisoning and fouling of the catalyst. Regeneration protocols will be necessary to enhance catalysts lifetime and therefore increase the overall process efficiency. Meeting these challenges requires a detailed understanding of reaction mechanisms at the interface between catalyst support, catalyst surface and reaction medium.

The presented study aims at providing a fundamental understanding of the structure of ruthenium catalysts and reaction mechanisms under hydrothermal conditions, without which a knowledge-based approach to challenges like catalyst poisoning and regeneration of deactivated catalysts is not possible. Studying catalysis under SCW conditions is complicated by demanding experimental requirements and the need of applying spectroscopic methods with a sensitivity sufficient for probing the active phase of the catalyst, adsorbed species and possibly reaction intermediates. Thanks to the penetration depth of hard X-rays, X-ray absorption spectroscopy (XAS) is a powerful method for the determination of the electronic and geometric structure of nano-sized metal clusters under supercritical water conditions.

A tubular, continuous flow reactor, made of ceramic aluminum nitride, was designed to perform in situ XAS under SCW conditions. The aluminum nitride tube allowed for sufficient X-ray transmission to enable acquisition of extended X-ray absorption fine structure (EXAFS) spectra of a ruthenium catalyst during the hydrothermal gasification of organic model compounds. From these spectra, structural information about catalyst composition and particle size could be derived. This structural analysis was combined with electronic structure calculations, obtained from density functional theory, and isotope labeling of

reactants and reaction products in order to establish structure-performance relationships for both active and sulfur poisoned catalysts.

The combined results from XAS and isotope labeling show that the active phase of the Ru catalyst under reaction conditions is metallic, nano-sized Ru with an average particle size of 1.5 nm. The methanation reaction in SCW, vital for the production of SNG, proceeds via direct hydrogenation of (hydro-) carbon adsorbates on the Ru surface instead of the classic methanation pathway via carbon monoxide and hydrogen. These adsorbates are formed from the complete degradation of organic compounds on the active catalyst.

Upon sulfur poisoning, the Ru surface was covered by irreversibly adsorbed sulfide species with a surface coverage of about 40%. This affected the formation of the (hydro-) carbon adsorbates on the Ru catalyst by diminishing its ability for biomass degradation via C-C, C-H and C-O bond breaking. Sulfur poisoning further affected the abundance of these adsorbates on the catalyst's surface and as a result the selectivity of the methanation reaction.

Based on the in situ XAS studies, protocols for an efficient removal of sulfur from the poisoned catalyst were developed. A liquid-phase oxidation of the sulfur poisoned catalyst at mild conditions was developed using hydrogen peroxide as an oxidizing agent. This treatment successfully removed sulfur from the catalyst's surface, restoring the active catalyst phase, and shows promising potential for catalyst regeneration.

In conclusion, mechanistic details of the conversion of organic compounds to methane in supercritical water could be clarified. This was largely supported by the development of a reactor that allows for in situ EXAFS studies under these conditions. The structural data was augmented by concomitant isotope labeling experiments, in combination with structure calculations, to provide a multi-facetted understanding of catalyst structure and catalytic reaction mechanisms. It is expected that the gained knowledge will help to further advance chemistry and conversion processes in hydrothermal media.

Kurzfassung

Chemische Reaktionen in überkritischem Wasser (SCW) spielen eine immer grössere Rolle in Abfall- und Energieumwandlungsprozessen, die gegenwärtig entwickelt werden. Beispiele für solche Prozesse sind die Oxidation in überkritischem Wasser (SCWO) zur Beseitigung von Giftmüll und die hydrothermale Vergasung von Biomasse zur Produktion von Methan und Wasserstoff. Die katalytische, hydrothermale Vergasung von Biomasse – ein Prozess, der am PSI entwickelt wird – hat die Herstellung eines Produktgases mit hohem Methananteil (synthetisches Erdgas, SNG) bei niedrigen Temperaturen zum Ziel und ist ein hervorragendes Beispiel für Katalyse in überkritischem Wasser. Die Effizienz dieses Prozesses wird derzeit durch Katalysatordeaktivierung limitiert, hauptsächlich aufgrund von Schwefelvergiftung und Verkokung des Katalysators. Methoden, die den Katalysator regenieren sind notwendig um die Standzeit und somit die generelle Prozesseffizienz zu erhöhen. Um diesen Herausforderungen zu begegnen sind detaillierte, mechanistische Untersuchungen an der Schnittstelle zwischen Katalysatorträger, Katalysatoroberfläche und Reaktionsmedium nötig.

Die vorgestellte Studie zielt darauf ab, ein grundlegendes Verständnis der Struktur von Rutheniumkatalysatoren und der Reaktionsmechanismen unter hydrothermalen Bedingungen bereit zu stellen, ohne das wissensbasierte Lösungsansätze für Herausforderungen wie Katalysatorvergiftung und der Regenerierung von deaktivierten Katalysatoren nicht möglich sind. Katalytische Reaktionen unter SCW Bedingungen zu untersuchen wird jedoch durch die anspruchsvollen experimentellen Voraussetzungen erschwert. Zudem sind spektroskopische Methoden nötig, die empfindlich genug sind um die aktive Phase des Katalysators, adsorbierte Spezies und mögliche Zwischenprodukte zu untersuchen. Dank der Eindringtiefe von harter Röntgenstrahlung ist Röntgenabsorptionsspektroskopie (XAS) eine hervorragende Methode um die elektronische und räumliche Stuktur von metallischen Nanopartikeln unter extremen Reaktionsbedingungen zu bestimmen.

Ein rohrförmiger, kontinuierlich operierender Reaktor aus Aluminiumnitrid-Keramik wurde entwickelt um in situ XAS in überkritischem Wasser durchzuführen. Das Rohr aus Aluminiumnitrid ermöglichte eine ausreichende Röntgentransmission um

Röntgenfeinstrukturspektren (EXAFS) eines Rutheniumkatalysators während der hydrothermalen Vergasung von organischen Modellsubstanzen aufzunehmen. Aus diesen Spektren konnten Informationen über Katalysatorzusammensetzung und Partikelgrösse ermittelt werden. Diese Strukturanalyse wurde mit Strukturberechnungen, basierend auf der Dichtefunktionaltheorie, und Isotopenmarkierung von Reaktanden und Reaktionsprodukten kombiniert um Struktur-Aktivität-Beziehungen für aktive und schwefelvergiftete Katalysatoren zu erhalten.

Die Ergebnisse zeigen, dass die aktive Phase des Ru Katalysators unter Reaktionsbedingungen metallisches, nanopartikuläres Ruthenium ist, mit einer durchschnittlichen Partikelgrösse von 1.5 nm. Die Methanierungsreaktion in überkritischem Wasser, notwendig für die Erzeugung von SNG, läuft über eine direkte Hydrierung der adsorbierten Kohlenwasserstoffspezies auf der Rutheniumoberfläche ab, anstatt über den klassischen Reaktionsweg mit Kohlenmonoxid und Wasserstoff als Zwischenprodukte. Diese adsorbierten Spezies werden durch den vollständigen Zerfall von organischen Verbindungen auf der Katalysatoroberfläche gebildet.

Im Zuge der Schwefelvergiftung wurde die Rutheniumoberfläche zu ungefähr 40% Oberflächenbelegung mit irreversibel adsorbiertem Sulfid bedeckt. Dies beeinflusste die Bildung der Kohlenwasserstoffadsorbate auf dem Katalysator indem dessen Fähigkeit, Biomasse durch C-C, C-H und C-O Bindungsbrüche aufzubrechen, verringert wurde. Desweiteren veränderte die Schwefelvergiftung die Häufigkeit der Oberflächenadsorbate und somit die Selektivität der Methanierungsreaktion.

Basierend auf den in situ XAS Untersuchungen wurden Methoden entwickelt für eine effektive Entfernung des adsorbierten Schwefels von der Katalysatoroberfläche. Mit Wasserstoffperoxid als oxidierendem Agens wurde eine Flüssigphasenoxidation des schwefelvergifteten Katalysators unter milden Bedingungen erzielt. Diese Behandlung entfernte erfolgreich den adsorbierten Schwefel von der Katalysatoroberfläche, stellte die aktive Phase wieder her und zeigte vielversprechendes Potential für die Regenerierung des Katalysators.

Schlussendlich konnten mechanistische Details der Umwandlung von organischen Verbindungen zu Methan in überkritischem Wasser aufgeklärt werden. Dies wurde vornehmlich durch die Entwicklung eines Reaktors ermöglicht, der es erlaubt unter diesen

Bedingungen in situ EXAFS Untersuchungen durchzuführen. Die Strukturdaten wurden durch Isotopenmarkierungsexperimente in Verbindung mit Strukturberechnungen komplementiert um ein vielseitiges Verständnis von Katalysatorstruktur und katalytischen Reaktionsmechanismen zu ermöglichen. Es wird davon ausgegangen, dass das erhaltene Wissen helfen wird, chemische Reaktionen und Umwandlungsprozesse in hydrothermalen Medien weiter zu entwickeln.

Acknowledgements

I thank Prof. Alexander Wokaun for accepting me as a PhD student in his department, for refereeing this work and for the instructive discussions during our quarterly meetings. I thank Prof. Christophe Copéret for co-refereeing this thesis.

Fredi and Jörg, thank you for supervising me and especially for entrusting me with so much freedom to develop and follow my own ideas in this project.

Thank you, Maarten, for showing me my way around the beamline and for supervising and teaching me with frankness, bluntness and good humor. I always appreciated our discussions about work and particularly about everything beyond.

Erich, I think it goes without saying that your help and knowledge were a major contribution to the success of this research project. Thank you so much for being virtually always available and for generally being such a great character.

Gisela, thank you for dealing with all the paperwork I created, the chats we had in your office and for always creating a very hospitable and kind atmosphere around yourself.

I'm indebted to Marcel Hottiger, Jörg Schneebli and Peter Hottinger for helping me out countless times and for giving me advice, often on such short notice.

Thomas Huthwelker is thanked for data acquisition at the PHOENIX beamline, Albert Schuler for ICP-OES measurements and Frank Krumeich from ETH for providing TEM micrographs.

I'm grateful for the good times in- and outside of PSI, for countless coffees, beers, laughs and discussions with: Evalyn Alayon, Martin Brandenberger, Simon Maurer, Johann Regler, Tilman Schildhauer, Martin Schubert, Vera Tschedanoff, Sinan Teske and Marco Wellinger.

Gael, thank you for the good times in our office, coffee on the roof and beer by the Rhine. It was great to work with someone who has the same mindset when it comes to life outdoors and I won't forget our climbs in the Jura and the Alps.

Marcelo Kaufman Rechulski, thank you for being such a great friend and for offering your help when I needed it. And what happens when the police catch you with a beer on the street?

Christian König, thank you for the gin, the minimal beats and our lengthy discussions about the hopelessness of it all. You might not believe this, but I did learn quite a few things from you, too.

Claudio, Fede, Hanna, Konstanze, Kunal, Luca, Lucio, Nora, Ruth, Salvatore, Tina, Tim: thank you for our adventures in the mountains, the drinks and the laughter and for being there in the great times and the bad times.

Jaime Gomez Diaz, there are no words. I miss you.

Contents

Chapter 1

Introduction

The term “biomass” refers to all material from living, or recently living organisms, most often referring to plants or plant-derived materials. As a renewable energy source, biomass can either be used directly – e.g. in the combustion of wood – or indirectly via conversion into another energy carrier such as biofuels (e.g. liquid bio-oils or a methane rich product gas). Biomass and wet biomass in particular, such as agricultural residues, food processing wastes, waste water and, more recently, aquatic cultures (algae), is considered to play a major role in our future sustainable energy supply. Given that a proper conversion technology is used, the production of biofuels from these materials proves to be sustainable, meaning that the energy content of the produced biofuel exceeds the amount of energy consumed in the conversion process. Focusing on residual and waste biomass is required in order achieve a sustainable energy supply by avoiding the competition between food and energy crops. A rough estimate of the yearly energy potential of these types of biomass is presented in Table 1.1. The numbers suggest that about 30% of conventional fuels for primary energy production could be replaced by waste biomass in 2050 (based on the total fuel consumption in 2004). However, since additional conversion processes are necessary to convert biomass to typical liquid or gaseous fuels (e.g. methane, Fischer-Tropsch diesel, ethanol), an upper limit of about 15% seems more realistic.[1]

Since raw biomass typically contains high amounts of water (one exception being wood), a processing route for dry biomass would consume large amounts of energy due to the necessary removal of water prior to processing. As an alternative to dry conversion technologies, hydrothermal processing does not require dry biomass and shows great potential for producing bio-fuels and bio-chemicals from various types of biomass.[1,2] Typically, hydrothermal conditions involve the use of water as a reaction medium at high pressures and temperatures, often reaching the supercritical state of water. Catalysts are being used successfully to lower reaction temperatures in these processes and to control product selectivity. However, a fundamental understanding of (catalytic) reaction mechanisms under these conditions is lacking, mostly due to the highly challenging reaction

parameters (pressure and temperature) that complicate the study of catalyst structure and reaction mechanisms under realistic process conditions.

Biomass	**World**	**Europe**	**Asia**	**North America**
crop harvest residue	49-69	6-8	9-12	5-10
crop process residue	16	1	9	1
wood residue/waste	30	8	7	10
manure	18-22	3	5	3-4
total	**113-137**	**18-20**	**30-33**	**19-25**

***Table 1.1**: Estimated energetic potential of waste biomass from agriculture and forestry in 2050 in EJ/yr.*[1]

This work presents methods to study catalyst structure and surface reactions during the catalytic conversion of organic compounds to methane in supercritical water. The attained fundamental understanding of chemistry and catalysis under these conditions provides a platform for a knowledge-based approach to understand reaction mechanisms and to meet challenges like catalyst poisoning and catalyst regeneration under hydrothermal conditions. This knowledge will help to develop advanced materials for the hydrothermal conversion of biomass and other hydrothermal processes.

1.1 Hydrothermal biomass conversion

Several reviews have been published in the last years that give an excellent overview on the state of the art in hydrothermal biomass processing.[1,3–9] Here, only the main aspects will be discussed.

Hydrothermal processing of biomass can yield either chemicals or fuels, depending on the chosen reaction conditions.[3,4] Typically, chemicals are obtained in sub-critical water via conversion of biomass in the presence of acid or base catalysts, e.g. lactic acid and acrolein from glycerol[10,11] or aldehydes and furan derivatives from the dehydration of polyols.[12] In these reactions, catalytic amounts of sulfuric acid or metal sulfates (< 0.1 wt%) are used to facilitate biomass conversion and control product selectivity.

So-called bio-oil or bio-crude, precursors for liquid biofuels, can be obtained from hydrothermal biomass conversion at sub-critical conditions, generally by biomass liquefaction in the presence of alkaline catalysts.[3] For example, long chain alkanes can be obtained by hydrolysis of fats to release the fatty acids in subcritical water,[13] followed by the decomposition of fatty acids to alkanes in the presence of NaOH or KOH in supercritical water.[14] A low viscosity oil, containing mainly alkenes and C_9-C_{16} alkanes, was obtained by treating crude glycerol (a by-product of the biodiesel production from plant oil) in supercritical water in the presence of NaOH.[15] The hydrothermal liquefaction of microalgae, a group of aquatic organisms that receives increasing attention as a potential energy crop, also shows promising results in the production of bio-oils. Under subcritical conditions, microalgae can be converted to bio-oil with high yields, using heterogeneous metal catalysts or dissolved alkaline catalysts such as NaOH and Na_2CO_3.[16,17]

For generating gaseous fuels, the hydrothermal gasification of biomass takes place at higher temperatures in supercritical water, yielding either a hydrogen or methane rich fuel gas. If hydrogen is the desired product, the gasification is typically carried out at temperatures higher than 600°C.[3,4,18] At lower temperatures, a methane rich product gas is obtained, so-called synthetic natural gas (SNG).[1,3,19,20] However, catalysts are required to obtain high conversion rates under these conditions.

The concept of hydrothermal gasification is a promising route for the conversion of most kinds of wet biomass streams such as manure, sewage sludge and wet agricultural and forestry residues. It utilizes and energetically upgrades biomass feedstocks that are unfit for dry gasification processes due to their high water content and the associated energy loss due to water evaporation. Unlike anaerobic digestion, it fully converts all organic feedstock, leaving only trace residues. Thus, this process combines energy conversion with waste treatment and water purification.

The hydrothermal gasification process, under development at the Paul Scherrer Institute (PSI), aims at a holistic use of (wet) biomass and organic waste streams.[1] The organic (hence, carbon-containing) parts are decomposed under hydrothermal conditions and converted into synthetic natural gas (SNG) which can be fed into the existing natural gas grid and used for heating or power generation. The inorganic moieties in the biomass (e.g. N, P, K, Mg, Ca) can potentially be separated and concentrated in a salt brine that can be recycled and used as fertilizer. Lastly, toxic substances – both chemicals like dioxins and biological hazards such as bacteria and germs – are likely to be destroyed in the process, similar to what has been observed for supercritical water oxidation (SCWO).[21,22]

Figure 1.1 displays a sketch of the demonstration unit that has been built at PSI. Biomass slurries or liquid feeds are fed into the plant at a pressure of 30 MPa. The feed is pre-heated to about 350°C, initiating the hydrolysis and liquefaction of biomass in the hot, compressed water. In the next step, the feed is further heated to about 450°C and thus reaches the supercritical state. Here, a brine containing salts and residual solids can be separated. After this step, the purified stream contains mostly water and small organic molecules (e.g. sugars, aromatics, acids and alcohols) and enters the catalytic reactor which operates at around 400°C. The reactor contains a carbon-supported Ru catalyst (Ru/C) which converts the organics to methane, carbon dioxide, hydrogen and trace amounts of carbon monoxide. After cooling down and expansion to ambient pressure, the reactor effluent then enters a phase separator where the liquid water phase is separated from the product gases. A fraction of the product gas can be burnt to supply the necessary process heat. Through heat recovery from the hot reactor effluent, the overall process can reach a net thermal efficiency of 60-70%, mainly depending on the composition of the biomass (e.g. a higher oxygen

content in the biomass leads to a lower heating value and therefore to lower thermal efficiency).[1]

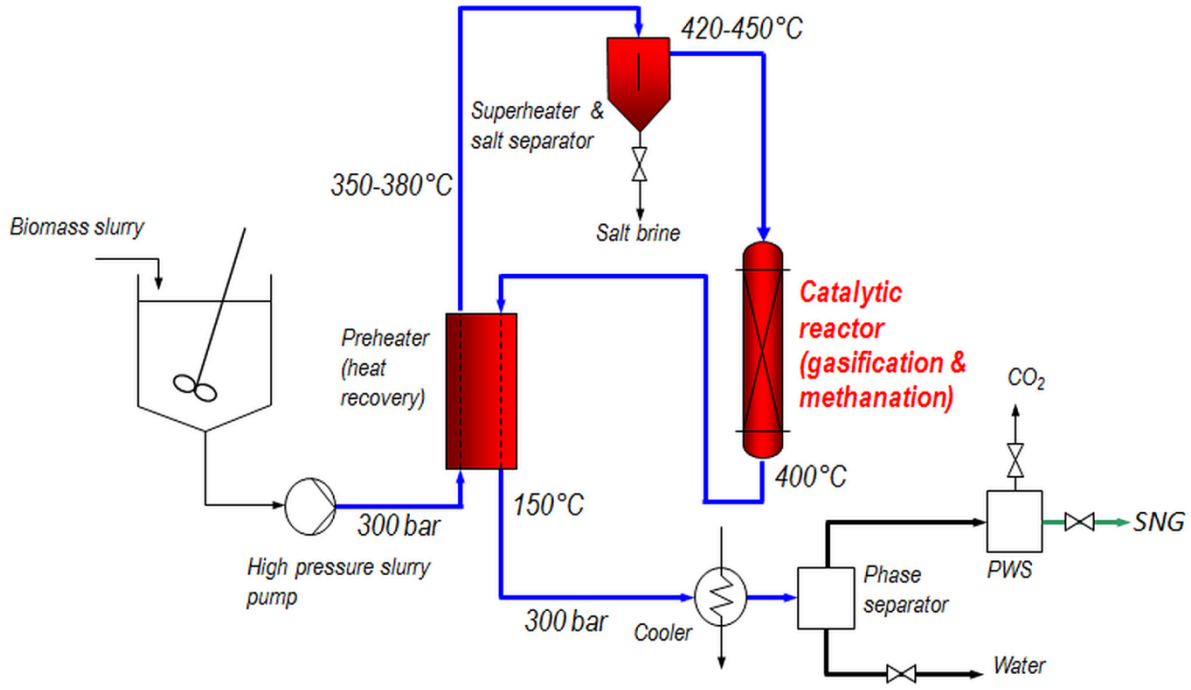

***Figure 1.1**: Sketch of the lab-scale demonstration unit for supercritical water gasification (SCWG) at the Paul Scherrer Institute. Adapted from Vogel.*[1,19,23]

1.2 Properties of water at elevated temperatures and pressures

Throughout this thesis, water at high pressure and high temperature has been used as a reaction medium for the conversion of organic compounds to methane. Under these conditions, water changes its typical, liquid-state properties and presents itself as a highly potent reactant and solvent. This change in properties is the key to hydrothermal processing of organic feedstocks, as outlined in the following paragraphs.

A simplified phase diagram for pure water is depicted in Figure 1.2 for temperatures above 20 °C.[24] The solid line (saturation line) represents the vapor pressure of pure water. At each temperature and pressure pair along this line, two phases exist: liquid water in equilibrium with water vapor. The saturation line results from heating water in a closed system. With increasing temperature, increasing amounts of water evaporate, filling the volume above the liquid phase with vapor which then results in an increase in pressure.[1]

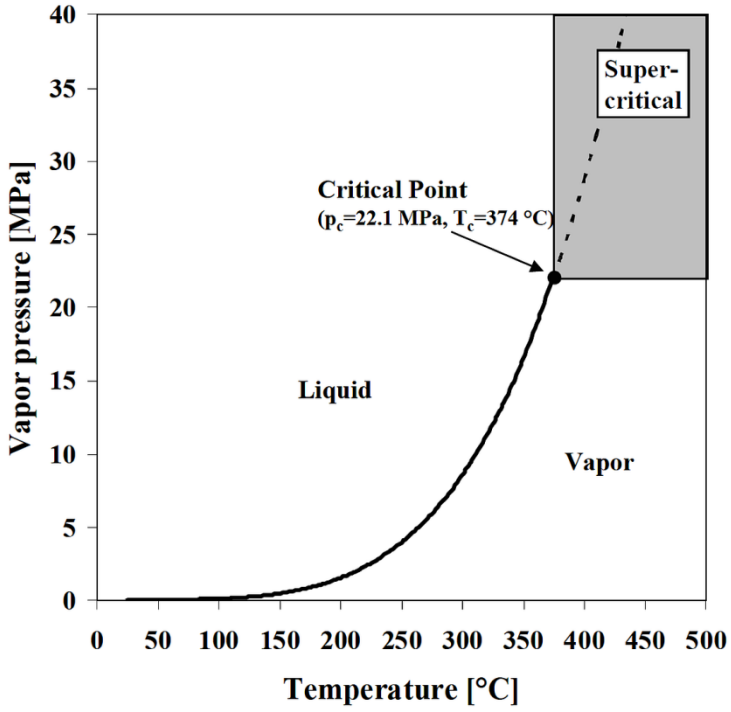

***Figure 1.2**: Simplified phase diagram for pure water at temperatures above 20 °C. Adapted from Schubert.*[23,24]

Thus, both temperature and pressure increase along the saturation line. Due to the increasing temperature during heat-up, the density of the liquid phase will decrease while the density of the vapor phase will increase due to the increasing pressure. At a temperature of T_c = 374 °C and a pressure of p_c = 22.1 MPa, the vapor and the liquid phase will reach the same density (ρ_c = 322 kg/m^3) and thus become a single fluid phase. This point is called the critical point, with its critical temperature T_c and critical pressure p_c. Water at conditions close to but below the critical point is usually referred to as subcritical or near critical water (NCW). Water at temperatures of $T > T_c$ and pressures of $p > p_c$ is called supercritical water (SCW). In this temperature and pressure regime water exists only as a single homogeneous phase. When pressurized water (with $p > p_c$) is heated from ambient to supercritical temperatures, the supercritical state is reached directly from the liquid state. Hence, no energy is lost due to evaporation of water.

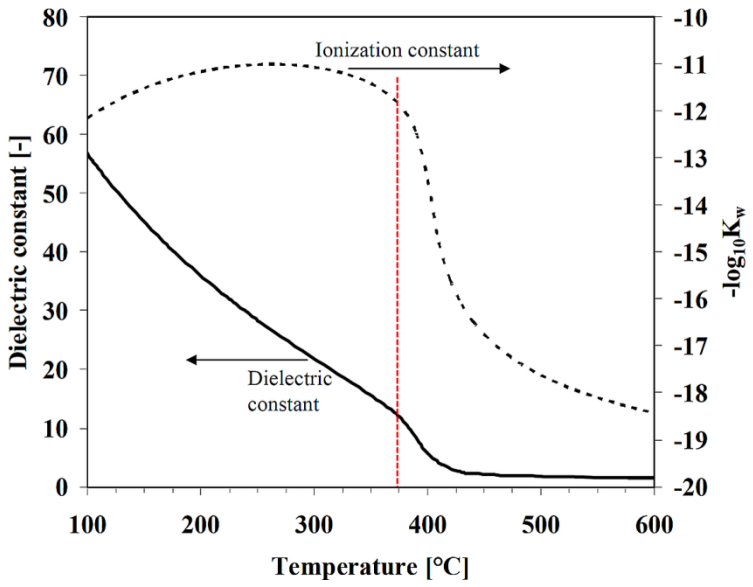

***Figure 1.3**: Dielectric constant and ion product of water as a function of the temperature at 30 MPa. The red, dashed line indicates the critical temperature T_c = 374°C. Adapted from Schubert.*[23,25,26]

Water exhibits unique properties in its supercritical state, which are of importance for hydrothermal biomass conversion. The following two features of supercritical water are most important:[1]

- *Water as a solvent*
  - *for weakly polar and non-polar organic compounds*
  - *for gases*
  - *for inorganic materials such as salts and metal oxides*

- *Water as a reactant*
  - *hydrolyzing agent*
  - *gasifying agent*
  - *oxidant*

By adjusting T and p beyond the critical point, the fluid and solvent properties of water can be tuned.[6] The dielectric constant determines the solvent properties of water and the ion dissociation of salts.[27] In near- and supercritical water the dielectric constant exhibits values of typical organic solvents such as acetone (ε = 20.9), pyridine (ε = 12.8), diethyl ether (ε = 3.9) or n-hexan (ε = 1.6), which is illustrated in Figure 1.3.[25] Due to the decreasing dielectric constant, near-and supercritical water is able to dissolve non-polar organic molecules, such as benzene (Figure 1.4).[1,6,27,28] Due to the high reactivity of NCW/SCW, large organic structures (such as lignin in woody biomass) are broken down to smaller molecules which then dissolve to form a homogenous phase (Figure 1.4). The dissolution of organic coke precursors is a very important feature, preventing their deposition on catalysts and reactor walls.[1]

Furthermore, the solubility of gases such as CO, CO_2, H_2 and CH_4 increases steadily towards the critical point of water. Supercritical water becomes completely miscible with these gases and forms a single-phase fluid. Due to its relatively high density and low viscosity, SCW exhibits better heat transfer rates than gases and higher diffusivities than liquids.[1]

On the other hand, the ability of water to dissolve highly polar or ionic inorganic compounds, e.g. salts, decreases with decreasing dielectric constant.[27] Therefore, these materials can be separated from the supercritical medium in the form of concentrated salt solutions.[23] For example, dilute solutions of so-called type 1 salts, such as K_3PO_4 or KNO_3, form a liquid and a vapor phase, each saturated with salt, under supercritical conditions whereas dilute solutions of type 2 salts, such as Na_2SO_4, form a supercritical fluid phase and a solid salt phase.[29]

According to reaction (1.1), the ion product of water is defined as (1.2):

$$H_2O \leftrightarrow H^+ + OH^- \tag{1.1}$$

$$K_w \equiv [H^+] \cdot [OH^-] \tag{1.2}$$

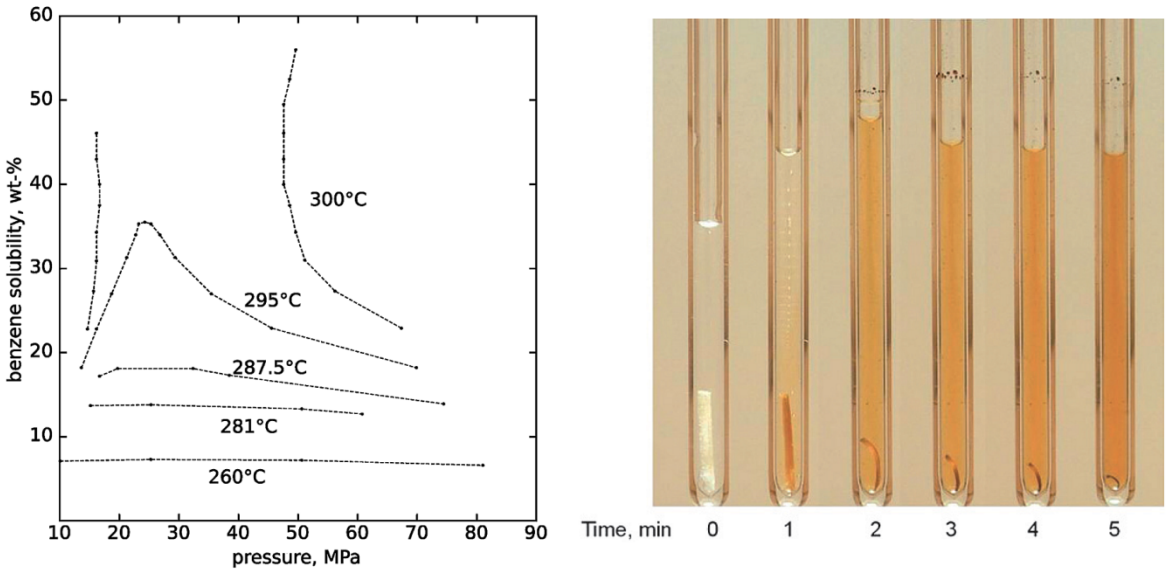

***Figure 1.4**: Pressure and temperature dependence of benzene solubility in water (left) and dissolution of wood in water at 340°C (right). Adapted from Peterson et al.*[3]

The ionization constant of liquid water increases by roughly three orders of magnitude from about 10^{-14} mol^2/kg^2 at 25 °C to about 10^{-11} mol^2/kg^2 in the range of 250- 350 °C and drops rapidly in the vicinity of the critical point to values far below the value at ambient conditions. As an example, the ion product is depicted in Figure 1.3 as a function of temperature at a pressure of 30 MPa.[26] Due to the enhanced self-dissociation, sub-critical water is able to catalyze acid-base catalyzed reactions such as hydrolysis or condensation reactions.[1,8,13,30]

Ionic reaction pathways are favored in sub-critical or supercritical water at high densities, whereas free radical reactions are favored in high temperature supercritical water at low densities.[11,31,32] Thus, the reaction pathways may be controlled by adjusting the density of the reaction environment.

1.3 Catalytic supercritical water gasification (SCWG)

Heterogeneous catalysts for the production of CH_4 serve primarily to increase the rates of the methanation reactions (1.4) and (1.5) and of the water gas shift (WGS) reaction (1.6) which provides the hydrogen required for methanation. By catalyzing the preceding steps of hydrolysis and steam reforming of organic molecules (1.3), the rate of the total conversion to methane is also accelerated. As the hydrolysis of biomass is a reaction between a solid and liquid water, homogeneous catalysis (where reactants and the catalyst are present in the same phase; e.g. dissolved molecular or ionic catalysts) is more effective than heterogeneous catalysis (e.g. metal nanoparticles on a solid support). Heterogeneous catalysts then become effective when small organic moieties (lower molecular weight compounds) have been formed that can dissolve in the reaction medium and thusly access the catalytic sites. Steam reforming of these compounds then becomes the main reaction over heterogeneous catalysts.[1]

$$CH_xO_y + (1-y)H_2O \longrightarrow CO + (x/2 - y + 1)H_2 \quad (1.3)$$

$$CO + 3H_2 \leftrightarrow CH_4 + H_2O \quad (1.4)$$

$$CO_2 + 4H_2 \leftrightarrow CH_4 + 2H_2O \quad (1.5)$$

$$CO + H_2O \leftrightarrow CO_2 + H_2 \quad (1.6)$$

The three main reactions in pressurized water in the presence of a catalyst are WGS (1.6), methanation (1.4 and 1.5) and steam reforming (1.3), with their relative rates being WGS >> methanation > steam reforming. In absence of a catalyst, chemical equilibrium is typically not reached even at 600°C.[1]

The steam reforming reaction is generally endothermic. The WGS is slightly exothermic, as are both methanation reactions. If hydrogen is the desired product, the reactions (1.4) and (1.5), leading to the formation of methane, must be suppressed. Due to the exothermicity of the methanation reactions, hydrogen production is favored at higher temperatures.[4,33,34] Although the pressure dependence is far less pronounced, hydrogen yields will slightly decrease and methane yields slightly increase at higher pressures.[4,33] High methane yields are favored at lower temperatures and high feed concentrations.[4,19,33]

Steam reforming in supercritical water over metals whose predominant phase is an oxide or hydroxide under hydrothermal conditions, e.g. nickel, might proceed according to a Mars-van Krevelen redox mechanism (a redox-cycle between metal and metal oxide).[1] Based on ex-situ X-ray diffraction (XRD) results that showed both metallic Ni and NiO on a spent Ni catalyst after hydrothermal gasification of wastewater, Sharma et al. proposed a mechanism where Ni is partially oxidized to NiO by water.[35] The NiO oxidizes adsorbed organic species to CO and H_2 and is in turn reduced to metallic nickel. The CO and H_2 then react further to form methane, according to the reactions (1.4) and (1.5). However, despite being a highly active and inexpensive methanation catalyst, nickel catalysts are of limited use for hydrothermal gasification since they suffer from leaching and sintering under these conditions.[36]

Ruthenium has seen increasing use as a catalyst for hydrothermal biomass reforming due to its high activity for the steam reforming, water gas shift and methanation reactions which are the key steps for efficient biomass conversion.[1] In terms of possible supports for such a Ru catalyst, carbon was found to be a stable catalyst support under hydrothermal reaction conditions with excellent long term stability.[37] Supports made of porous carbon (e.g. activated carbon) show good structural and chemical stability even under supercritical water conditions[36] and allow for the immobilization of highly dispersed Ru particles on their surface.[38] Highly active carbon supported Ru catalysts (Ru/C) are also commercially available; e. g. the Ru/C catalyst that was used throughout this thesis was obtained from BASF, Germany.

However, carbon supports are unstable in oxidative media at high temperatures which can pose a problem during potential catalyst regeneration procedures that oxidize the catalyst to remove coke deposits or catalyst poisons such as sulfur.[39] Mild conditions must be applied here to protect the catalyst support. Oxidic catalyst supports are generally preferrable under oxidative conditions but have to be structurally stable and chemically inert in supercritical water.

Composition of Samples 1−11,[a] Diameter of Pellets, Physical Stability,[b] and Crystallographic Stability[c]

sample no.	manufacturer's product designation (Norpro Saint Gobain)	composition (given by manufacturer)	diameter of pellets [mm]	physical stability	crystallographic stability
1	SZ 61152	t-ZrO_2 94%, HfO_2 2.4%, SiO_2 3%	1.5	yes	no
2	SZ 61156	t-ZrO_2 88.2%, HfO_2 1.77%, La_2O_3 9.7%	3	(yes)	(yes)
3	SZ 61157	t-ZrO_2 90.44%, HfO_2 1.85%, SiO_2 0.11, Y_2O_3 7.34%, Al_2O_3 0.17%	3	no	no
4	SZ 61191	t-ZrO_2 78.75%, HfO_2 1.56%, SiO_2 0.6, CeO_2 18.83%, Al_2O_3 0.72%	3	(yes)	no
5	SZ 31140	ZrO_2 56.7%, TiO_2 41.3%, $HfO_2$1.1%, SiO_2 0.4%	3	(yes)	(yes)
6	ST 61120	TiO_2 anatase	3	no	(yes)*
7	SZ 31163	ZrO_2 monoclinic	3	(yes)	yes
8	ST 51122	TiO_2 rutile	3	yes	yes
9	SZ 61143	t-ZrO_2 82.4%, HfO_2 1.49%, Al_2O_3 0.17%, WO_3 15.94%	3	(yes)	no
10	SZ 31107	ZrO_2 monoclinic	3	(yes)	yes
11	SZ 31262	ZrO_2 monoclinic	1.5	yes	yes

[a]t: tetragonal. [b](yes) = stable but traces of attrition. [c](yes) = minuscule changes. * = crystal particle growth but no phase change.

***Table 1.2**: Stability of metal oxide supports in supercritical water. Adapted from Zöhrer et al.*[40]

The work of Zöhrer et al. gives a good overview over the performance of several oxidic catalyst supports during supercritical water gasification of glycerol.[40] Based on what is known from literature, they selected zirconia and titania as the most promising materials and studied the stability of different morphologies of these catalyst supports under

hydrothermal conditions (Table 1.2). The majority of the tested catalyst supports was not stable in supercritical water, showing strong attrition and/or changes in the crystal structure. With the exception of rutile TiO_2 and monoclinic ZrO_2 (sample 11), all of the supports showed a significant loss of surface area after 20 hours of treatment in SCW. After this initial decrease in surface area, most materials remained stable during another 20 hours in SCW. Based on the stability tests, several zirconia supports (samples 2, 5, 7 and 11) and rutile TiO_2 (sample 8) were chosen for catalyst preparation via impregnation with ruthenium nitrosylnitrate. The performance of the obtained Ru catalysts was studied during the SCWG of glycerol over a time span of 24 hours. With the exception of the mixed ZrO_2/TiO_2 support (sample 5), the catalysts showed high selectivities for methane production, with gas compositions close to the thermodynamic equilibrium. Extended tests showed that the Ru catalysts supported on rutile TiO_2 and hafnium/lanthanum doped zirconia (sample 2) gave the best overall performance with excellent structural stability and stable glycerol gasification (in terms of carbon selectivities and gasification efficiency) over the duration of the experiments. Since titania is a readily available and relatively inexpensive material, it is an attractive alternative to carbon supports in the preparation of Ru catalyst for use in hydrothermal conditions. The potential of Ru/TiO_2 has also been shown for the gasification of phenol in long term experiments (up to 14 weeks on stream)[37], for continuous ethanol gasification over 70 hours[19] and for the gasification of lignin in a series of batch experiments.[41,42] In all of these studies a good stability of the titania support and high methane yields were observed.

Whereas most studies found in literature concentrate on the conversion of different biomass-based materials over Ru catalysts and the composition of obtained reaction products, there have been only few attempts to study these catalytic systems from a mechanistic point of view.

A mechanism, similar to the one outlined above in the case of nickel, was proposed by Park and Tomiyasu for the hydrothermal gasification over Ru catalysts.[43] In batch experiments, they gasified naphthalene in supercritical, deuterated water (D_2O), using unsupported RuO_2 as a catalyst. From the distribution of deuterium in the produced methane, they concluded that the gasification reaction proceeds primarily through a partial oxidation of organic compounds by RuO_2 to produce CO and H_2O, whereas RuO_2 would be reduced to a lower

oxidation state in the process. The reduced Ru species are then re-oxidized by reducing water to form hydrogen (Figure 1.5). Finally, the produced CO and H_2 form methane via the methanation reaction (1.4). In their proposed mechanism, the redox couple is Ru^{IV} / Ru^{II}:

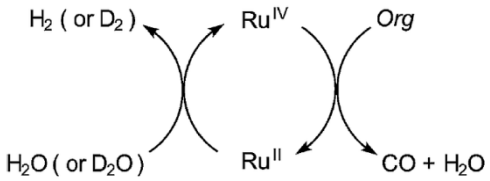

***Figure 1.5**: SCW-induced redox cycle between Ru^{IV} and Ru^{II}, catalyzing the gasification of organic compounds, as proposed by Park and Tomiyasu.*[43]

However, this mechanism for the gasification over ruthenium catalysts contradicts more recent findings of Ketchie et al.,[44] Yamaguchi et al.[42,45] and Rabe et al.[46] that suggest the presence of metallic ruthenium under SCW conditions.

Yamaguchi et al. gasified lignin over unsupported ruthenium salts ($RuCl_3$ and $RuNO(NO_3)_3$) and Ru salts supported on carbon or titania.[42,45] For each catalytic system, they found metallic ruthenium particles after the catalytic gasification of lignin at 400°C and 37.2 MPa in batch reactors. The characterization of the catalyst samples was performed with X-ray diffraction (XRD) before and after gasification. Furthermore, ex-situ EXAFS (extended X-ray absorption fine structure) measurements of the spent catalyst samples were carried out at room temperature after the gasification experiments. The catalyst samples were recovered from the reactor as a water suspension and quickly filled into an EXAFS cell. The EXAFS measurements were performed under air-exposed conditions. However, the authors did not observe signals indicating oxidized ruthenium on the catalyst samples. The formation of metallic ruthenium was also observed when the carbon supported ruthenium catalyst had been treated in supercritical water in absence of organics.[45] This suggests that oxidized ruthenium species might be able to auto-reduce by oxidizing their carbon support under hydrothermal conditions.

Rabe et al. performed the first in-situ X-ray absorption (XAS) study of the continuous hydrothermal gasification of ethanol at 25 MPa and at temperatures up to 390°C.[46] They used a commercially available, carbon supported Ru catalyst with a Ru loading of 2 wt%. The ruthenium on the as received catalyst was present in the form of RuO_2, but was quickly reduced to metallic ruthenium at temperatures around 150°C upon exposure to an aqueous 5 wt% ethanol solution. Once reduced, the ruthenium remained in the metallic state over the entire temperature range of the experiment (up to 390 °C).

These findings indicate that the active phase of the catalyst under SCW conditions is metallic ruthenium rather than oxidized ruthenium. However, it is not clear yet whether the methane formation takes place via the hydrogenation of CO, the hydrogenation of CO_2 or through a different pathway. It is assumed that the methanation proceeds via the hydrogenation of CO_2, since the WGS is fast in the hydrothermal environment due to a strong adsorption of CO on transition and noble metal catalysts, leading to a high surface coverage of CO and H_2O (due to the high partial pressure of water) and therefore to a fast WGS.[1] Additionally, Kudo and Komatsu reported the formation of methane from CO_2 (or alkali carbonates) and water in the presence of a Raney nickel alloy and a Ru/C catalyst at 380°C and 22 MPa.[47,48]

In their study on ethanol gasification over carbon supported Ru, Rabe and coworkers suggested a catalytic mechanism for the formation of methane which is similar to the steam reforming of ethanol.[46] They suggested that ethanol is adsorbed on the catalyst and dehydrogenated to acetaldehyde, followed by C-C bond rupture and subsequent formation of CH_4 and CO. CO then remains strongly adsorbed on the catalyst and is converted to CO_2 via the WGS, thus generating H_2 (which then can hydrogenate CO_2 to form methane).

On the other hand, the results of Park and Tomiyasu suggest a pathway via methanation of CO.[43] In their experiments, the gasification of naphthalene in deuterated water over RuO_2 as catalyst led to the almost exclusive formation of fully deuterated CD_4. Based on these results they concluded that methane is formed by direct methanation of CO (from the steam reforming of naphthalene) with D_2 (from water splitting on the Ru catalyst). However, the Ru redox cycle underlying their proposed mechanism has already been disproven, as mentioned above.

In conclusion, the current state of research identified metallic Ru as the active catalyst phase during supercritical water gasification. However, the pathway of the methanation reaction and the nature of surface reactions on the catalyst under these conditions remain unclear.

1.4 Catalyst deactivation due to sulfur poisoning

The high sensitivity of many metal catalysts towards contaminants which are present in real feedstocks, sulfur in particular, is a great challenge for the development of biomass conversion processes. Deactivation of nickel catalysts due to sulfur poisoning has been the subject of many studies.[49] For most metals that are used as catalysts, sulfur shows a poisoning effect. In steam reforming, the actual poisoning sulfur species is H_2S which is a decomposition product of organic sulfur compounds such as thiophene. In a hydrothermal environment, however, a more complex sulfur speciation due to the aqueous chemistry of the sulfur compounds must be considered:[1]

$$SO_4^{2-} + 4H_2 \longrightarrow S^{2-} + 4H_2O \quad (1.7)$$

$$SO_4^{2-} + H_2 \longrightarrow SO_3^{2-} + H_2O \quad (1.8)$$

$$SO_3^{2-} + 3H_2 \longrightarrow S^{2-} + 3H_2O \quad (1.9)$$

$$2SO_3^{2-} + 2H_2 + 2H^+ \longrightarrow {S_2O_3}^{2-} + 3H_2O \quad (1.10)$$

$${S_2O_3}^{2-} \longrightarrow 1/8\, S_8 + SO_3^{2-} \quad (1.11)$$

In addition to sulfide, as in H_2S, elemental sulfur and oxidized, ionic sulfur species such as sulfate, sulfite and thiosulfate might be present under hydrothermal conditions. Additionally, their partially or fully protonated species will coexist, depending on the solvent properties and dissociation of water (hence, depending on temperature). In the presence of

organic compounds, oxidized sulfur species such as sulfate and sulfite can be reduced by hydrogen or the organic compounds directly.

Ruthenium catalysts were found to be quickly poisoned by sulfur compounds under hydrothermal conditions, leading to an irreversible loss of the catalytic activity.[19,23,50] Catalyst poisoning experiments were carried out both in continuous mode with sodium sulfate during the gasification of synthetic liquefied wood over Ru/C,[19,50] and in batch mode with elemental sulfur, thiophene, 2-methyl-1-propanethiol and sulfuric acid during gasification of lignin.[51,52] From these batch experiments, Osada and coworkers concluded that any sulfur species (elemental, reduced or oxidized forms) will poison the Ru catalyst and that sulfur poisoning inhibits the C-C bond scission and the methanation reaction,[52] but not the water gas shift.[51] In contrast, Waldner conducted experiments in a continuous mode reactor and found that also the WGS was hindered after a Ru/C catalyst had been completely deactivated by sulfur.[19,50] The difference here might lie in the mode of experimentation, since it is known that the steel walls of batch reactors can catalyze the WGS reaction (the effect being less pronounced during continuous experiments due to shorter residence times in the reactor).[1]

The studies of Osada show that their Ru/C and Ru/TiO_2 catalysts were covered with sulfur in various oxidation states (S^{II-}, S^{IV} and S^{VI}) after batch gasification of lignin in presence of elemental sulfur, sulfuric acid and various organic sulfur compounds.[52] Since the analysis of the spent catalyst samples was performed via ex situ X-ray photoelectron spectroscopy (XPS), it remained unclear which sulfur species is the actual poisoning agent under hydrothermal reaction conditions. Sulfur species adsorbed on the catalyst may have been oxidized when the samples were exposed to air prior to characterization, thus obscuring the results.

Elliott and coworkers investigated the effect of several trace contaminants on the hydrogenation of sugars over a Ru/TiO_2 catalyst.[53] Although this reaction was carried out in water at 100°C and with H_2 pressures of 8.3 MPa, hence under conditions which are quite different from the conditions of the catalytic hydrothermal gasification, valuable information about the effects of trace contaminants on the catalytic activity can be extracted from their work. Interestingly, sulfate ions showed no inhibiting effect on catalytic activity under these conditions, suggesting that higher temperatures might be necessary to turn sulfate into a

catalyst poison. Similar results were obtained by Waldner et al. who did not observe catalyst deactivation after continuously feeding a sodium sulfate solution through a Ru/C catalyst bed at 200°C with a $S_{fed}/Ru_{catalyst}$ ratio of 2.71.[19,50]

To study the structure of (poisoned) catalysts and to clarify which species are the actual poisoning agents, it will be necessary to perform in situ analyses under realistic reaction conditions. At the same time, adsorbed species on the catalyst surface can be probed via isotope labeling to gain information on surface reaction mechanisms. This ensures that the catalyst is probed in its actual working state and that the sample quality is not compromised.

1.5 Regeneration of sulfur poisoned Ru catalysts under hydrothermal conditions

Two options for obtaining useful catalyst lifetimes are the development of sulfur resistant catalyst formulations or of regeneration protocols to remove sulfur from poisoned ruthenium catalysts.

Osada et al. proposed a sub-critical water regeneration method.[54] They reported that the regeneration was most effective at water densities of 750-830 kg/m^3 (corresponding to 250-300 °C at 30 MPa). After their regeneration procedure, carbon gasification efficiencies of 50 % were achieved whereas a fresh catalyst sample gave 97 %, a sulfur poisoned catalyst gave 20 % and a catalyst-free experiment gave 8 % gasification efficiency, respectively. However, the relevance of the used method for sulfur poisoning remains questionable. Osada and coworkers impregnated Ru/TiO_2 with sulfuric acid at room temperature and dried the catalyst samples by evaporation. They referred to the obtained catalyst samples as S-Ru/TiO_2. The subcritical water regeneration procedure, however, was applied before these S-Ru/TiO_2 samples were exposed to SCWG conditions. As mentioned in the previous section, Elliott and coworkers did not observe a poisoning effect of sulfate ions at low temperatures.[53] Thus, it is questionable whether the S-Ru/TiO_2 samples of Osada et al. were really poisoned by sulfur. The amount of deposited sulfate ions would simply be decreased by the subcritical water treatment before performing actual SCWG experiments. The

influence of water density on the “regeneration efficiency” is then not surprising, given the temperature dependence of the polarity and ion product of water, as explained in section 1.2.

A more realistic experiment was performed by Waldner.[19] A Ru/C catalyst that was poisoned by sulfur (in the form of sulfate) under SCWG conditions was treated with a 1 wt% H_2O_2 solution at mild conditions (50°C and 90°C at 30 MPa) for a total of 6.3 hours. This oxidative treatment led to a recovery of catalytic activity and a product gas that attained the chemical equilibrium for the gasification of ethanol at 30 MPa and 400°C. However, the catalyst’s activity decreased again within 24 hours on stream. It was concluded that the treatment time with the peroxide might have been too short for a complete regeneration. Since the experiment was run at full carbon to gas conversion, it was not possible to determine how much of the original catalytic activity could be regained by the peroxide treatment. The effect of hydrogen peroxide on the sulfur poisoned Ru/C catalyst remained unclear, as this requires in situ spectroscopic methods.

1.5.1 Comparison with gas phase methanation: on-stream regeneration of S-Ru/Al_2O_3

Whereas only little information can be found on the regeneration of metal catalysts under hydrothermal conditions, it is worthwhile to look into gas phase regeneration procedures where a plethora of studies is available.[55–57] An interesting concept was published by König et al. who suggested an integrated process where a methanation catalyst (Ru/Al_2O_3) is poisoned over time by sulfur and subsequently regenerated in an oxygen-containing gas stream.[58] This is of particular interest for methane production from the producer gas of dry biomass gasification which can contain large amounts of sulfur.[59–63] Since Ru does not form a stable sulfate phase – in contrast to Ni catalysts – oxygen at high temperatures can be used to remove adsorbed sulfur and thus regenerate the catalyst.

In their study, König et al. used a model feed gas, containing H_2, CO and several sulfur species (H_2S, thiophene and carbonyl sulfide), and modulated the feed composition to simulate the exposure of the Ru/Al_2O_3 catalyst to different environments (sulfur-containing producer gas and dilute oxygen, respectively). Methanation in CO/H_2 and sulfur poisoning

took place at 300°C whereas catalyst regeneration with dilute oxygen was performed at 550°C (Figure 1.6).

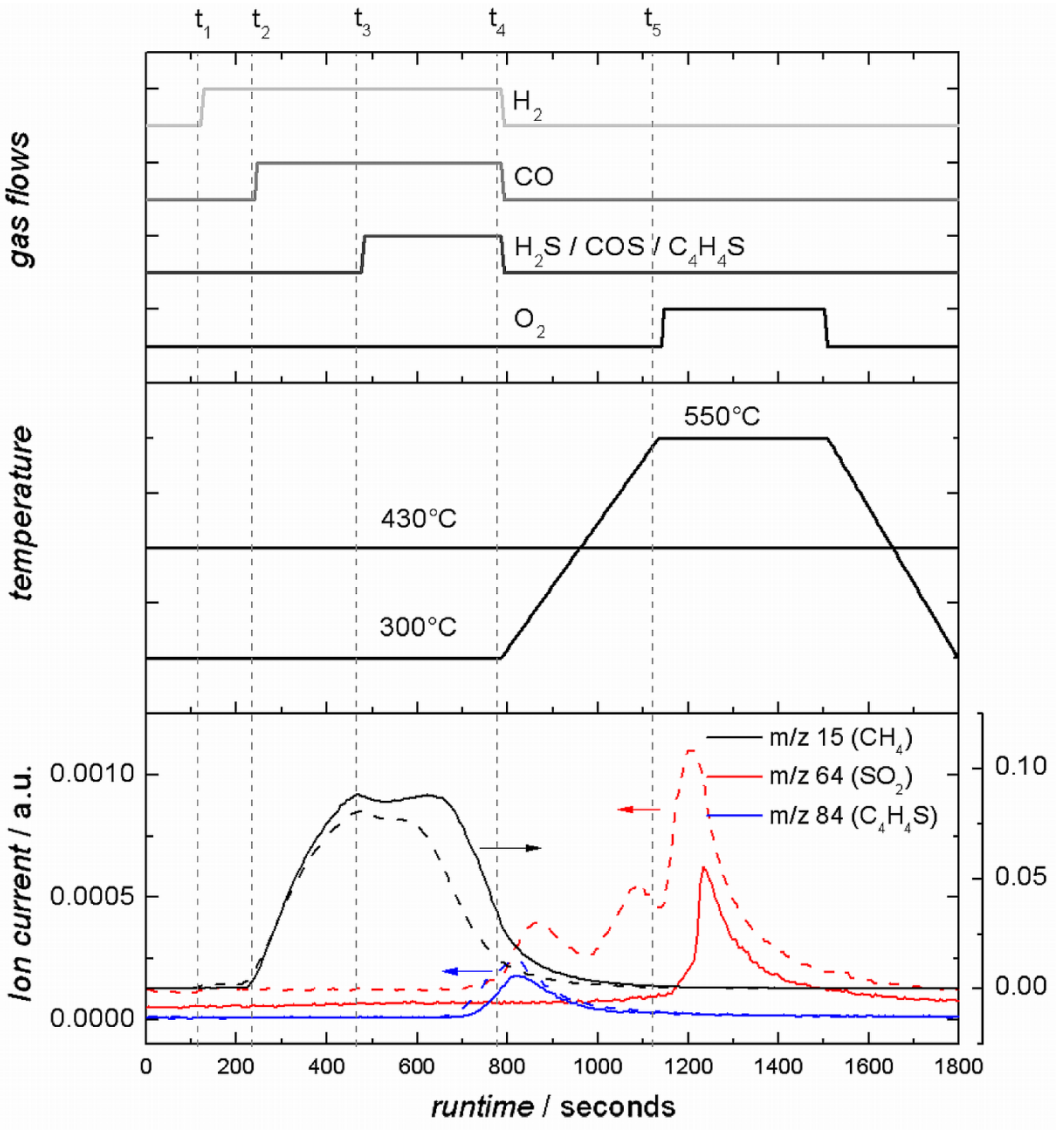

***Figure 1.6**: Schematic of gas flows (top) and temperature profiles (center) during one cycle of methanation and poisoning. The points in time where gas flows were changed are indicated by dashed vertical lines. Mass spectrometer traces (bottom) for the reactor outlet of the nonisothermal experiment where methanation was performed at 300°C and oxidative regeneration was performed at 550 °C. Shown are CH_4 (m/z 15, black), C_4H_4S (m/z 84, blue), and SO_2 (m/z 64, red). The solid lines show the first cycle, the dashed lines the 20th cycle. Adapted from König et al.*[58]

The catalyst was exposed to a series of methanation-poisoning-regeneration cycles while its activity was monitored by MS analysis of the product gas. At time t_1 (see Figure 1.6), the catalyst was reduced in H_2, followed by the addition of CO (t_2), at which point methanation set in. After the addition of sulfur to the gas feed (t_3), the methane production started to decrease and sulfur was detected at the reactor outlet. After flushing with helium (t_4) and heating up to 550°C, the deactivated catalyst was exposed to oxygen (t_5) and SO_2 was released.

At the beginning of the next cycle, the methanation activity was recovered and the sequence repeated. Over the course of 20 cycles, a 50% decrease in methanation activity and an increase in released SO_2 was observed. König at al. attributed that to an accumulation of sulfur on the alumina support via formation of $Al_2(SO_4)_3$. A similar result was obtained for cycles where both methanation and regeneration took place at the constant temperature of 430°C which is advantageous from a process engineering point of view. In this case, the methanation activity dropped down to about 20% of the original value where it seemed to stabilize. Under sulfur-free conditions, the activity recovered back to about 65% of the initial value over several regeneration cycles.

A time resolved structural analysis of the Ru catalyst via in situ EXAFS revealed that surface adsorption of sulfur was responsible for decrease of catalytic activity (Figure 1.7). Bulk sulfidation was not observed under the chosen reaction conditions. Upon catalyst regeneration in dilute oxygen, the Ru particles were partially oxidized to RuO_2. Adsorbed sulfur was oxidized to SO_2 and removed from the Ru surface. However, a layer of $Al_2(SO_4)_3$ on the surface of the catalyst support was formed which acted as a sulfur storage system, releasing sulfur during the reactivation of the catalyst in H_2. The released sulfur can then act as a catalyst poison again.

In summary, the results show that a steady state of methane production in the presence of sulfur can be attained through periodic catalyst regeneration, albeit at a 50% to 80% lower rate as under sulfur free conditions. These findings are encouraging with regards to the development of similar, periodic regeneration methods that involve an oxidative treatment of Ru catalysts under hydrothermal reaction conditions. Whereas the harsh conditions of gas phase oxidation forbid the use of carbon supported catalysts, the milder reaction conditions

in hydrothermal media allow for Ru/C catalysts on which sulfur storage might be significantly lower than on Al_2O_3.

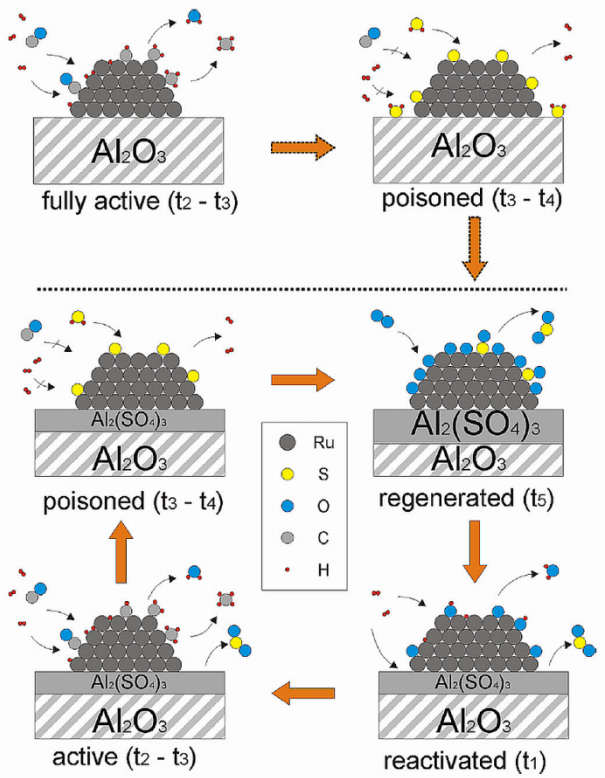

***Figure 1.7**: Schematic representation of the mechanisms during methanation, poisoning, regeneration and reactivation. Adapted from König et al.*[58]

1.6 Methods for probing the structure of solid samples in situ

In the preceding subchapters, it has been mentioned multiple times that in situ investigations are key to properly assess catalyst structure, reaction mechanisms and phenomena like catalyst poisoning under realistic process conditions. There are a number of techniques available to study the structure of solid samples, each with its advantages and limitations. Most of these techniques are based on the interaction of electromagnetic radiation with solid matter.

Infrared (IR) spectroscopy probes vibrations of molecules whose molecular dipole moment changes due to certain molecular vibrations. These molecules include for instance CO, CO_2, H_2O or CH_4. If the molecules are adsorbed on a catalyst surface, the vibrational frequencies change due to the interaction with the surface, and these changes can be detected in the IR spectra. The state of the solid catalyst can be probed by attenuated total reflectance (ATR) IR spectroscopy which is however not compatible with hydrothermal conditions.

X-ray photoelectron spectroscopy (XPS) probes the occupied orbitals of the sample. The X-rays create photoelectrons that are analyzed according to their energies, which are related to the electron's binding energies. Due to the low penetration depth of electrons, XPS is a surface sensitive technique that is usually performed at very low pressures. Recent developments in differential pumping allow in situ XPS experiments, while the absolute gas pressures are still far below those that are accessible with other X-ray based techniques.[64–66]

X-ray diffraction (XRD) determines the structure of crystalline samples, based on Bragg's law, but is not sensitive to amorphous samples. XRD typically probes the bulk of the sample, irrespective of the sample's element. Information on particle size can be derived from the Scherrer formula,[67] given that the particles are large enough (larger than about 2 nm) to be detected by XRD.[68] However, the analysis of supported catalysts can be complicated by overlapping peaks from the catalyst support and the active catalyst phase. Furthermore, the sensitivity of the method is often not high enough to study catalysts with low metal loadings.

X-ray radiation can also be used for spectroscopy, where it probes the elements of choice. In X-ray absorption spectroscopy (XAS), the energy of the X-ray photons is varied around the binding energy of the core electrons of the probed element to measure the sample's

absorption coefficient as a function of energy. In contrast to XRD, XAS does not require crystalline samples, and is not limited by the particle size of the sample. It is also sensitive to catalysts with low metal loadings and very small particles. Since X-ray photons with high energy can penetrate reactor walls, XAS is an excellent tool to study catalysts under reaction conditions even at high pressures and temperatures.

1.7 Aim of the project

The goal of this thesis was to study the structure of Ru catalysts and catalytic reaction mechanisms under realistic reaction conditions during the SCWG of organic model compounds, hence in situ. As outlined above, the in situ approach is imperative in order to guarantee the integrity of the sample, since ex situ analysis is often compromised by sample degradation. This general goal was sub-divided into the following objectives:

- Reviewing experimental results and the deduced reaction mechanism from previous experiments at PSI in the SCWG of organic compounds: Chapter 3

- Designing a high-pressure, bench-top setup to study the gasification of organic key compounds in SCW: Chapter 3

- Developing the experimental infrastructure necessary to perform spectroscopic in situ studies under supercritical water conditions. X-ray spectroscopy was selected as the method of choice since high energy photons are able to penetrate relatively thick reactor walls: Chapter 4

- Establishing direct chemical probes that can be used to study reaction mechanisms on the catalyst's surface in parallel with the spectroscopic in situ studies. Isotope labeling of reactants and products was used in combination with density functional

theory (DFT) calculations to directly probe adsorbed species on the catalyst's surface: Chapter 5

- Studying the structure of a Ru/C catalyst under operando conditions with a focus on the methanation reaction on the active and sulfur poisoned catalyst: Chapter 6

- Developing and optimizing regeneration protocols for Ru catalysts that have been deactivated by sulfur poisoning or coke formation: Chapter 7

- Proposing a reaction mechanism for the gasification of ethanol on Ru: Chapter 8

Each chapter will contain a short introduction to the respective task, including an experimental section, results and discussion and a conclusion.

The results will be summarized in Chapter 9 which also contains recommendations for further research.

Chapter 2

X-ray absorption spectroscopy

X-ray absorption spectroscopy (XAS) has been developed over the last four decades into one of the most widely used and powerful probes of the local atomic structure. The elemental specificity arises from the unique energies of the atoms' core orbitals. XAS provides the local geometric and electronic structure of a particular element and has been widely used to study the structure of materials in the solid and liquid phase. Such studies have been successfully performed under high pressure, at high temperature and in the presence of reactive gases and liquids.[69] Since XAS probes the local structure, it can be applied to structurally disordered and ordered solids and to disperse species such as small metal clusters.[70] The analysis of disordered and nano-sized samples is a major advantage of this spectroscopic technique compared to X-ray diffraction which requires structurally ordered samples of sufficient particle size (typically > 2 nm).[68]

The fundamentals of synchrotron-based X-ray absorption spectroscopy, which is the main spectroscopic technique used in this project, will be explained in this chapter. The underlying physical processes that give rise to an X-ray absorption spectrum and basic data treatment are described in detail.

2.1 Absorption of X-ray radiation in a sample

To determine the X-ray absorption of a sample, the intensity of the X-ray beam is measured in front of and behind the sample. According to the Lambert-Beer law, the transmitted intensity I_t is:[71]

$$I_t = I_0 e^{-\mu \cdot d}$$

with I_0 as the beam intensity in front of the sample, μ as the absorption coefficient (or absorbance) of the sample and d as the thickness of the sample. Resolving the equation for μ then gives the absorption coefficient as a function of sample thickness and the measured intensities:

$$\mu = \frac{1}{d} \ln \left(\frac{I_0}{I_t}\right)$$

This relation is true for homogeneous samples, independent of their aggregate state (gaseous, liquid or solid). Furthermore, the absorbance depends on the photon energy and the atomic weight of the sample, with heavy elements absorbing more X-ray radiation than light elements at the same photon energy. Scanning the photon energy of an X-ray beam, step-like changes in the absorption coefficient are observed at specific photon energies. The position of these so called absorption edges on the energy scale depends on the binding energies of the electrons in the probed atom (Figure 2.1).

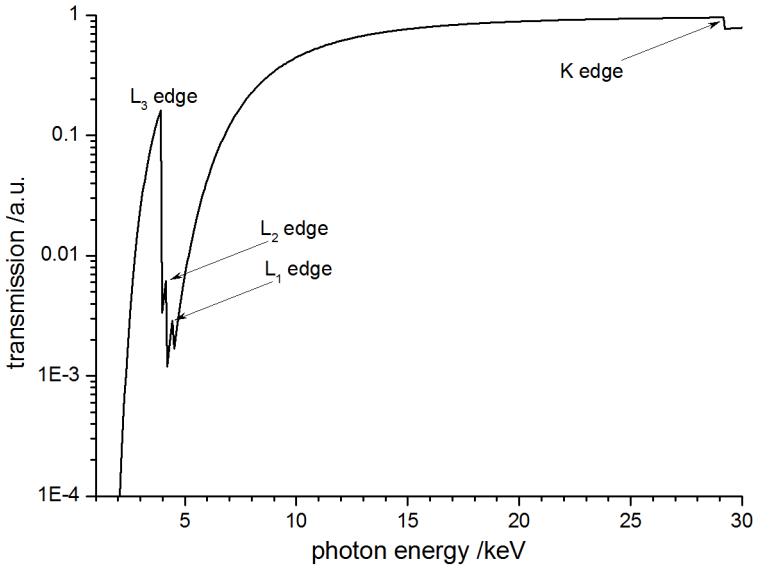

***Figure 2.1**: Calculated transmission spectrum of a 6 µm thick tin foil.[72] At the binding energies of the core electrons, the absorption of X-ray photons gives rise to step-like changes in the spectrum, the absorption edges (shown here for the K and L shells of the tin atom).*

2.2 Physical background of X-ray absorption

When a photon encounters an atom, it can interact with the electrons in the different electron shells of that atom. If the photon energy matches the energy difference between an electron's binding energy and the energy level of an unoccupied state, the photon is absorbed and will excite the electron into an unoccupied orbital. However, if the photon has an energy that exceeds the binding energy of the electron, the electron will be ejected as a photoelectron, with a kinetic energy that equals the difference between its binding energy and the photon energy (Figure 2.2).

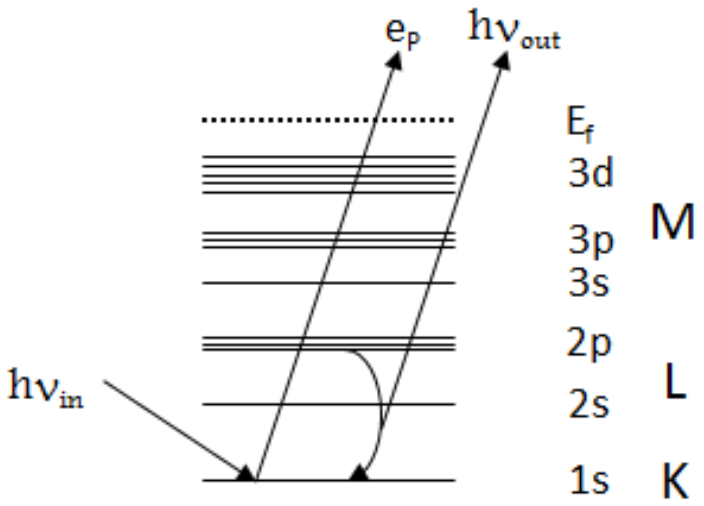

***Figure 2.2**: Schematic energy diagram of K-edge XAS and XES: the incoming photon excites a 1s electron to an energy above the Fermi energy (E_f), creating a photoelectron e_P and a core hole. The core hole is filled, e.g. by a 2p electron, while the energy difference between the 2p and the 1s level is emitted in form of a fluorescent photon.*

The photon energy at which the creation of photoelectrons starts to take place is called the absorption edge and is by definition associated with the energy level of the electron, e.g. K-edge for photon energies matching the binding energy of electrons in the K-shell of a given atom.

Electronic structure of the sample: the near edge structure

Figure 2.3 shows the XAS spectrum of a Ru sample at the Ru K-edge, with the normalized absorption coefficient plotted against photon energy. The absorption coefficient increases at around 22117 eV, which is the binding energy of a 1s electron in a Ru atom. The part of a XAS spectrum in the vicinity of the absorption edge is called the X-ray absorption near-edge structure (XANES). This region of the spectrum contains information on the electronic structure of the absorber atom, such as oxidation state or unoccupied electronic states (hence, unoccupied orbitals). XAS spectra can also show features at energies below the absorption edge, the so called pre-edge features. Those indicate transitions of the excited electron to higher, unoccupied orbitals below the Fermi level. The position of the edge itself is an indication of the electron density around the absorbing atom. The energy required to

eject an electron from an atom typically increases with its oxidation state, resulting in a higher energy of the observed absorption edge.

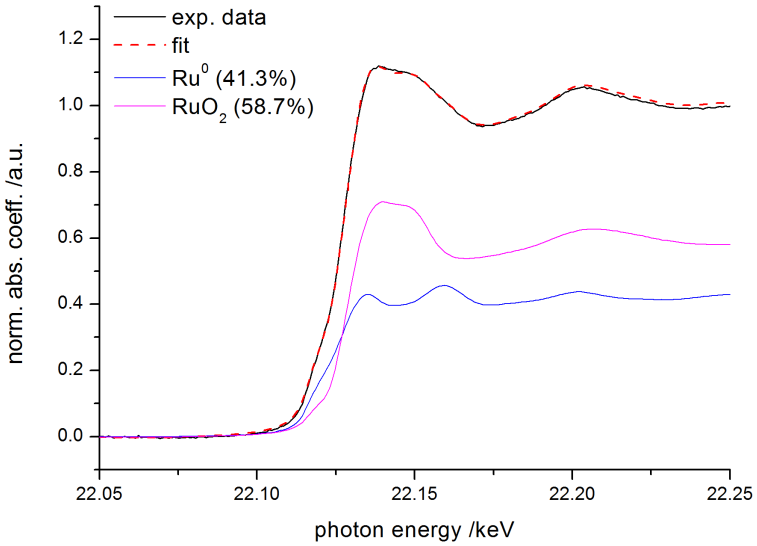

***Figure 2.3**: Ru K-edge XANES spectrum of a sample, with linear combination fit (dashed line) of two references, metallic Ru (blue) and RuO_2 (pink) weighted by their respective fitted fractions.*

A semi-quantitative analysis of the sample's composition can be performed, based on the fitting of a XANES spectrum with a linear combination of spectra of reference compounds. This is depicted in Figure 2.3, where the XAS spectrum of a Ru sample of unknown composition is fitted with two reference spectra, obtained from metallic Ru and RuO_2, respectively. While it was known that the sample contained both metallic and oxidized Ru, their ratio was determined by linear combination fitting (LCF).

A requirement for linear combination fitting is that spectra of relevant reference compounds exist. Moreover, linear combination fitting of a sample with unknown composition requires knowledge about which reference spectra can be used. Statistical methods can be used to fit the data with correct reference spectra. The accuracy of LCF is typically around ± 5 %.[73] Simulated XANES spectra, obtained from ab initio calculations can be used to simulate XANES spectra of pure compounds.[74] From these computational methods, insights into the sample's electronic structure can be gained. Recently, methods for parameterized calculations of XANES spectra were developed.[75,76] These allow for implementation of full

multiple scattering codes and fitting of XANES spectra to extract structural information and do not rely on experimental references.

Geometric structure of the sample: the extended fine structure region

Starting at about 50 to 100 eV above the absorption edge, solid, liquid and gaseous materials can show an oscillatory structure in the XAS spectrum. These oscillations are called the extended X-ray absorption fine structure (EXAFS) region, carrying a wealth of structural information. If the energy of the incoming photon is higher than the binding energy of the core electron, the latter is released from the atom as a photoelectron, having a kinetic energy that equals the difference between the energy of the incoming photon and the binding energy:

$$E_{kin} = E_{photon} - E_{binding}$$

This photoelectron then moves away from the absorber atom, scatters at the neighboring atoms and is eventually scattered back to the absorber. The outgoing and back-scattered electron wave functions interfere with each other, leading to interference patterns that range from destructive interference (hence, zero amplitude) to constructive interference (hence, maximal amplitude; see Figure 2.4). These interference patterns determine the probability of photoelectron creation (hence, they modulate the absorption coefficient) and depend on the kinetic energy of the photoelectron and the distance of the scattering atom to the absorber. As a consequence, the photoelectron probes the local environment around the absorbing atom. From the point of view of the absorbing atom (the atom where the photoelectron is created), the surrounding atoms are divided into scattering shells (see Figure 2.4), according to their distance to the absorber, their atomic weight and the number of atoms of the same element at the same distance (coordination number).

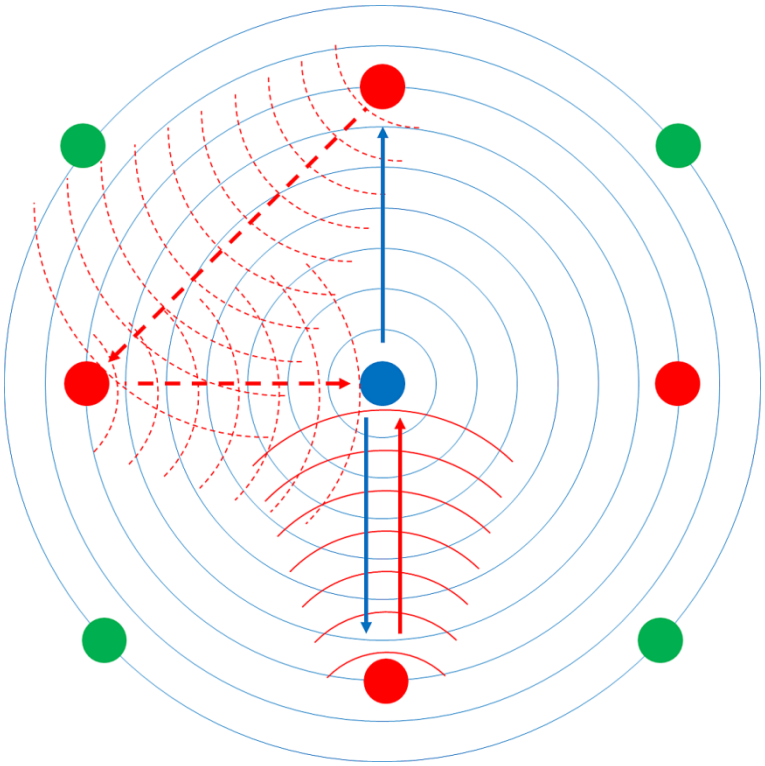

***Figure 2.4**: 2-D sketch of an atomic lattice, with the central absorbing atom (blue), and the two closest scattering shells (red and green). The first and second shells both have a coordination number of 4. The outgoing photoelectron is represented by blue arrows and the blue, centrosymmetric wave. Single scattering is shown as a solid red arrow and wave. Multiple scattering is represented by dashed, red arrows and waves.*

The desired EXAFS signal χ can be extracted from the raw data by subtracting a structure-less background function μ_0 which represents the absorption of an atom without any neighbors:[77]

$$\chi = \frac{\Delta\mu}{\mu_0}$$

The EXAFS signal can be described by the following formula:[78]

$$\chi(k) = \sum \frac{N \cdot s_0^2 \cdot F(k)}{k \cdot R^2} e^{-2k^2\sigma^2} e^{-\frac{2R}{\lambda k}} \sin(kR + \phi) \qquad (2.1)$$

In this so-called EXAFS equation, the EXAFS signal χ is the sum of all scattering paths. Instead of the kinetic energy, the signal is typically shown as a function of the wave vector k, with $k = 2(m_e(E - E_{kin})/\hbar)^{1/2}$ with the electron mass m_e and the reduced Planck constant$\hbar$. Expressed as a function of k, the EXAFS signal is the sum of different wave functions, each of them stemming from a specific scattering path. Each scattering path is described by its coordination number N, pseudo Debye-Waller factor σ^2 and the radial distance R. The pseudo Debye-Waller factor represents structural disorder, caused for example by thermal motion or crystal lattice distortion. Additionally, the backscattering amplitude F(k), the phase shift ϕ, the electron mean free path λ and the amplitude reduction factor s_0^2, which originates from inelastic interaction of the photoelectron with the absorbing atom, are taken into account.[77] The backscattering amplitude and the phase shift can be calculated with ab initio methods.[79]

From equation (2.1) it becomes clear that the EXAFS signal corresponding to a given coordination shell is the stronger the more atoms are in this coordination shell (in other words, for a higher coordination number N). At high values of R and k the signal is damped due to inelastic scattering of the photoelectron and the finite lifetime of the core-hole, so that EXAFS probes a radius of approximately 6 Å around the absorbing atom and is therefore an inherently local probe.

2.3 XAS data treatment

The extraction of the EXAFS signal $\chi(k)$ from the raw data contains three steps: normalization of the spectrum, background subtraction and Fourier transformation. The data treatment is usually performed by using specialized software, such as IFEFFIT.[80] Figure 2.5 depicts these different data treatment steps, where the raw data is first normalized such that the absorbance below the absorption edge is zero and the absorbance at energies above the edge is oscillating around 1. In the next step, the EXAFS signal is isolated by subtracting a smooth background function from the normalized spectrum. This background function represents the hypothetical signal of an absorber atom without any scattering neighbors. Subsequently, the photon energy E is transformed into the wavenumber k. In the given example, the function was multiplied with k^2 to amplify the part of the spectrum at higher values of k, where the signal is damped. In the final step, the EXAFS signal is Fourier transformed, yielding a complex function.[78] Shown here are the magnitude and the real part of the Fourier transformed EXAFS function.

The Fourier transform of the EXAFS signal is a pseudo radial-distribution function (RDF, see Figure 2.5 d), which contains information on the nature of the atoms surrounding the absorbing atom as well as their number and distance from the absorber. In the example presented here, a RuO_2 sample, the first peak at approximately 1.5 Å corresponds to a Ru-O coordination shell, whereas the signals at approximately 2.8 Å and 3.2 Å correspond to the first and second Ru-Ru scattering shells, respectively. It is important to note that the presented Fourier transform is not phase corrected, meaning that the apparent distances in the graph are not the real atom distances. The phase shift ϕ is represented in the sine function of the EXAFS equation (2.1) and depends on the scattering element and the wave vector k.[79] From the RDF, structural information such as coordination numbers and radial distances is extracted by fitting the experimental data to a theoretical model, which can be based upon a theoretical crystal structure and calculated numerically, for instance using the FEFF code.[81]

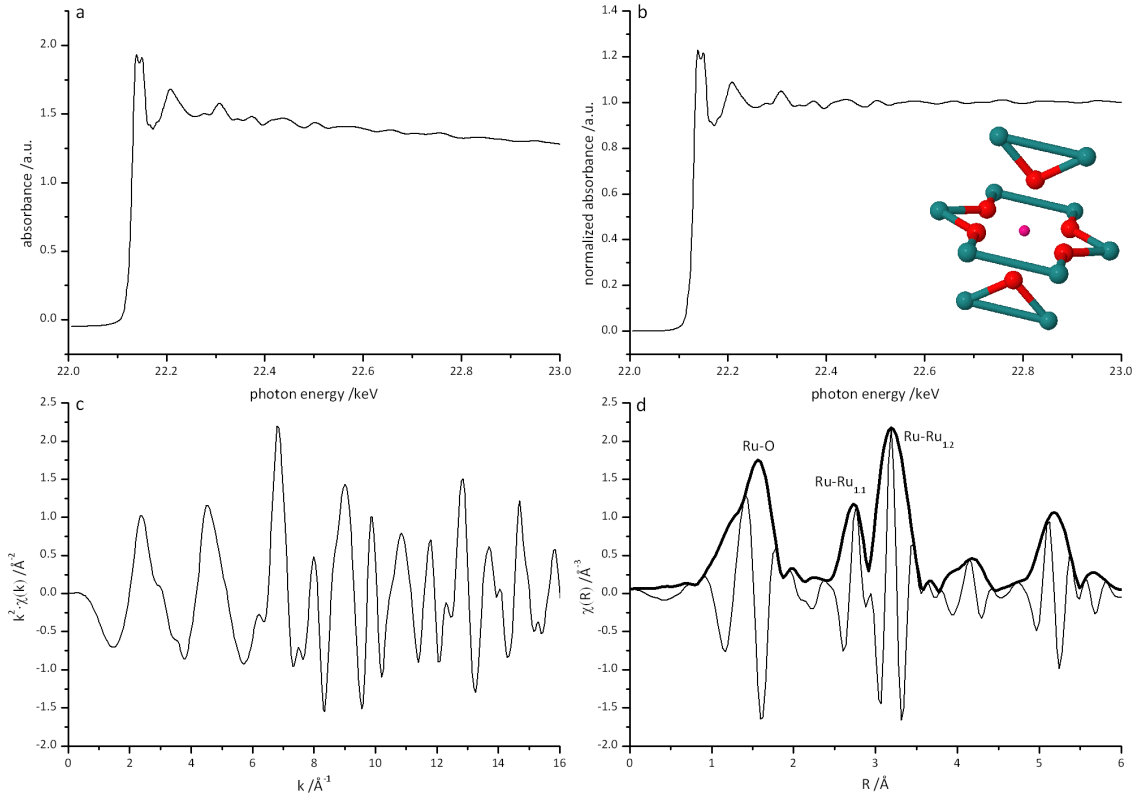

***Figure 2.5**: XAS spectrum of RuO_2. a) The raw absorbance as a function of energy, b) the normalized absorbance as a function of energy, c) the extracted EXAFS signal, d) the Fourier transform. The inset in b) shows the absorber atom (pink) with the first scattering shell of 6 oxygen atoms (red) and higher scattering shells with 4 and 6 Ru atoms, respectively (turquoise).*

2.3.1 Fitting EXAFS data to a theoretical model

To extract structural information from a XAS spectrum, such as the type of elements surrounding the absorbing atom, their coordination number (N), distance (R) and pseudo Debye-Waller factor (σ^2), a fit of the EXAFS signal χ(k) to a theoretical model is performed. For instance, this can be done with ARTEMIS which is part of the IFEFFIT software suite.[80,82] A model based on known crystal structures (e.g. from the ICSD - Inorganic Crystal Structure Database, FIZ Karlsruhe, Germany[83]) is converted to an input file for the FEFF code.[81] From this structural information, FEFF calculates theoretical scattering paths around a chosen absorbing atom, with their respective coordination numbers, bond distances, scattering amplitudes and phases.

The mathematical representation of this model is essentially a function like the EXAFS function (see equation (2.1)) with five free parameters:
The coordination number (or degeneracy) N, the amplitude reduction factor s_0^2, the radial distance R, the Debye-Waller factor σ^2 and a correction term for the edge energy ΔE_0. Since N and s_0^2 are correlated, one of them needs to be set to a fixed value. Typically, s_0^2 is derived by fitting the XAS spectrum of a reference material (often a standardized sample pellet or metal foil) with N set to its literature value and then used for the fit of the sample. The software (e.g. IFEFFIT) then runs a minimization routine, so that the difference between the data and the model function (e.g. $\chi^2 = \frac{P_{idp}}{P\varepsilon^2}\sum_{i=1}^{N}\{[Re(f_i)]^2 + [Im(f_i)]^2\}$) is minimized. In other words, the free parameters are changed such that the model fits to the data. In the expression of χ^2, f_i is the complex function that is to be minimized with its real and imaginary parts, P is the number of data points in the chosen R-space range, P_{idp} is the number of independent points in the data range and ε is the average uncertainty of the experimental data.[84] The number of independent points P_{idp} depends on the data range in k-space and in R-space that is used for the fit (Nyquist theorem):[85]

$$P_{idp} = \frac{2(k_{max} - k_{min})(R_{max} - R_{min})}{\pi} + 2.$$

To obtain a reliable fit, it is best practice to keep the number of free parameters in the fit at less than half of P_{idp}. This means that a large region in k-space will allow for more fit variables to be used, hence, high spectra quality up to high k-values is required for more complex fit models. In principle, EXAFS fitting can be performed both in k-space or R-space. Running the fitting routine in R-space has the advantage that single scattering shells can be selectively fitted by multiplying a window function around the peak of choice, filtering out the rest of the data.[77] In order to reduce the number of free parameters of the fit, parameters can be fixed or related to each other. Furthermore, mathematical relations between parameters can be implemented which further reduce the number of free parameters. As an example, this could be the assumption of isotropic expansion or contraction in the sample, expressed as a relationship between the bond distances R of several scattering paths. To determine the accuracy of EXAFS fitting, Li et al. compared experimental data with calculated spectra and found that the error in the obtained coordination numbers is generally below 10 % and approximately 0.005 Å for the bond distances.[86]

2.4 A typical layout for in situ XAS experimentation

A basic layout of a beamline equipped for X-ray absorption spectroscopy is shown in Figure 2.6. The polychromatic X-ray beam coming from the storage ring is reflected by a mirror which collimates the beam. In a monochromator, typically a parallel set of polished crystals with a specific crystal cut, the beam is monochromatized and a specific wavelength selected. The X-ray beam is then focused by another mirror. The beam passes through a first ionization chamber I_0 which measures the incident beam intensity. Behind the sample, depicted as a tubular reactor filled with a catalyst, the beam intensity is recorded by a second ionization chamber I_1.

A metal foil is often used for simultaneous energy calibration by placing it between I_1 and a third ionization chamber I_2. Ionization chambers are gas-filled chambers with two parallel electrodes between which a static high voltage is applied. A fraction of the gas is ionized by

the X-rays and the ions are collected at the anode, creating a measurable current that is proportional to the X-ray intensity.

For in situ studies of heterogeneous catalysis, as presented in this thesis, a reactor is used which needs to be stable under reaction conditions (i.e. high temperatures and pressures) and sufficiently X-ray transparent at the required photon energy. For high temperature/pressure conditions, ceramic reactor or window materials are often used. The reactor is filled with the catalyst sample, brought to reaction conditions and reactants of interest are passed through the catalyst bed. Concomitant measurement of reaction products by effluent analysis at the reactor outlet and the catalyst's structure via XAS allows for mechanistic insight by studying structure-reactivity relationships.

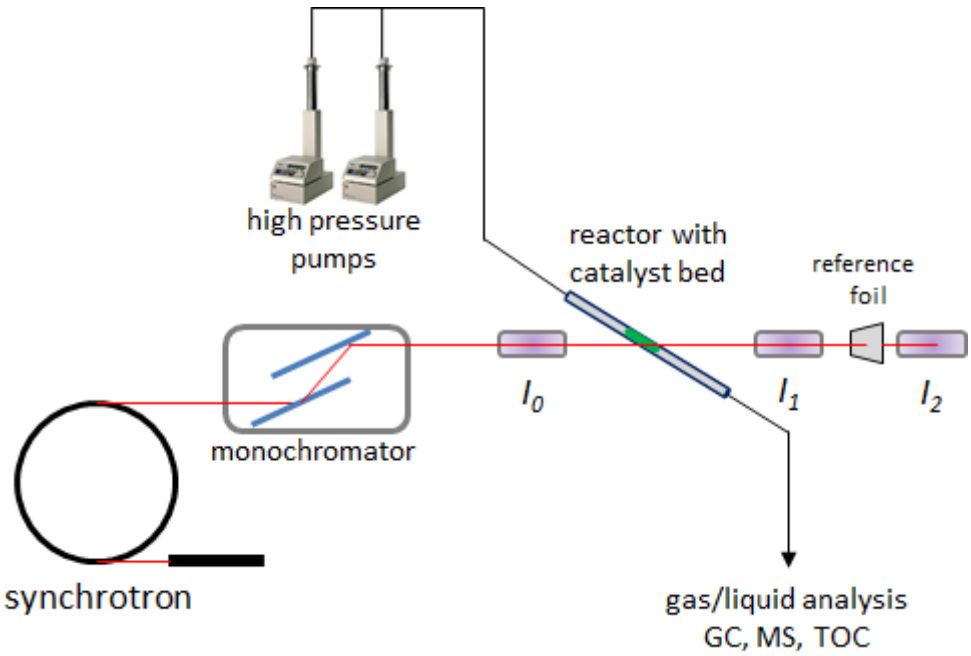

***Figure 2.6**: Schematic of a typical in situ experiment at a XAS beamline. X-ray radiation from the synchrotron is monochromatized and the ion chambers as well as the reactor are aligned with the X-ray beam. High pressure pumps feed liquid reactants to the reactor where they pass through the catalyst bed. A reference foil is placed between I_1 and I_2 for the purpose of energy calibration.*

Chapter 3

Review of previous results from the SCWG of ethanol and design of a bench-top setup for gasification in SCW

Abstract

This chapter encompasses a short review of previous results obtained by Rabe et al. at the Paul Scherrer Institute that suggested an oscillatory nature of the gasification of ethanol in supercritical water.[46] It outlines how the observed fluctuations in product gas composition are caused by the slug flow of the gas/liquid effluent in the used setup and that they are independent of the gasification reaction. Based on this, the entire setup – composed of feed and effluent capillaries, valves and the reactor itself – has been improved to limit the occurrence of product gas fluctuations.

Parts of this chapter were published in a Corrigendum to the original publication of Rabe et al. as *S. Rabe, M. Nachtegaal, T. Ulrich and F. Vogel, Angewandte Chemie Intl. Ed. 51 (2012), 2533*.[87]

3.1 Review of previous results

In ethanol gasification experiments conducted by Rabe et al. at the Paul Scherrer Institute in 2008, the evolution of product gas showed a periodic behavior in terms of flow rate and gas composition (Figure 3.1).[46] Both the gas flow rate as well as the gas composition oscillated strongly, with concentration maxima of CH_4/H_2 and CO_2 being phase shifted by about 180° with respect to each other. Also, at high CH_4/H_2 concentrations in the product gas, the gas flow rate showed a maximum. As an explanation for these phenomena the possibility of an oscillating reaction on the catalyst's surface was debated, during which organic adsorbates (mainly acetaldehyde), accumulated on the catalyst's surface, are quickly converted to gaseous products, followed by anew accumulation of organic adsorbates. For a full interpretation of these results and the suggested reaction mechanism, the reader is referred to the original publication by Rabe et al.[46]

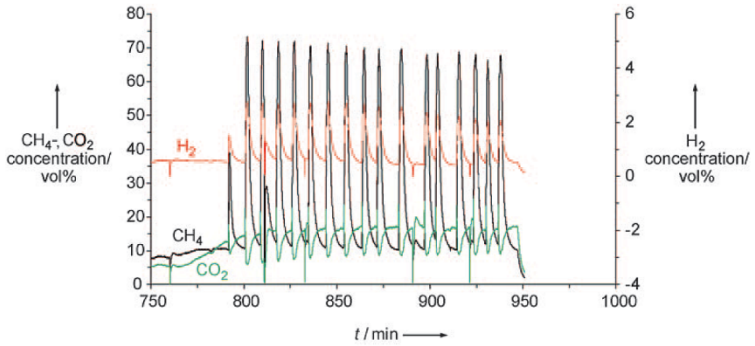

***Figure 3.1**: Oscillating gas composition during gasification of 5 wt% of ethanol in water at temperatures between 350°C and 390°C. Adapted from Rabe et al.*[46]

A sketch of the setup used by Rabe et al. is depicted in Figure 3.2. It consisted of an HPLC pump which fed water or EtOH/water mixtures at 25 MPa into a tubular sapphire reactor with dimensions 200 × 5 × 3.48 mm. After the reactor, the effluent passed through a series of filters and valves before being allowed to expand to ambient pressure in a back pressure regulator. The product gases were then separated from the liquid effluent in a phase separator.

This setup was put into operation again to verify the results obtained by Rabe et al., the only difference being that the tubular sapphire reactor was replaced by a tubular stainless steel (SS 316L) reactor with similar dimensions (300 × 6 × 4 mm) to guarantee a safe bench-top operation. In a series of experiments, ethanol was gasified over a fixed bed of Ru/C in supercritical water at 400°C and the aforementioned oscillations in product gas evolution were readily observed. However, it became apparent that their frequency and magnitude strongly depended on the orientation of the various pipes and valves downstream of the reactor (e.g. whether they were level or pointing upwards or downwards).

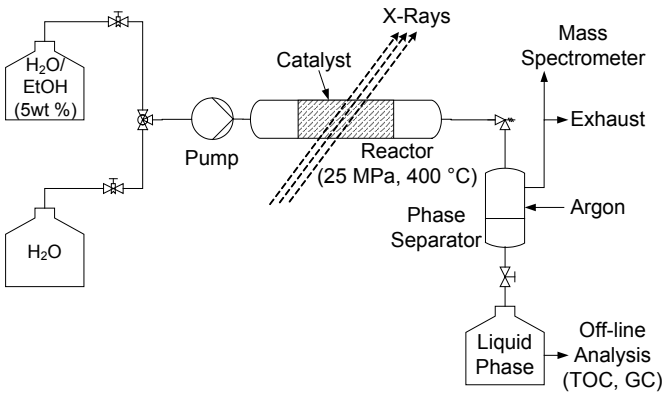

Figure 3.2: *High pressure continuous flow fixed-bed XAS setup. Adapted from Rabe et al.*[46]

To investigate the role of dead volumes in the setup (caused by the large diameter of the installed pipes and valves), all filters and valves downstream of the reactor were removed from the setup, the reactor now being directly connected to the back-pressure regulator by a 1/16 inch stainless steel capillary. With the modified setup, it was possible to control the fluctuations in gas production by simply tilting the back-pressure regulator upwards or downwards (in other words, the outlet of the back pressure regulator facing upwards or downwards; see Figure 3.3).

The cause for this effect lies in the 2-phase gas/liquid effluent that is present in the pressurized pipes and capillaries downstream from the reactor. While the gasification of organics in the feed takes place in a uniform supercritical phase, the product gases and water separate as soon as the effluent temperature falls below the critical temperature of water. The produced methane and hydrogen hardly dissolve in water whereas CO_2 dissolves

well in pressurized water.[88] Thus, a slug flow of pressurized CH_4/H_2 and CO_2-rich water is moving through the capillaries, leading to the successive escape of pressurized CH_4/H_2 and CO_2-rich water from the back-pressure regulator. Here, a bubble of compressed gas will expand to a large volume, causing the observed sharp increase in product gas flow and CH_4/H_2 concentrations. On the other hand, when the liquid phase is passing through the valve, only a very low gas flow (due to the evolution of previously dissolved CO_2) can be observed. Due to the low feed flow rate of 0.5 ml/min, these fluctuations are then well resolved in a gas flow vs. time graph. Thus, the true gas composition is only obtained by calculating the time average over a large enough number of oscillations.

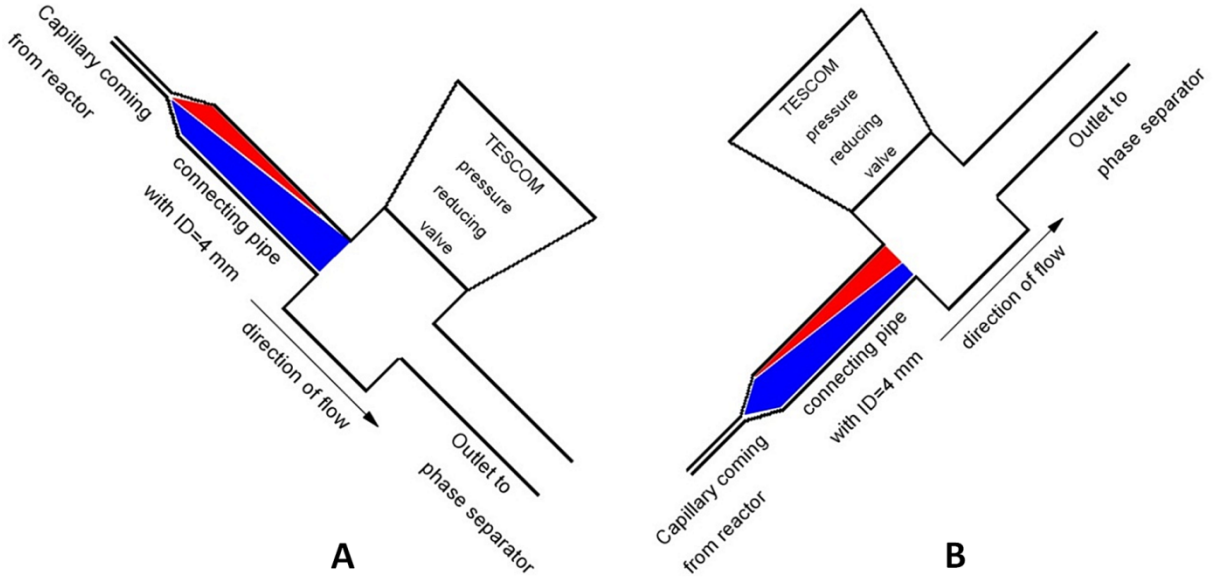

***Figure 3.3**: Distribution of compressed gases (red) and liquid effluent (blue) in a back pressure regulator with attached piping during downwards (A) and upwards (B) tilt.*

Since the density of the compressed CH_4/H_2 is smaller than that of water, methane and hydrogen will accumulate in a non-level pipe of sufficient inner diameter, remaining at its upper end, whereas the H_2O/CO_2 phase will pass through unhindered (Figure 3.3). By tilting the back-pressure regulator downwards it is possible to collect CH_4 and H_2 within the setup for a certain amount of time, during which a stable and very low gas flow are observed (runtime 80 to 95 min; Figure 3.4). During this time, the system pressure also stabilizes, since the liquid-only phase is moving smoothly through the back-pressure regulator without

causing drops in system pressure. After a while, the accumulation of compressed gas in the setup reaches a spill-over point and the oscillations start again, despite the downwards-tilt of the setup (runtime 95 to 170 min; Figure 3.4). Now, by tilting the back-pressure regulator upwards, the collected gases are suddenly released, resulting in a gas flow three times higher than average (runtime 170 to 175 min; Figure 3.4).

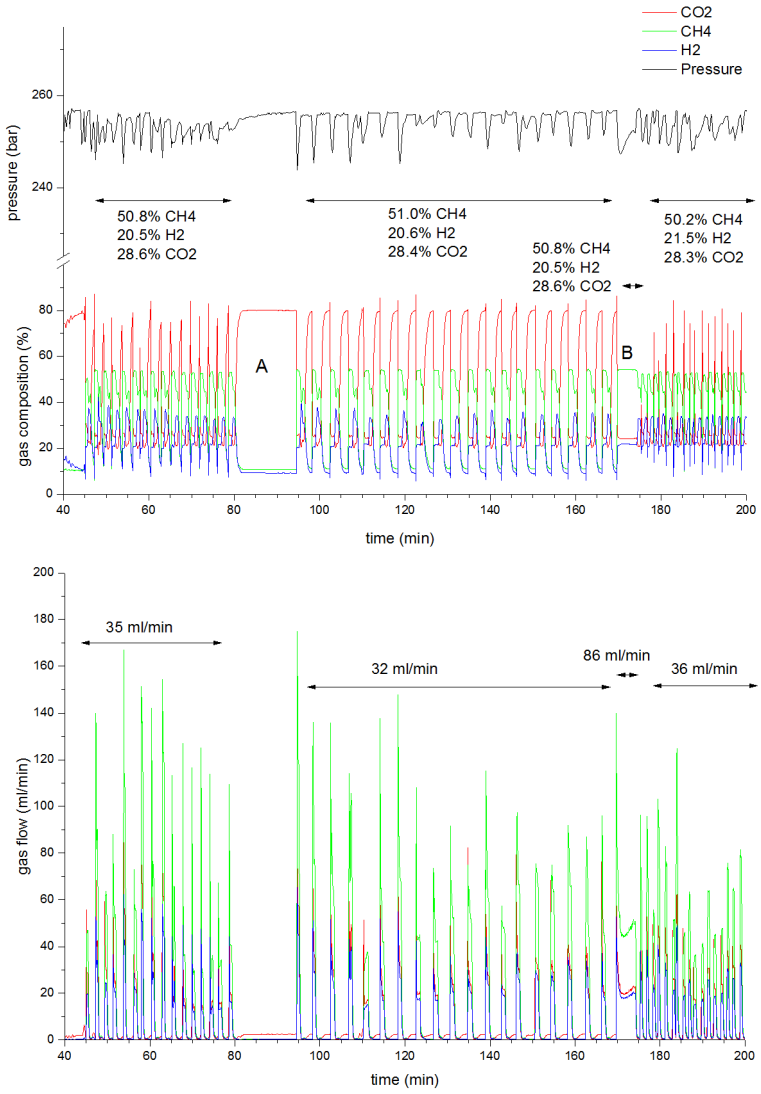

Figure 3.4: *Gas flow and composition of product gas during gasification of 4.8% ethanol in water at 25 MPa and 400°C (experiment C-1). During the gasification, the back pressure regulator was tilted downwards (A; runtime 80 to 95 min) and upwards (B; runtime 170 to 175 min). The product gas flow rates and gas compositions were obtained by integrating and averaging over the time span indicated by the arrows.*

Based on these results, it is safe to conclude that the observed oscillations in product gas flow and composition are of systemic and not of chemical origin. Therefore, the hypothesis of an oscillating reaction on the catalyst's surface and the proposed reaction mechanism for ethanol gasification in SCW are not supported by the experimental data. Rabe et al. determined the active catalyst phase as metallic Ru via in situ XANES. The observed state of the Ru catalyst under reaction conditions is independent of the proposed reaction mechanism and remains true.

3.2 Design of an improved bench-top setup for gasification of model biomass in SCW

3.2.1 Improving the high pressure liquid flow setup

Although fluctuations in the product gas composition and flow rate – due to the slug flow described earlier – cannot be avoided entirely, the setup can be optimized in terms of dead volume and arrangement of various parts such as valves and pressure gauges. The setup was improved by using 1/16 inch stainless steel capillaries wherever possible in order to decrease the dead volume of the setup and to increase the flow velocity of the feed before and after the reactor. As a result, time lags such as the one between formation of product gases in the reactor and their detection in the mass spectrometer (MS) are reduced. Relief valves and pressure gauges (both having large inner diameters) were decoupled from and placed below the main effluent capillary in order to avoid gas accumulations in these parts (see Figure 3.5).

The key components of the improved, continuous flow setup are two syringe pumps (Model 260D, Teledyne-ISCO, USA) that allow pumping liquids and viscous slurries with a flow rate precision of 5 µl/min at pressures up to 60 MPa. In contrast to HPLC pumps that were used in previous setups, these pumps do not cause any pressure fluctuations. Furthermore, the pressure sensors of the pumps record the system pressure upstream of the reactor. The two syringe pumps are linked to the feed capillary by a switch valve allowing for remote switching between different feeds. The switch valve is directly connected to the reactor,

after which the effluent passes through a heat exchanger and a particle filter (pore size 5 micron). At this point, a tee junction connects to a safety valve and a pressure sensor that records the system pressure downstream of the reactor. The final component of the setup is a high precision back-pressure regulator, optimized for low flow rates (Model 26-1700, TESCOM, USA), where the effluent stream is allowed to expand directly from system to ambient pressure. Gaseous reaction products are then segregated from the liquid phase in a phase separator. Here, liquid samples can be taken for further analysis. A mass spectrometer (Quadstar 32, Pfeiffer, Germany) is connected directly to the phase separator in order to monitor the product gas composition online. In experiments involving isotope labeling of the product gases (see chapters 6 and 7), a tube filled with calcium chloride was installed between the phase separator and the MS in order to remove water from the product gas. For a precise quantitative gas analysis, product gases were also collected in a gas bag and analyzed offline with a gas chromatograph (HPHP 6890 Series with HP 1, AT 5 and PLOT Q columns). This setup generally accepts any type of reactor with Swagelok® connections and was used for bench-top operation with tubular reactors made from stainless steel (see section 3.2.2) as well as with ceramic AlN reactors for in-situ XAS measurements (see chapter 4).

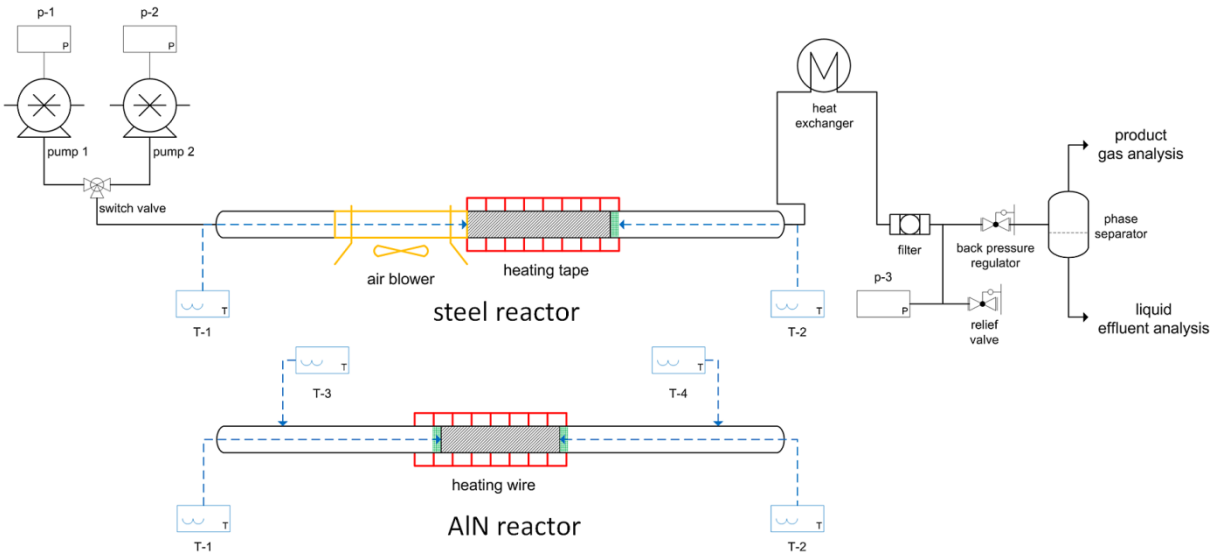

***Figure 3.5**: Sketch of the entire liquid flow setup that was used with both steel reactors for bench-top operation and AlN reactors for in-situ XAS measurements. T-x designates installed thermocouples, p-x the installed pressure gauges.*

3.2.2 Design of a tubular stainless steel reactor for bench-top operation

For bench-top experimentation, a simple, safe and inexpensive reactor design was desired that can hold a sufficient amount of catalyst as a fixed bed and can be operated under supercritical water conditions. A stainless steel (SS 316L) capillary with dimensions 300 × 6 × 4 mm was used as reactor material and equipped with Swagelok® fittings that allow for a fast and simple connection to the liquid flow setup outlined above. The reactor was designed to accommodate a catalyst bed of up to 30 mm in length which is held in place by a stainless steel frit that is fixed in the reactor tube (Figure 3.6). The temperature before and behind the catalyst bed is recorded by two thermocouples. A hot air blower heats the reactor tube on a length of about 40 mm in front of the catalyst bed and thus preheats the feed before it reaches the catalyst. The catalytic zone of the reactor is enveloped in an electric heating tape. The two heating systems offer a good flexibility in terms of fine tuning the reaction temperature inside the reactor, in particular to match the temperatures before and after the catalyst bed. Furthermore, the heating power is increased and feed flow rates of up to 2 ml/min can be used, decreasing fluctuations in product gas evolution and allowing for variation of the feed residence time in the reactor.

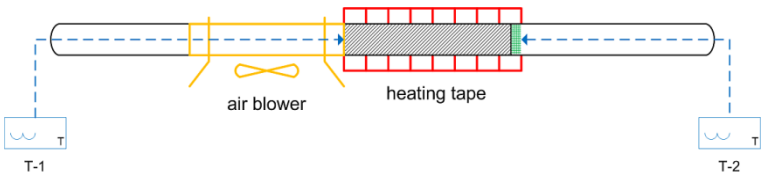

***Figure 3.6**: Tubular stainless steel reactor with two heating zones. Thermocouples are installed in front of and behind the catalyst bed (shaded grey). A stainless steel frit (15 µm pore size, green) downstream of the catalyst holds the catalyst bed in place. Direction of flow is from left to right.*

3.3 Conclusions

The oscillating fluctuations in gas production and gas composition during the SCWG of ethanol, observed by Rabe et al., were caused by the slug flow of compressed gas and liquid water in the reactor effluent. The reaction mechanism that was suggested to explain this allegedly oscillating gasification reaction is therefore not supported by the experimental results anymore. The liquid flow setup, both up- and downstream of the reactor, was revised in order to limit the occurrence and magnitude of these fluctuations. However, as the slug flow of gas and liquid cannot be avoided, fluctuations in the observed product gas flow will always occur to a certain extent, particularly at low gas production and liquid flow rates. Using product gas analysis alone to deduce a reaction mechanism is therefore not viable and more sophisticated (in situ) methods that probe the catalytic reactions directly will be necessary.

A versatile setup for bench-top gasification experiments in SCW was designed, including a tubular stainless steel reactor with two heating zones that allows for flow rates up to 2 ml/min at 400°C and for adjusting the reaction temperature before and after the catalyst bed separately. Due to the small scale of the reactor, high heat up and cool down rates can be realized, allowing for efficient experimentation. This setup can be used to study the gasification of organic model compounds, sulfur poisoning, coke formation and catalyst regeneration.

Chapter 4

Design of a continuous-flow reactor for in situ X-ray absorption spectroscopy of solids in supercritical fluids

Abstract

This chapter presents the design and performance of a novel high-temperature and high-pressure continuous-flow reactor which allows for X-ray absorption spectroscopy or diffraction in supercritical water and other fluids under high pressure and temperature. The use of boron carbide and aluminum nitride as reactor materials is discussed. The final design of the in-situ cell consists of a tube of sintered, polycrystalline aluminum nitride (AlN) which is tolerant to corrosive chemical media and was designed to be stable at temperatures up to 400°C and pressures up to 30 MPa. The performance of the reactor is demonstrated by measurement of extended X-ray absorption fine structure (EXAFS) spectra of a carbon-supported ruthenium (Ru/C) catalyst during the continuous hydrothermal gasification of ethanol in supercritical water (SCW) at 400°C and 24 MPa.

Parts of this chapter were published as *M. Dreher, E. De Boni, M. Nachtegaal, J. Wambach and F. Vogel, Review of Scientific Instruments 83 (2012), 054101*.[89]

4.1 Introduction

X-ray absorption spectroscopy (XAS) is a powerful technique for obtaining local geometric (up to 6 Å) and electronic structural information about the X-ray absorbing atoms.[90] On the other hand, X-ray diffraction (XRD) provides information about crystalline phases (long range order) and lattice parameters of solid samples.[91] Owing to the large penetration depth of (high energy) X-ray radiation, XAS and XRD can be applied in situ in the presence of gaseous or liquid reactants and solvents, using X-ray transparent cells or windows that are able to withstand the high temperatures and pressures necessary to reach supercritical conditions. Amongst the commonly used supercritical fluids (water, CO_2 and NH_3), SCW presents the greatest challenge in terms of cell design, due to its critical parameters (p_c = 22.1 MPa, T_c = 374°C) and its corrosive nature.

In particular, a cell that enables measuring XAS and XRD under typical SCW conditions needs to fulfill five main requirements:

(1) mechanical strength to withstand operating pressures of up to 30 MPa

(2) mechanical and thermal stability at temperatures up to 500°C

(3) resistance to corrosion under hydrothermal conditions

(4) absence of crystallinity that could cause additional diffraction of the X-rays

(5) sufficient X-ray transmittance at the desired photon energy.

In the field of catalysis it is furthermore desirable to investigate the catalyst during continuous operation whilst applying different reaction conditions such as flow rate, temperature, pressure or variation of reactants. For catalysis under supercritical conditions, this requires a continuous flow reactor that fulfills all of the above requirements. In addition, the reactor must allow for intimate contact of the supercritical fluid with the catalyst which is usually achieved by operating the reactor in a “fixed bed” mode. In fixed bed mode, the catalyst is placed and secured as a closely packed bed of fine particles within the tubular reactor.

Grunwaldt and Baiker reviewed the requirements that need to be taken into account when designing in situ XAS cells for catalytic reactions in supercritical fluids.[92] A comprehensive review of existing XAS cells for high temperature/high pressure (HT/HP) catalytic fluid phase reactions as well as suitable materials was published by Kawai et al.[93]

Nearly all in situ XAS cells for HP/HT application found in literature are of the diamond-anvil type or batch reactors with X-ray windows made from various materials such as Be, diamond, silica or graphite.[94–96] One of the most versatile and complex X-ray transparent batch reactors for in situ XAS and X-ray emission spectroscopy (XES) under SCW conditions has been designed by Testemale et al. and has been used extensively for geochemical applications.[97–100] However, batch reactors do not allow for continuous flow operation, making it impossible to study catalysts under steady state or transient conditions. A promising in situ XAS cell for continuous flow operation was developed by Kawai et al. who studied hydro-desulfurisation reactions over Ni catalysts in hot oil at 450°C and 3 MPa using cubic boron nitride as X-ray windows.[93] However, their reactor can only resist pressures up to 10 MPa which is not sufficient to reach SCW conditions. Furthermore, boron nitride does not seem to be chemically stable in SCW.[101–103]

A general drawback of using reactors with X-ray windows for catalytic reactions is the limitation of being able to probe the catalyst only in one spot. For studying catalytic reactions in detail it can be necessary to probe the catalyst at different positions along the catalyst bed which requires a reactor that is X-ray transparent along its entire length.

In this chapter a novel type of X-ray transparent, continuous flow reactor is introduced, using polycrystalline AlN as a reactor material which is able to withstand SCW conditions. As an example for its performance, we present the first extended X-ray absorption fine structure spectra of an active heterogeneous catalyst recorded under these conditions.

4.2 Strategy for cell construction

4.2.1 Choice of cell material

Prospective materials for the construction of a continuous flow reactor that allows for in situ XAS acquisition under SCW conditions need to fulfill a number of requirements in terms of mechanical strength and chemical inertness, as outlined in the introduction. Generally, many metals and metal alloys fulfill the conditions of mechanical strength, temperature stability and resistance to corrosion, but have poor X-ray transmittance, with the exception of beryllium which should be avoided for safety reasons. This leaves ceramic materials as possible construction materials for an in situ cell. To keep the X-ray attenuation at a sufficiently low level, the ceramic material should be composed of light elements (e.g. up to Al). Furthermore, a high mechanical stability is necessary in order to enable operation under SCW conditions (here: 400°C, 25 MPa) whilst keeping the wall thickness of the reactor tube at a minimum. The acceptable wall thickness correlates with the X-ray transmittance of the material in the desired photon energy region which should be as high as possible in order to ensure high data quality of the acquired XAS spectra at short acquisition times.

Finally, a material with good thermal conductivity is desirable in order to guarantee a quick heat transfer from the heating to the inside of the reactor and an even heat distribution along the catalyst bed. Figure 4.1 gives an overview on typical ceramic materials used for construction of X-ray transparent cells and reactors.

	density [g·cm^{-3}]	thermal conductivity [W·m^{-1}·K^{-1}]	thermal expansion [K^{-1}]	Young's modulus [Gpa]	crystallinity[a]
c-BN	2.2	740	3.8 ppm	850	poly
B_4C	2.52	42	4.78 ppm	450	poly
AlN	3.25	200	4.2 ppm	345	poly
sapphire	3.97	42	5.3 ppm	470	SC
SS 316L	7.95	16.2	9.7 ppm	193	poly

[a] poly: polycrystalline, SC: single crystal

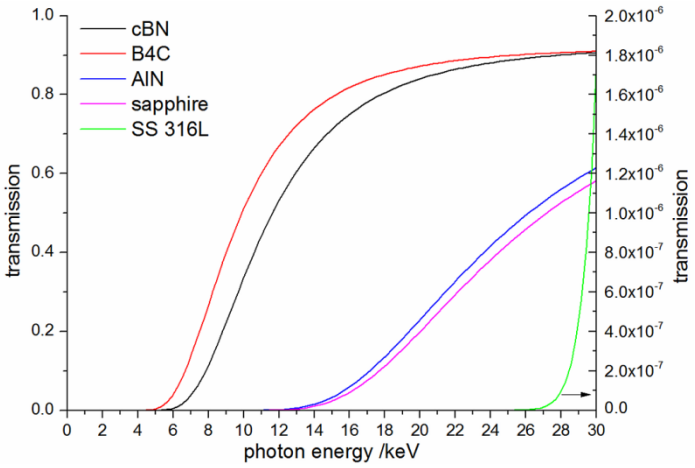

***Figure 4.1**: Comparison of mechanical properties and X-ray transmission (material thickness: 2 mm) for typical materials used in the construction of X-ray transparent reactors or cells.*[72,104] *Stainless steel 316L is shown for comparison.*

4.2.2 Boron carbide

With the above prerequisites in mind, boron carbide was selected as a prospective reactor material due to its high mechanical strength and superior X-ray transmittance (Figure 4.2). A material sample (tubular geometry with an outer diameter of 10 mm and inner diameter of 4 mm) was obtained from *ESK Advanced Technical Ceramics* (Kempten, Germany) to conduct first tests. A piece of the boron carbide tube was exposed to SCW in a stainless steel batch reactor at 400°C for 8 hours and the mass loss detected by weighing. A mass loss on the order of 62 ppm/h was detected, indicating that boron carbide is not chemically stable even in pure SCW (its instability in more aggressive supercritical media has already been reported in literature).[101] However, this mass loss would be acceptable for short term experiments in the range of up to 24 hours and if the boron compounds that are leached from the reactor walls do not interfere with the studied reaction or catalyst.

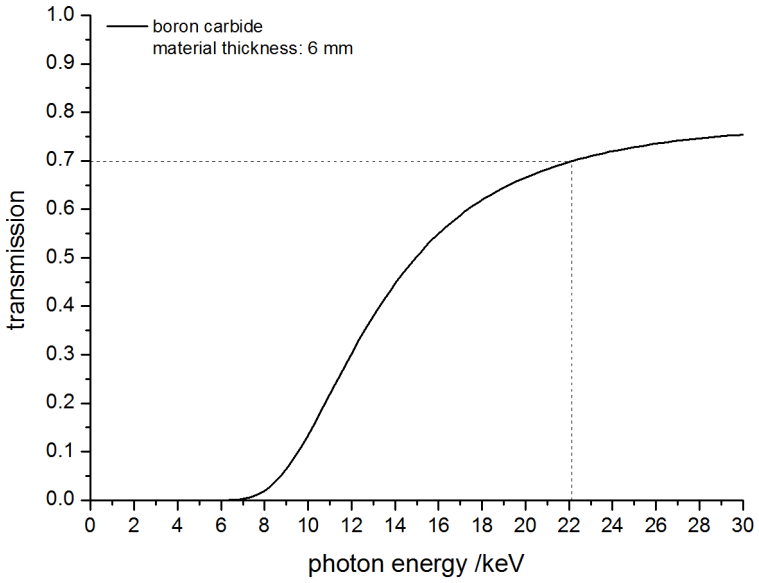

***Figure 4.2**: Calculated transmission of a boron carbide tube with a material thickness of 6 mm. The transmission at the Ru K-edge energy of 22.117 keV is indicated by dashed lines.*[72]

For reactor construction, boron carbide tubes with dimensions of 150 x 10 x 4 mm were obtained from *ESK Advanced Ceramic Materials* (Kempten, Germany) with 150 mm being the maximal tube length that could be manufactured. For connecting to a high pressure setup, a ceramic tube can be relatively easily glued into metal casings that serve as a connection to typical high pressure adapters, such as Swagelok® fittings. For the metal casings, a Fe-Ni-Co alloy (Kovar) was used which has a coefficient of thermal expansion that closely resembles that of boron carbide.

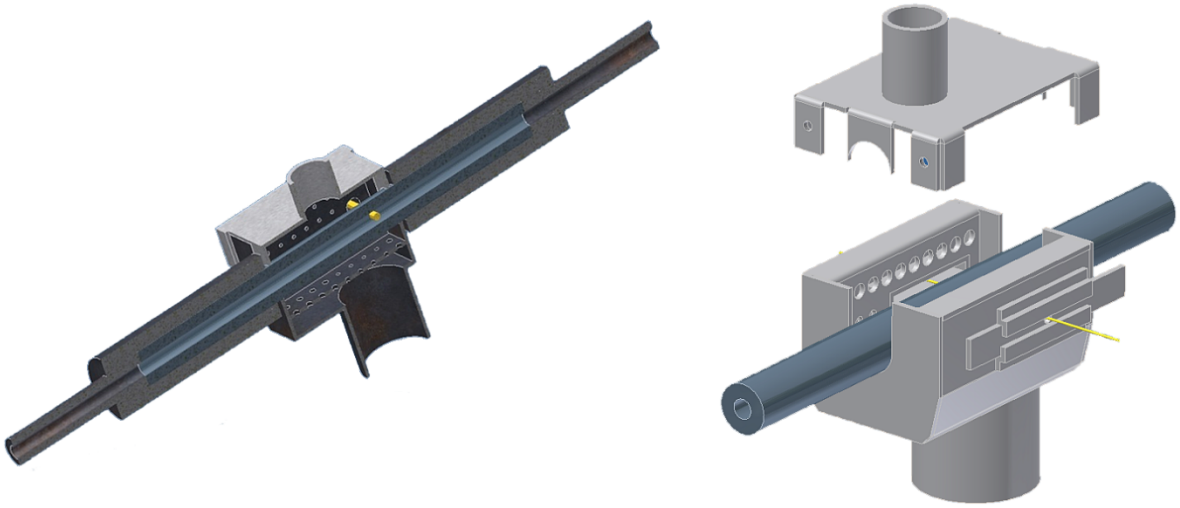

Figure 4.3: *Left: design draft for a boron carbide reactor with a tube length of 150 mm: Kovar steel casing (grey), boron carbide tube (blue-grey), heating chamber (dark grey) with lid (light grey), X-ray beam (yellow). Right: detail view of the heating chamber.*

Typically, high performance epoxide glues are used for this purpose. However, due to the limited tube length and a required gluing zone of at least 4 cm at each end, only about 7 cm in the center of the reactor tube were available as a heating zone. A heating chamber, operated by a hot air blower, was designed to envelop this part of the tube (Figure 4.3). Since the center of the reactor needs to be heated up to 400°C for operation under SCW conditions, it is impossible to keep the steel casings and thus the glue cool enough to maintain its strength. Therefore, organic glues were not an option for this reactor design. However, epoxide glue was used for a pressure test at room temperature which showed that the boron carbide tubes can withstand pressures of at least 30 MPa (testing at higher pressures was not possible due to limitations of the used HPLC pump).

As a substitute for epoxide glues, several high temperature adhesives (based on aluminum oxide or silica), able to withstand temperatures of up to 800°C, were used to fix the boron carbide tube in the steel casings. However, these glues failed to deliver a tight connection between the boron carbide and the steel casings, leading to leakages at pressures higher than 1 MPa.

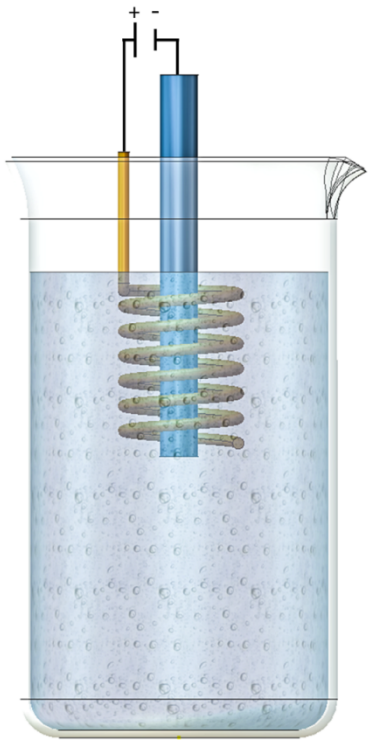

***Figure 4.4**: Sketch of the electrochemical cell that was used for copper-coating of boron carbide tubes, using a commercial copper sulfate electrolyte (RI 375, RIAG Oberflächentechnik AG, Switzerland). The boron carbide tube (cathode) was closed at the bottom and surrounded by a spiral made of 3 mm thick copper wire (anode, grade DHP) at a distance of 15 mm. During copper deposition, the electrolyte was vigorously stirred (magnetic stirrer) and nitrogen was bubbled through. For coating the boron carbide tube over a length of 40 mm, a current of 0.32 A at a voltage of 0.7 V was applied, resulting in a deposition rate of about 42 µm/h.*

Another attempt to fix a boron carbide tube in a Kovar steel casing was made by using the technique of vacuum soldering to create an intimate connection between ceramic and steel. Since this technique requires a thin layer of copper to be deposited on the ceramic material first, an electrochemical cell was designed to coat boron carbide with copper (exploiting the fact that boron carbide is a conductive material and can be used as an electrode; Figure 4.4). After successfully coating boron carbide with a thin layer of copper (Figure 4.5), the coated tube was soldered into Kovar steel casings, using a nickel based solder at 980°C. However, at this temperature the copper film was ripped off of the boron carbide tube due to the different thermal expansion coefficients.

Figure 4.5: *Boron carbide tube, coated with about 100 µm of copper. Grooves (500 µm deep) were cut into both ends to improve the interlocking between solder material and boron carbide.*

In a final attempt to create a high pressure connection to the boron carbide tube, a 1 mm thick layer of copper was electrochemically deposited at both ends of the tube in order to directly apply a 12 mm Swagelok fitting onto the coated tube (Figure 4.6). Pressure tests at room temperature showed that the copper-boron carbide joint was stable enough to withstand pressures of up to 30 MPa. When heat was applied to the center of the tube, water started to leak from the ceramic-copper interface. Upon cooling down, the leakages disappeared again, suggesting that the different thermal expansion coefficients of boron carbide and copper do not allow for operation at elevated temperatures. As a consequence, and due to the lack of longer boron carbide tubes that would allow for the use of epoxide glues, this material was abandoned for reactor construction.

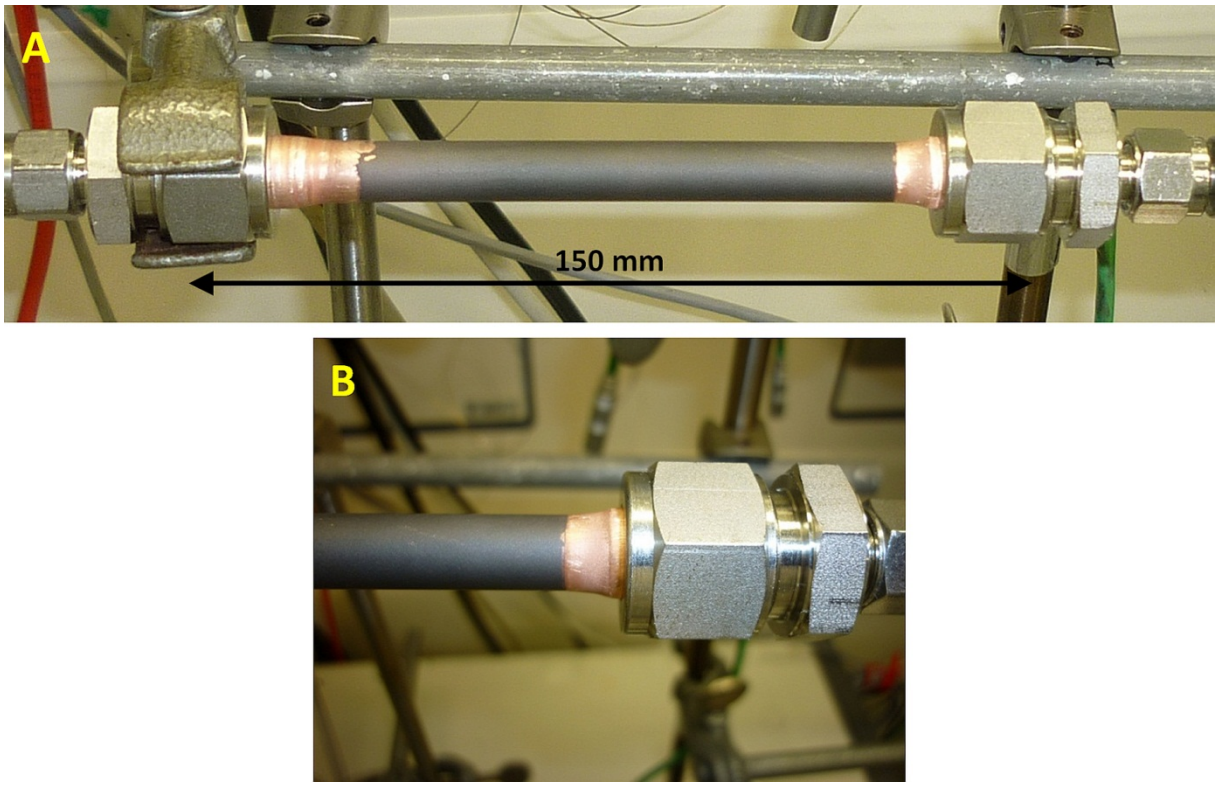

***Figure 4.6**: Boron carbide tube with 1 mm copper coating and Swagelok® fittings (A). Close-up of the connection (B).*

4.2.3 Aluminum nitride

Boukis et al. conducted an extensive study on the corrosion resistance of several steel alloys and ceramics under hydrothermal (SCWO) conditions.[101–103] Of the ceramic materials composed of relatively light and thus X-ray transparent elements, tested in these studies, sapphire and aluminum nitride (AlN) proved to be very stable in supercritical water. Due to its high mechanical strength and corrosion resistance, sapphire is an excellent material for high pressure cells.[46,105] However, its crystalline nature causes X-ray diffraction that interferes with the XAS signal and limits the analysis of the spectra to the position of the absorption edge (determination of oxidation state, see Figure 4.7).[46] This leaves aluminum nitride as the material of choice, presenting a mechanical strength similar to sapphire and exceptionally high thermal conductivity.[106] Furthermore, it transmits X-ray radiation without causing diffraction, due to its polycrystalline nature (Figure 4.7).

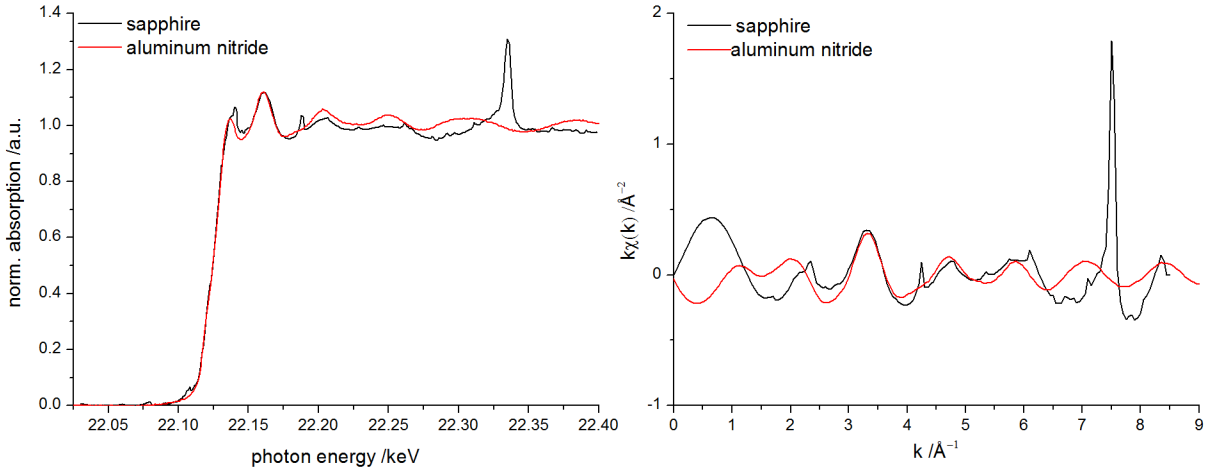

***Figure 4.7**: Comparison of XAS spectra of a Ru/C catalyst in sapphire and aluminum nitride tubes, respectively. Strong X-ray diffraction peaks, caused by the crystalline sapphire, can be observed both in the raw data (left) and the extracted EXAFS data (right), whereas aluminum nitride allows for recording a clean EXAFS spectrum.*

For these reasons, tubular aluminum nitride was selected as the material of choice for reactor construction. A tubular design, where the entire reactor is made of an X-ray transmitting material, has a clear advantage over window-type reactors: it allows for spatial resolution along its entire length.

It needs to be noted, though, that the X-ray attenuation of AlN is still relatively high compared to materials like beryllium or boron carbide. The energy dependence of the X-ray transmittance of a tubular AlN reactor with a wall thickness of 1.25 mm, as developed in this study, is shown in Figure 4.8.[72] At a photon energy of 18.5 keV, only 10% of the photons are transmitted through the reactor walls and transmission quickly decreases to zero at lower energies. Therefore, the proposed reactor design (inner diameter of 3.5 mm, outer diameter of 6.0 mm) limits fast EXAFS spectroscopy (with acquisition times of a few minutes) to absorbers heavier than Zr (for K-edge XAS). Measurements at lower energies are possible, but require long acquisition times to achieve good signal statistics.

However, by decreasing the inner diameter of the AlN tube, the wall thickness necessary to withstand the pressure during SCW conditions also decreases, thus enabling thinner walls and measurements at lower photon energies. It needs to be kept in mind, though, that the amount of sample in the X-ray beam decreases with decreasing inner diameter. Hence, signal intensity is lowered which might be a problem when investigating very dispersed absorbers such as supported catalysts with low metal loading. In contrast, for samples with a

sufficient concentration of X-ray absorbing atoms, reducing inner diameter and wall thickness would be a viable option to perform XAS at lower photon energies.

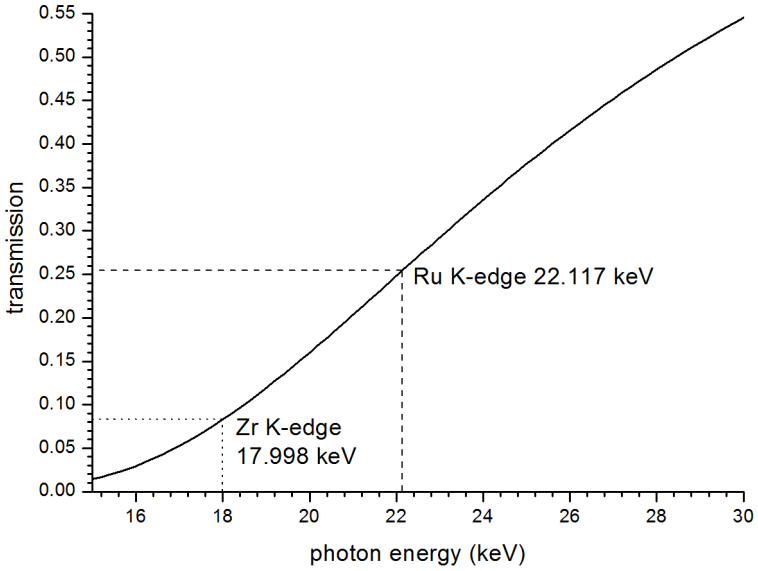

***Figure 4.8**: Calculated X-ray transmission of an AlN capillary with a wall thickness of 1.25 mm (hence, a material thickness of 2.5 mm).*

4.2.4 Construction of the continuous flow, in situ reactor

Figure 4.9 shows a 2D representation of the complete reactor as well as an enlargement of the catalytic zone. As the centerpiece of the X-ray transparent cell, an AlN tube with dimensions 3.5 x 6.0 x 200 mm (CeramTec GmbH, Germany) was used. In order to connect the AlN tube to the high pressure system employed in this study, its ends were glued into stainless steel (316L) casings, using high performance epoxide glue which is stable up to 300°C (Nr. 526N, Kager Industrieprodukte, Germany). To maximize the contact area of the glue, both the steel casings and the AlN tube were sandblasted prior to caulking. The steel casings had a centered bore of 6.3 mm to accommodate the AlN tube; their ends were machined down to 6 mm in diameter with a centered bore of 3.5 mm to allow for connection to Swagelok® fittings.

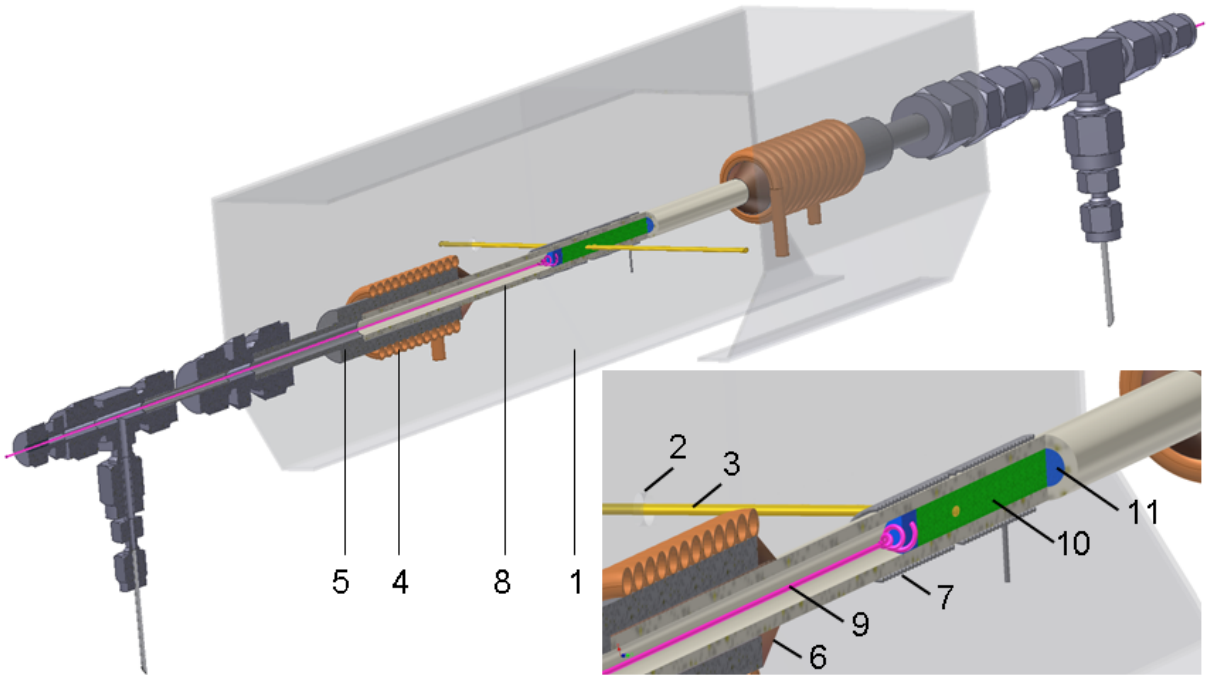

Figure 4.9: *3D model of the in-situ reactor. 1: safety shield, 2: aperture for X-ray beam, 3: X-ray beam, 4: coil of copper tubing, 5: stainless steel casing, 6: epoxide glue, 7: coil of heating wire, 8: AlN tube, 9: thermocouple, 10: catalyst bed, 11: stainless steel frit.*

Due to the high thermal conductivity of AlN and the relatively short reactor tube, the steel casings needed to be water cooled in order to guarantee the mechanical stability of the epoxide glue and to prevent overheating. This was achieved by coils of copper tubing, wrapped around the steel casings. Heat conducting paste (WPS II, TRANSMETRA GmbH, Switzerland) was used to maximize the cooling efficiency.

A flexible heating was realized with a coil of resistive wire, tightly wrapped around the center of the reactor. In this case, an iron-nickel alloy (Monel) was used due to its resistance to oxidation at high temperatures. In order to allow the X-ray beam to pass through the heating unhindered, the twines in the center of the heating coil were pulled apart to a sufficient extent. A remotely controllable AC/DC converter was used to power the heating.

In the following, the assembly of an in situ XAS reactor, based on an AlN tube is described step by step in detail. Figure 4.10 depicts the assembly process at its various steps.

1 Sandblasting of the AlN tube

Both ends of the AlN tube need to be sandblasted thoroughly on a length of 4 cm in order to prepare the surface for optimal contact with the epoxide glue. The air pressure used for sandblasting must not exceed 3 bars, as AlN is prone to fracture at higher pressures.

The inside of the steel casings is sandblasted with an air pressure of at least 6 bars. The 6 mm nipples for the Swagelok® connection need to be protected with tape.

2 Preparation of the epoxide glue

The epoxide glue (Nr. 526N, Kager Industrieprodukte, Germany) is prepared according to the manufacturer's instructions. It should be allowed to cure at room temperature for about 3 hours to reach optimal viscosity before application. The glue has to be free of air bubbles before use.

3 Gluing process

One end of the AlN tube is placed in a steel casing and a steel capillary with a diameter of 3.42 mm is shoved through the 6 mm nipple of the casing and into the AlN tube. This steel capillary prevents the glue from oozing into the AlN tube and the nipple during gluing. Coating the steel capillary with Teflon (using Teflon spray) makes it easier to be removed later on.

The free end of the AlN tube is closed with a rubber cap and a 10 ml syringe is connected to the 6 mm nipple of the steel casing via a plastic tube. This setup is then clamped in a vise in vertical position.

Epoxide glue is spread on top of the steel casing and around the AlN tube so that it completely covers the gap between the AlN tube and the steel casing. While applying

suction via the syringe, the AlN tube is rotated slowly in order to evenly fill the gap between AlN and steel casing with glue. Usually, a second load of glue needs to be deposited on top of the steel casing in order not to suck air into the gap. Suction is applied until the AlN tube can be rotated smoothly without a feeling of friction, a good indicator that the glue has completely filled the gap.

4 Curing

After the gluing process, the whole setup stays in vertical position in the vise for one day. The glue should then be highly viscous and the syringe, rubber cap and steel capillary can be removed. The glue is then further cured at 60°C overnight in an oven and subsequently at 150°C for 3 hours. During curing, the assembly must stay in vertical position. Direct curing at 150°C should be avoided as the glue then becomes liquid again and oozes into the steel nipple.

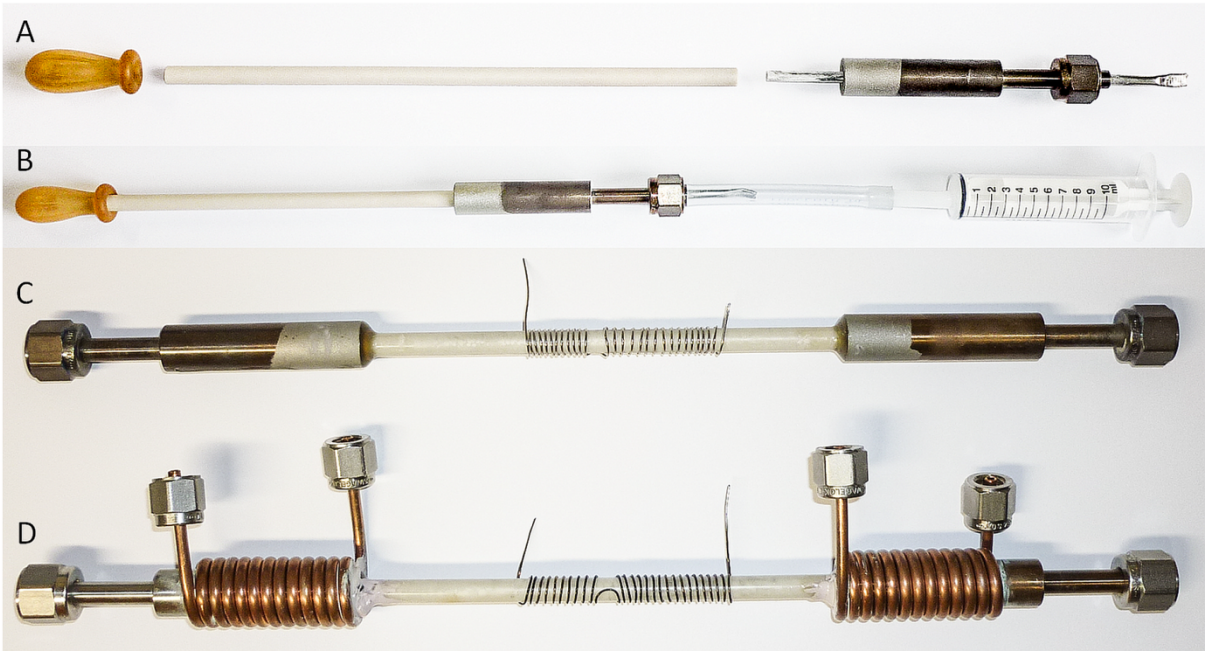

***Figure 4.10**: An AlN reactor at various steps of the assembly process. A: parts necessary for the gluing process. B: assembled and ready for gluing. C: AlN tube with heating coil after gluing into both steel casings. D: fully assembled and ready-for-use AlN reactor with coils of copper tubing for water cooling.*

For operation at the SuperXAS beamline of the Swiss Light Source, the in situ reactor was supported on an aluminum rack and encased in a safety shield made of 3 mm aluminum. Small openings in the safety shield at the level of the reactor tube allowed the X-ray beam to pass through unhindered.

4.3 Results and discussion

4.3.1 Operation of the in situ reactor

The in situ reactor was integrated into the high pressure, liquid flow setup described in chapter 3.2.1. Before operation at the beamline, the reactor was pressure tested to 30 MPa at room temperature for 3 hours in our high pressure lab. The in situ reactor was then used in a study of catalytic biomass gasification and operated almost continuously at 24.5 MPa and 400°C for 5 days. During that time, no material failure occurred, nor could any degradation of the reactor material be observed. An electrical power of 120 W was sufficient to heat the catalytic zone of the reactor to 400°C at a rate of 4 K/s (measured inside the reactor) whilst a solution of 7.5 wt% EtOH in water was fed at a flow rate of 0.5 ml/min.

As AlN has a high temperature shock stability, experiments involving fast heating-cooling cycles are not expected to present a problem.

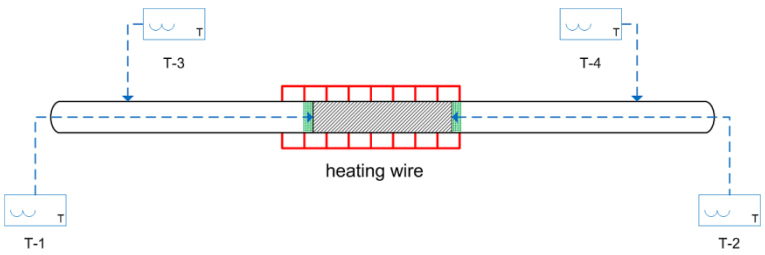

***Figure 4.11**: Sketch of the AlN reactor with installed thermocouples. T-1 and T-2 record the temperature in front of and behind the catalyst bed, respectively. T-3 and T-4 record the temperature at the transition point between the bare AlN capillary and the encased (glued) parts. The catalyst bed (shaded grey) is held in place by two stainless steel frits (pore size 5 µm, green). Direction of flow is from left to right.*

Due to the thermal heat conductivity of AlN, overheating and mechanical failure of the epoxide glue were a concern. However, the water cooling was efficient enough to keep the temperature of the steel casings well below 100°C. Temperatures measured at the transition point between the bare and encased parts of the AlN tube (thermocouples T-3 and T-4 in Figure 4.11) never exceeded 180°C.

4.3.2 Considerations on Safety

The results of Boukis et al. show that the surface of AlN is slowly attacked under hydrothermal conditions with a mass change of 4.8 mg/cm^2 after 80 hrs.[101] However, a very corrosive supercritical medium, containing hydrogen peroxide and hydrochloric acid, was used in their study. The results of that study further suggest that there is no single ceramic material which is generally stable under hydrothermal conditions. The composition of the supercritical medium (e.g. acidic vs. basic, ionic species) has a significant influence on the corrosion rate and needs to be taken into account when evaluating the reactor lifetime. Generally, long term operation using strongly corrosive fluids (acidic and/or oxidative) should be avoided whilst strongly caustic fluids should not be used altogether as they are known to hydrolyse AlN.[106] It is suggested to regularly inspect the inside of the in situ reactor and to install a fresh AlN tube after about 80 hours of online operation.

$$p = \frac{20w\frac{K}{s}}{D - w} \tag{4.1}$$

Equation 4.1*: Calculation of the pressure stability of a ceramic tube. p: pressure in MPa, w: wall thickness, K: tensile strength of the ceramic material in MPa, s: safety factor (≥ 1), D: outer diameter.*[107]

The reactor should be enclosed in a safety shield at all times during operation, since structural failure of the AlN tube under hydrothermal conditions will lead to a steam

explosion and the generation of ceramic shrapnel. Based on the mechanical properties of sintered AlN and equation 4.1, the in situ reactor presented here has a calculated rupture pressure of 79 MPa, applying a safety factor of 2.[106,107] The reactor was pressure-tested at 30 MPa and 450°C for two hours during which no leakage or structural failure occurred.

4.3.3 In situ EXAFS of a carbon supported Ru catalyst during SCWG of ethanol

EXAFS measurements under SCW conditions were carried out in transmission mode at the Ru K-edge at the SuperXAS beamline of the Swiss Light Source (SLS), Villigen, Switzerland. The SLS is a third generation light source with a storage ring energy of 2.4 GeV, a current of 400 mA and top-up injection.

The beam was monochromatized with a Si (311) double crystal monochromator and was focused on the sample to a size of 3000 by 500 micron. The monochromator was operated in "on-the-fly" mode, which allowed for collection of a full EXAFS spectrum (1200 eV scan) in 180 seconds. The incident and transmitted intensities were monitored by ion chambers filled with Ar.

specific surface area (BET)	~ 1100 m^2/g
active metal surface area[23]	3.11 m^2/g
average Ru particle size	1.5 nm
dispersion[23]	32%
bulk density	0.5 g/cm^3

***Table 4.1**: Properties of the 2 wt% Ru/C catalyst (BASF, Italy).*

The performance of the in situ reactor under SCW conditions was evaluated by studying the Ru catalyzed gasification of ethanol in supercritical water. A commercial catalyst, consisting of 2 wt% Ru supported on highly porous coconut carbon was used (BASF, Italy). The as-

received catalyst was crushed and sieved to a grain size of 125 to 800 µm. Table 4.1 summarizes the key properties of this catalyst.

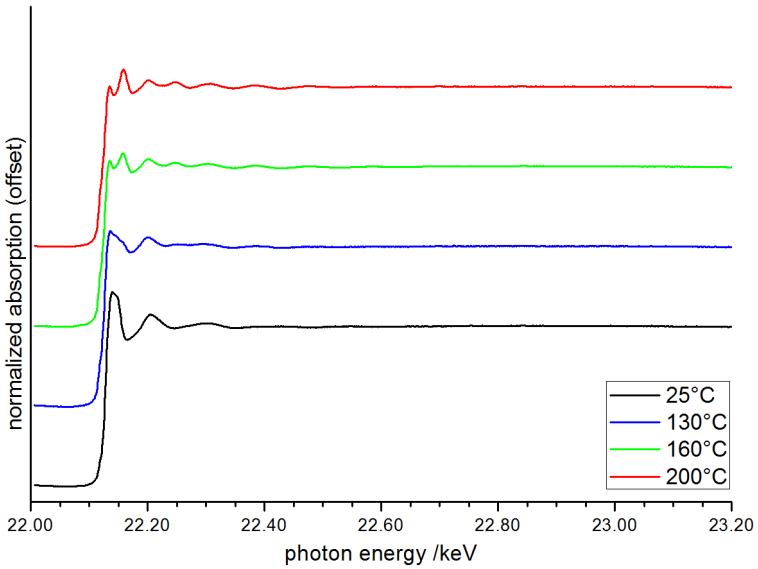

Figure 4.12: *Normalized Ru K-edge EXAFS spectra of fresh 2% Ru/C in a continuous flow of 7.5 wt% ethanol in H_2O at various temperatures (experiment Ci-1). All spectra were recorded at 24.5 MPa with an acquisition time of 180 sec.*

The reactor was loaded with 150 mg of Ru/C, fixed between two stainless steel frits (pore size 5 µm). The setup was brought to an operating pressure of 24.5 MPa at room temperature by pumping deionized water at a flow rate of 0.5 ml/min. The feed was then switched to 7.5 wt% ethanol in water whilst keeping the flow rate constant. Under these conditions the catalyst was present in its fully oxidized form RuO_2, as confirmed by EXAFS. Stepwise heating up to supercritical conditions showed that reduction of the RuO_2 particles to Ru^0 started at 130°C and was complete at 200°C (Figure 4.12). The catalyst then remained in its reduced form which represents the active phase during SCWG of ethanol at 400°C, confirming previous results.[46] To the best of our knowledge, these are the first full EXAFS spectra of a supported catalyst recorded under SCW and continuous flow conditions.

At supercritical conditions (400°C, 24.5 MPa), damping of the EXAFS signal due to the high temperature is visible (Figure 4.13). However, data quality remained high up to k = 12 $Å^{-1}$, allowing for analysis of Ru particle structure and size during hydrothermal ethanol gasification which is reported in chapter 6.

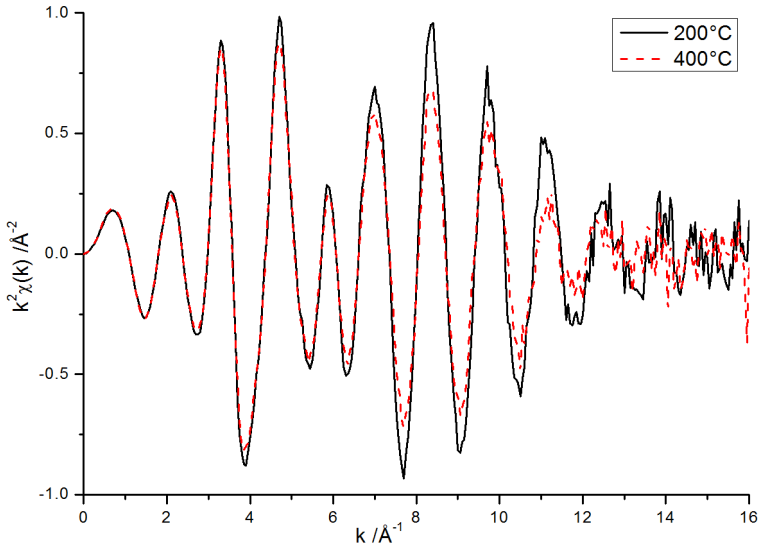

Figure 4.13: *EXAFS spectra of the active 2% Ru/C catalyst in sub- (200°C) and supercritical (400°C) water at 24.5 MPa (acquisition time: 180 sec). Damping of the EXAFS signal is well visible at 400°C.*

4.4 Conclusions

A novel, continuous flow reactor was constructed that is able to withstand the demanding conditions of supercritical water (p > 22.1 MPa, T > 374°C) and is resistant to chemical attack by the supercritical medium. This was achieved by employing aluminum nitride as reactor material, an inexpensive, nontoxic and highly stable ceramic.

For the first time, in situ EXAFS spectra of a supported metal catalyst in supercritical water were recorded, allowing for analysis of the catalyst's local structure and electronic state under these reaction conditions.

The presented continuous flow reactor may be used for investigating a plethora of catalytic as well as non-catalytic chemical reactions in gaseous, liquid and supercritical media. Its application is not limited to the field of XAS but also offers a viable option for in situ XRD under high T and p conditions.

Chapter 5

Evidence of scrambling over ruthenium-based catalysts in supercritical-water gasification

Abstract

Catalytic processes that employ Ru catalysts in supercritical water have been shown to be capable of converting organics into synthetic natural gas (CH_4) with high efficiencies at relatively moderate temperatures of around 400°C. However, the exact role of the catalyst and the descriptors that would enable the search for better catalysts with high conversions and selectivities have not been determined. This chapter outlines how electronic structure calculations are coupled with batch experiments to study the interaction of methane (CH_4) and water (H_2O) with a commercial catalyst, carbon supported ruthenium (Ru/C), to understand the final steps of the methanation reaction. The calculations predict that when CH_4 and H_2O react with the Ru surface, these molecules will undergo rapid scrambling, interchanging most of the hydrogen atoms with the Ru surface before desorbing as CH_4 and H_2O once again. Experiments using CH_4 as a feedstock in supercritical D_2O (deuterated water) in the presence of a carbon-supported Ru catalyst were conducted to confirm this mechanism: nearly all converted CH_4 formed fully substituted CD_4 or the 3/4-substituted CHD_3 isotopomers, with less significant production of the 1/4- or 1/2-substituted species CH_3D and CH_2D_2. The experiment was repeated with a RuO_2 powder catalyst, with similar results. Although other criteria such as the ability to cleave C-C and C-O bonds and resistance to poisoning will also prove important, this study suggests that one characteristic of an effective catalyst for supercritical water gasification to methane is its ability to promote rapid equilibria through scrambling mechanisms.

The contents of this chapter were published as *A. Peterson, M. Dreher, J. Wambach, M. Nachtegaal, S. Dahl, J. Nørskov and F. Vogel, CHEMCATCHEM 4 (2012), 1185*.[108]

Density functional theory (DFT) calculations and the discussion thereof were performed by Andrew Peterson at Stanford University, Stanford, USA; experimental data from batch gasification experiments and the discussion thereof was provided by Marian Dreher, in the frame of the presented thesis at Paul Scherrer Institute, Villigen, Switzerland.

5.1 Introduction

Since X-ray studies by Rabe et al indicated that metallic ruthenium (rather than the oxide) is the active catalytic phase during supercritical-water gasification[46], a different mechanism than the Ru oxidation state cycling proposed by Park and Tomiyasu (see chapter 1.3) must be responsible for the gasification.[43] The work presented in this chapter attempts to provide the basis for a mechanistic understanding by using electronic structure calculations to model the elementary dehydrogenation steps of C_1 and O_1 compounds on a reduced Ru^0 surface, and couple this with batch experiments in supercritical D_2O to validate the mechanistic insights from DFT. This will provide an understanding of the interaction of CH_4 and H_2O with the surface, and provides insight into the final steps of the methanation reaction. The role of scrambling in supercritical-water gasification is highlighted, defined here as the rapid and facile interchange of hydrogen atoms from adsorbates to the catalyst's surface.

5.2 Experimental part

The electronic structure calculations, conducted by A. Peterson, are described in detail in the publication that is the basis of this chapter and will only be briefly described here.[108] Calculations were undertaken on 3×3×3 (atoms) supercells of Ru, taken to be in an fcc (211)

configuration to allow for both step and terrace binding sites on the same structure. Adsorbates on the Ru surface were optimized starting from various initial geometrical configurations and the lowest-energy conformer is reported. To calculate the chemical potential of supercritical water, the chemical potential of liquid water at standard temperature and pressure (STP) was calculated first; thermodynamic values from the International Association of Water and Steam (IAPWS) were then employed to calculate the difference between water at STP and water at supercritical conditions of 669 K and 22.5 MPa. At supercritical water conditions, the hydrogen-bonding strength of water diminishes, and adsorbates were assumed not to be stabilized by the presence of water.[109–113]

Batch SCW gasification experiments were performed in an unstirred tubular stainless steel batch reactor with an internal volume of 55 ml (High Pressure Equipment Company, USA). The temperature inside the reactor was measured by a thermocouple at half the length of the reactor tube. Two catalyst preparations were used. The first was the commercially available 2 wt% Ru/C catalyst, described in chapter 4. Another Ru catalyst was prepared in-house by impregnating 1040 mg of granular coconut carbon with a suspension of 150 mg of RuO_2 (99.9%, Sigma Aldrich) in 0.5 ml of water. This preparation was then dried in vacuum at 60°C and is hereafter referred to as “Catalyst X”. 1040 mg of catalyst, confined in stainless steel mesh, was placed on top of the thermocouple. In the catalyst-free experiments only the steel mesh was used. The reactor was then loaded with 8.5 ml of D_2O (99.8% D, ARMAR Chemicals, Switzerland) and pressurized with 4.0 MPa of methane (purity 4.5, CarbaGas, Switzerland), resulting in a molar D to H ratio of approximately 3.24. The batch reactor was immersed in a fluidized sand bath, set to 400°C, and reached a constant reaction temperature of 395±1°C after 6 min. Owing to the initial pressure of 4 MPa, the D_2O stayed liquid until it reached the critical point and thus only made contact with the catalyst in the supercritical state. After a reaction time of 24 hours, during which the pressure inside the reactor stabilized at 28.5 MPa, the reaction was quickly quenched by immersing the reactor in water. After cooling down to room temperature and passing through a cold trap at -60°C to remove moisture, the product gases were released into a gas sampling bag.

Analysis of the gas components was performed by using a mass spectrometer (Quadstar 32, Pfeiffer, Germany). Total gas composition was calculated by calibrating the MS with standardized gas mixtures. The relative amounts of CH_xD_{4-x} isotopomers in the product gas

were calculated using their fragmentation patterns according to Schissler et al and the raw ion intensities of masses 16 (CH_4) through 20 (CD_4).[114] Contributions to the mass 16 via fragmentation of CO and CO_2 were subtracted before the determination of methane composition.

5.3 Results and discussion

To better understand the mechanism by which a pure metallic (reduced) ruthenium catalyst can catalyze the production of methane, density functional theory (DFT) calculations on CH_x and OH_x adsorbates, related to methane formation on ruthenium, were conducted. Figure 5.1 shows the results for the dehydrogenation of CH_4 on a stepped ruthenium surface; these results are similar to those appearing previously in the context of steam reforming of methane.[115] The results suggest that there is a significant penalty to perform the initial dehydrogenation of methane

$$CH_4 + 2* \rightarrow CH_3* + H*. \quad (5.1)$$

The free-energy barrier for this initial dehydrogenation is on the order of 1.6 eV, which at 400°C corresponds to a slow but appreciable reaction, typically on the order of 1-10 s^{-1} $site^{-1}$; in other words, this barrier is just surmountable at reaction conditions. However, after this initial dehydrogenation, the subsequent dehydrogenation reactions

$$CH_3* + * \rightarrow CH_2* + H* \quad (5.2)$$

and

$$CH_2* + * \rightarrow CH* + H* \quad (5.3)$$

are quite easily surmountable, with barriers for each of these subsequent dehydrogenation reactions much smaller than the reverse reaction of CH_3* to CH_4. From CH*, the final dehydrogenation

$$CH^* + * \rightarrow C^* + H^* \quad (5.4)$$

has a larger barrier than the previous two, and it is on the same order as the barrier to desorb CH_3* as CH_4. This implies that any CH_x* species present on the catalyst surface will readily scramble among the partially dehydrogenated states, CH* to CH_3*, before desorbing. Additionally, a significant proportion of the adsorbed CH_x* species is expected to surmount the 1.10 eV barrier from CH* to C*. This is consistent with a scrambling mechanism.

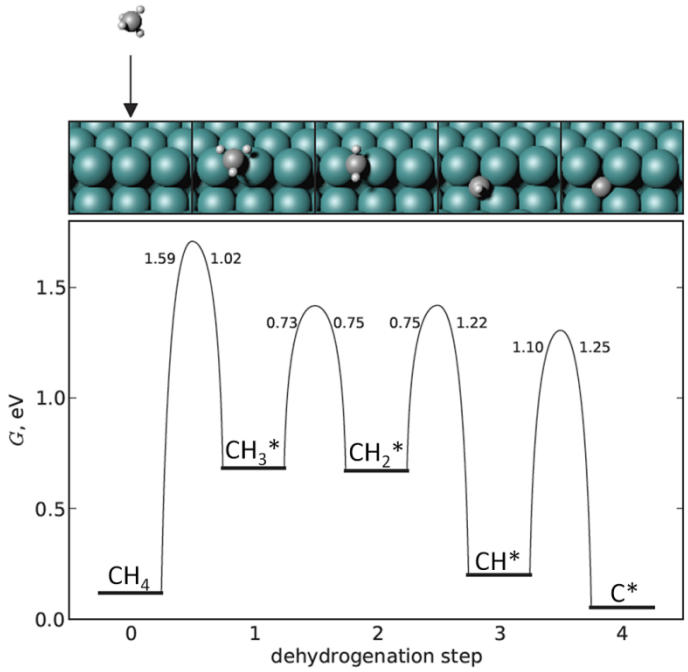

***Figure 5.1**: Calculated free energy pathway for the dehydrogenation of methane over a stepped ruthenium surface. The horizontal lines represent the energies of the metastable intermediates, the transition-state barriers are shown as Bezier curves between the intermediates. The calculated barrier height of the forward and reverse reaction is shown next to each barrier. The atomic figures at the top show the optimized binding geometry of each intermediate; dissociated hydrogen atoms are not pictured. Adapted from Peterson et al.*[108]

A similar analysis can be made for the interaction between H_2O and the Ru surface. A free-energy diagram of the dehydrogenation reactions of H_2O is shown in Figure 5.2. Based on these calculations, the initial dehydrogenation of water on the surface as OH* + H* will be much more facile than for methane, with a calculated forward barrier of 0.80 eV. The reverse reaction is more difficult, with a barrier of 1.44 eV; again, it is more facile to dehydrogenate the OH* into O* + H*, with a calculated barrier of about 1.1 eV. This implies that the water will readily interact with the Ru surface, leading to the interchange of a large

amount of adsorbed hydrogen with the surface. The high barrier to dissociative adsorption of CH_4, followed by smaller barriers for subsequent dehydrogenation of adsorbed species is consistent with a scrambling mechanism for methane. It implies that the Ru catalyst strips the hydrogenated carbon (CH_4) and hydrogenated oxygen (H_2O) via a scrambling mechanism over the metallic Ru catalyst.

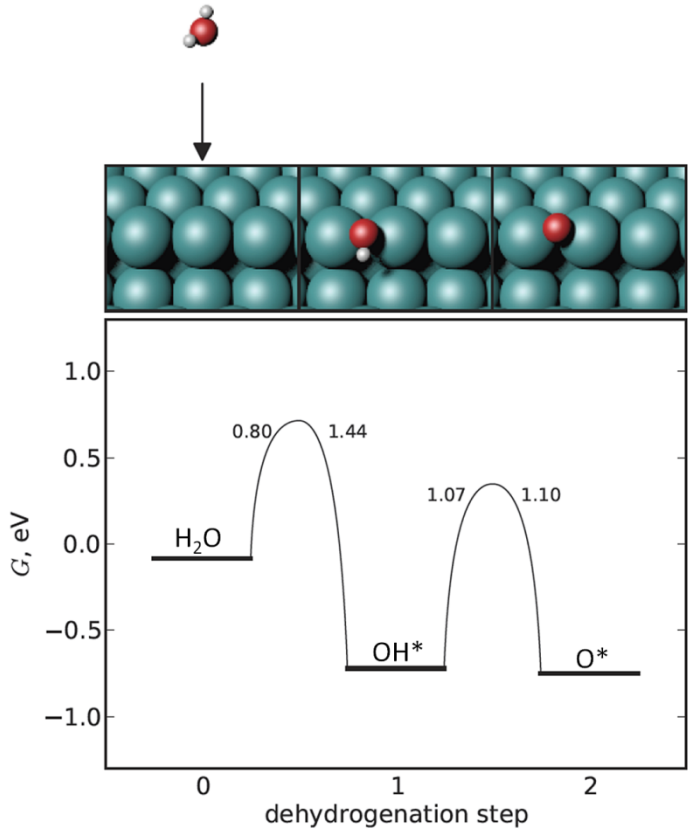

***Figure 5.2**: Calculated free energy pathway for the dehydrogenation of water over a stepped ruthenium surface. The horizontal lines represent the energies of the metastable intermediates, the transition-state barriers are shown as Bezier curves between the intermediates. The calculated barrier height of the forward and reverse reaction is shown next to each barrier. The atomic figures at the top show the optimized binding geometry of each intermediate; dissociated hydrogen atoms are not pictured. Adapted from Peterson et al.*[108]

To understand the relevance of these calculations to operation of the supercritical-water reactions, experiments using CH_4 as a reactant (which is normally the product of gasification) in supercritical heavy water, D_2O, were performed. If the suggested scrambling mechanism indeed takes place, it would be expected that D_2O readily dehydrogenates on and interchanges hydrogen atoms with the ruthenium surface, supplying a large amount of adsorbed D to surface reactions. CH_4 will react with the surface at a relatively lower rate, but any CH_4 that reacts with the surface will be expected to readily scramble with the hydrogen

(mainly D) atoms on the surface before desorbing again as methane. This should result in methane that has been fully or 3/4-substituted into the products CD_4 and CHD_3, since the last dehydrogenation barrier is the only one comparable to the desorption barrier. Twenty four hours batch experiments with CH_4 in supercritical D_2O, with and without Ru catalysts, were performed as described in section 5.2. The resulting product gases were analyzed with mass spectrometry (MS) in order to quantify the isotopomers formed.

The MS results are shown in Figure 5.3. Without the presence of a catalyst, CH_4 is largely unreactive, with only a small amount being converted to CO and CH_3D. In the presence of the Ru/C catalyst, methane was much more reactive, with only about 67 % of the original amount of methane detectable as CH_4 after the reaction. The fraction of the methane that did react was mostly detected as the isotopomers CH_xD_{4-x}. Consistent with the predictions of the DFT calculations, the large majority of the isotopomers were the fully substituted CD_4, at roughly 16 %, and the 3/4-substituted CHD_3, at about 10 %. This strongly supports the scrambling mechanism suggested in Figure 5.1.

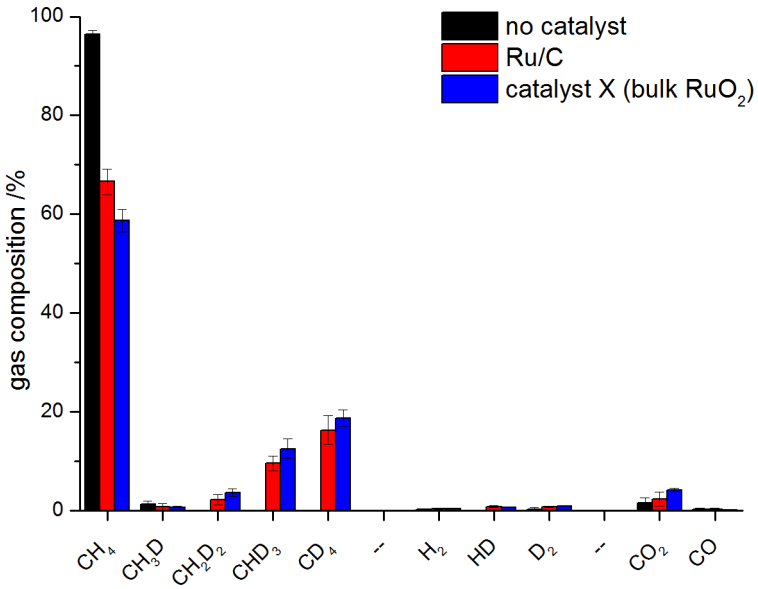

***Figure 5.3**: Gas-phase composition for catalyst-free conditions ("no catalyst", black), with a commercial carbon supported ruthenium catalyst ("Ru/C", red), and with an in-house synthesized RuO_2-on-carbon catalyst ("Catalyst X", blue); (experiments B-1 to B-3).*

Catalysts can also be synthesized from RuO_2 powder impregnated onto carbon. As shown by Rabe et al. and discussed in chapter 6, spectroscopic in situ data has shown that these catalysts are reduced to the pure metallic Ru during hydrothermal operation.[46] To test if a similar behavior occurs in this system, an identical twenty four hours batch experiment with an RuO_2 on carbon catalyst, as described in the methods and referred to as Catalyst X, was performed (Figure 5.3). A similar amount of CH_4 was transformed as in the case of the commercial Ru/C catalyst, with about 59% of the gas-phase products observed to be the fully unsubstituted CH_4. Similarly, the trend holds for the fractions of methane isotopomers; the fully substituted CD_4 was the most prevalent form of transformed methane at about 19%, followed by the 3/4-substituted CHD_3, at about 13%. Although initial structural differences exist between the two catalyst preparations, the relative amounts of CD_4 to CHD_3 were within statistical uncertainties of one another.

5.4 Conclusions

This study provides insight into how supercritical-water gasification (SCWG) catalysts act to use surface "scrambling" reactions to promote the production of an equilibrium gas composition, and suggests that molecular adsorbates are often broken down into atomic adsorbates by the catalyst surface before reforming into the equilibrium amounts of desorbed species.

Scrambling, defined here as the rapid and facile interchange of hydrogen atoms from adsorbates to the catalyst surface, has been shown to occur on Ru catalysts under supercritical water gasification conditions, through both theoretical calculations and isotope-labeling experiments. The agreement between calculation and experiment provides further indication that the pure metallic form of Ru, rather than an oxide form, is the active catalyst surface for the supercritical-water reforming and methanation reactions. This study further suggests that there will likely be high equilibrium coverage of OH and H on the catalyst surface. The relatively simple analysis presented here captures the major effects in terms of scrambling efficiency on a metallic Ru catalyst. This provides a basis for understanding the mechanism of the methanation reaction, and suggests an alternative mechanism to the Ru

oxidation-cycling mechanism that involved syngas as an intermediate, which was proposed elsewhere in the literature.

This is in agreement with an earlier study that shows that the gas composition resulting from SCWG is very close to the thermodynamic equilibrium gas composition, as predicted with the Peng-Robinson equation of state.[116] Although other considerations will be important, such as the ability to break up large molecules by breaking C-C and C-O bonds, coverage effects, and resistance to poisoning, this study suggests that a key role of the catalyst in SCWG is to support the facile interchange of hydrogen atoms between adsorbates and the catalyst surface.

Chapter 6

Pathway of the methanation reaction and sulfur poisoning over a Ru/C catalyst during the reforming of bio-molecules

Abstract

In the development of new processes that provide “green energy”, supercritical water has emerged as a powerful reaction medium to convert biomass into combustible gases such as hydrogen or methane. Due to typical SCW catalytic process conditions (400°C, 25 MPa), in situ characterization of materials and catalysts used in selective biomass conversion is difficult and accordingly, there is limited knowledge about catalyst structure and reaction pathways under these conditions. Particularly, catalyst poisoning mechanisms by sulfur, a major obstacle in catalytic biomass conversion, need to be understood in order to design sulfur resistant catalysts or catalyst regeneration procedures. We followed the dynamic structural changes of a Ru catalyst during the conversion of biomass model compounds (methanol and ethanol) to methane in supercritical water in a continuous flow reactor. In situ X-ray absorption spectroscopy showed that the catalyst is being activated by the organic compounds at low temperature without a detectable change in particle size during eight hours of operation. Combining XAS with isotope labeling and electronic structure calculations, we demonstrated that sulfur poisoning proceeds via irreversible adsorption of S^{2-} with a surface coverage of about 40% instead of bulk sulfidation. The adsorption of sulfur significantly changes the nature and abundance of hydrocarbon adsorbates – the precursors for methane formation – on the catalyst’s surface. This affects both the activity and selectivity of the catalyst for the methanation reaction. These results provide an incentive for designing sulfur resistant catalysts or effective regeneration procedures.

The content of this chapter was published as *M. Dreher, B. Johnson, A. Peterson, M. Nachtegaal, J. Wambach and F. Vogel, Journal of Catalysis 301 (2013), 38-45*.[117]

Density functional theory (DFT) calculations were performed by Benjamin Johnson and Andrew Peterson at Brown University, Providence, USA.

6.1 Introduction

The issue of sulfur poisoning during the supercritical water gasification (SCWG) of biomass has been addressed by several studies that can be found in literature and was outlined in chapter 1. Most of these studies, however, have been conducted using batch reactors instead of continuous flow reactors which would represent realistic process conditions more closely, combined with analysis of product gas composition and ex situ samples of the spent or poisoned catalysts.[50–52] Osada et al. studied the influence of sulfur on the Ru catalyzed gasification of lignin and found sulfur in several oxidation states on the spent catalysts.[52] However, the catalyst samples were prepared in a humid and aerobic environment and could thus have suffered from oxidation. Sulfur poisoning of a Ru/C catalyst during the continuous gasification of ethanol and synthetic liquefied wood was studied by Waldner et al. who showed that sulfur concentrations as low as 16 ppm are sufficient to poison the catalyst.[50] They suggested the formation of a ruthenium sulfate phase as the cause for catalyst deactivation but concluded that in situ studies are necessary to clarify the mechanism of catalyst deactivation. At present, the results published in the literature suggest that sulfur poisoning decreases the catalyst's ability to break C-C bonds and to perform methanation by blocking the respective active sites on the catalyst's surface.[51] However, there is no structural spectroscopic in situ data on the catalytic reforming of organics in supercritical water and particularly on the effect that sulfur poisoning has on the catalyst. As a consequence, there is no knowledge of the mechanism of sulfur poisoning and of the structure of the poisoned catalyst under these reaction conditions which is of fundamental importance for the development of sulfur resistant catalysts and regeneration protocols.

In chapter 4, the first in situ EXAFS data of the Ru/C catalyst in SCW was presented. In this chapter, the study is extended to include the activation and sulfur poisoning of the same carbon-supported ruthenium catalyst, used for biomass reforming in SCW, with in situ XAS in a realistic, continuous flow process. The spectroscopic data is combined with results from isotope labeling and electronic structure calculations in order to interpret the experimental results with a particular focus on the mechanism of the methanation reaction for both the active and sulfur poisoned catalyst. As simple biomass model substances, methanol and ethanol were used since their reforming requires breaking of C-O and C-C bonds, both steps being imperative in the reforming of real biomass.

6.2 Experimental part

6.2.1 Experimental setup

The design of the high pressure/high temperature liquid flow setup and the continuous flow reactor used for acquiring in situ extended X-ray absorption fine structure (EXAFS) and X-ray absorption near edge structure (XANES) spectra under SCW conditions has been illustrated in detail in chapter 4. For batch experiments, an unstirred tubular stainless steel batch reactor with an internal volume of 54 ml (High Pressure Equipment Company, USA) was used. The temperature inside the reactor was measured by a thermocouple at half the length of the reactor tube.

In all experiments described here, the commercial Ru catalyst (see chapter 4) was used. All chemicals were of analytical grade (≥99.5%) and obtained from Sigma Aldrich, unless otherwise noted. For experiments using the continuous flow reactor, the as-received Ru/C catalyst was crushed in a mortar and sieved to a grain size range of 50 to 200 μm. Typically, 200 mg of Ru/C were used in these experiments as a fixed bed. In experiments using the tubular batch reactor, 1050 mg of Ru/C, confined in stainless steel mesh, were used in its as-received state, hence with a grain size of about 3 mm. For batch gasification over sulfur poisoned Ru/C, 1050 mg of as received Ru/C were deactivated prior to the gasification

experiments by exposing it to 50 µl of dimethyl sulfoxide (DMSO) in 10 ml of water for 30 min at 395°C and 30 MPa. For the deuterium labeling experiments performed in batch reactors, 9 ml of a methanol in D_2O (99.8% D, ARMAR Chemicals, Switzerland) solution with the desired D/H ratio were used. For ^{13}C labeling, a solution of 0.5 g of 1-^{13}C ethanol (99% ^{13}C) or 1-^{13}C acetic acid (99% ^{13}C) in 9.5 ml H_2O was used. The ^{13}C labeled compounds were obtained from Cambridge Isotope Laboratories, USA. To limit evaporation during heat-up, a pre-pressurization with 4 MPa of argon was applied. The reactors were heated up to 398°C within 6 min in a fluidized sand bath and kept at this temperature for 5 to 25 min, after which the reactors were quickly cooled down to room temperature in a water bath. The product gases were extracted in a gas bag and analyzed with an MS (OmniStar, Pfeiffer Germany) in the case of deuterium labeling and with a GC-MS (SRA Instruments and Agilent Tech. 5975C) in the case of ^{13}C labeling.

For continuous flow gasification experiments, a feed of 7.5 wt% of ethanol in normal (H_2O) or deuterated (D_2O) water was used. The feed used to poison the catalyst additionally contained 200 ppm of DMSO, corresponding to 81 ppm of sulfur. Although a sulfur concentration of 16 ppm was reported to be sufficient for complete sulfur poisoning of the Ru/C catalyst, the concentration of 200 ppm DMSO (81 ppm S) was chosen in order to poison the catalyst within a reasonably short time since experiments at the XAS beamline and the use of D_2O as a solvent demanded time and cost efficient planning.[50] DMSO was chosen as an organic sulfur source due to its miscibility with water.

In order to determine the composition of deuterated methane, produced by gasification in heavy water, the MS signals were deconvoluted according to Schissler et al.[114]

XAS measurements were conducted at the Swiss Light Source (SLS) in Villigen, Switzerland. In situ XANES and EXAFS at the Ru K-edge (22.117 keV) were measured at the SuperXAS beamline of the SLS, with an acquisition time of 180 s per spectrum. Sulfur K-edge (2470 eV) and Ru L_3-edge (2840 eV) fluorescence spectra of ex situ samples were taken at the PHOENIX beamline of the SLS.

6.2.2 XAS data treatment

Treatment of the XAS data was performed using the IFEFFIT software package.[80,82] All XAS spectra were energy-calibrated by measuring a Ru reference foil (EXAFS Materials, USA) simultaneously with the samples. Linear combination fitting (LCF) of XANES spectra taken during catalyst activation was carried out in the energy range of -30 to 50 eV with respect to the absorption edge, using reference spectra obtained from a Ru foil and pelletized RuO_2. A weighting factor, allowed to range from 0 to 1, was assigned to each reference spectrum whereas the sum of weights was normalized to unity.

Fourier transformation of the normalized and background subtracted EXAFS spectra was carried out over a k-range ranging from 3.5 to 12.5 $Å^{-1}$ and a window function with $\Delta k = 1$. Fitting of the EXAFS data was then realized using scattering paths obtained from theoretical standards for metallic Ru and RuS_2, respectively.[118,119] In the case of the active catalyst the following fitting strategy was used: the main Ru-Ru coordination shell (CS) was fitted first, in an R-range from 1.5 to 3 Å, without constraining the fitting parameters (s_0^2, E_0, Δr, σ^2). Then, E_0 and Δr were fixed at their best fit values and the fit range was extended to 4 Å. The scattering path of the second Ru-Ru CS was added to the fit with its own set of s_0^2 and Δr parameters. Fitting of the first two Ru-Ru CS thus provided a single energy shift E_0 and pseudo Debye-Waller factor σ^2, valid for both shells, as well as amplitude reduction factors (s_0^2) and bond distance shifts (Δr) for each shell. The amplitude reduction factors were calibrated against data from bulk samples of metallic Ru (first and second shell Ru-Ru coordination numbers fixed at 12 and 6, respectively) to obtain the coordination number (CN) for each shell. The same strategy was used for the S-poisoned catalyst in order to determine the CN of the first and second Ru-Ru CS. Then, E_0, Δr and σ^2 of the Ru-Ru shells were fixed at their best fit values and the Ru-S CS was fitted with its own set of fitting parameters. Again, data from a bulk sample of RuS_2 was used to calibrate the s_0^2 parameter (Ru-S CN fixed at 6). All fitted spectra and experimental data were plotted using the first Ru-Ru scattering path for phase correction.

6.2.3 Computational details

Electronic structure calculations were carried out using Dacapo, a density functional theory (DFT) code operated within the Atomic Simulation Environment (ASE).[120,121] Calculations involving adsorbates used a 3 × 3 × 3 atom supercell of Ru in an fcc (211) configuration, as in a previous study.[108] The lattice constant of the Ru cell was optimized using DFT. Periodic boundary conditions were utilized in all three dimensions, forming a continuous slab in the *x*- and *y*- directions and approximately 15 Å distance of vacuum between adjacent layers in the *z*- direction. In all calculations, the bottom two layers of the slab were kept fixed at their bulk lattice positions and the top layer of Ru (in contact with the adsorbates) was allowed to relax in geometry optimizations. The RPBE exchange-correlation functional was utilized.[122] A 4 × 4 × 1 grid was used for *k*-point sampling. A Fermi smearing of 0.1 eV was utilized, and a dipole correction was enforced. For desorbed species (CH_4 and H_2), calculations were undertaken in a 15.0 × 15.0 × 15.0 Å cell with γ-point sampling and a Fermi smearing of 0.01 eV.

For each adsorbate and surface investigated, the adsorbate was placed in multiple starting configurations corresponding to all the probable sites to which the adsorbate could bind. Each system was then optimized using the BFGS line search algorithm to a maximum force of 0.05 eV/Å. The lowest energy conformer for each adsorbate-surface system is reported. From the obtained internal energy value, the free energy was derived using the vibrational modes of adsorbed atoms in a harmonic approximation. The geometries of the gas-phase (desorbed) molecules were also optimized in the BFGS line search algorithm, and electronic energies were converted to free energies using standard statistical mechanics treatments for ideal gases.[123]

In addition to the bare Ru surface described above, surfaces “poisoned” with 1, 2 and 3 sulfur atoms were also examined, corresponding to 1/9, 2/9 and 1/3 monolayer (ML) coverage, respectively. For 1/9 ML coverage, a single S atom was placed in multiple starting locations on a bare Ru surface and optimized, identical to the process described previously for other adsorbates. The lowest energy outcome was found to be in a fourfold (fcc 100) site directly below the step; this surface was employed in further analyses involving additional (CH_x and H) adsorbates on the 1/9 ML surface. The process was repeated to obtain the 2/9

and 1/3 ML coverage surfaces. For the 2/9 ML surface, the optimum surface featured the second S atom in a threefold site above the step. However, further analysis was conducted using a surface with the second S atom in an adjacent fourfold site. The energy of this configuration was within 0.05 eV of the optimum, within the margin of error for DFT calculations, and allowed for a more consistent analysis. Preliminary investigations using the optimum surface reveal that its adsorption behavior is comparable to that of the utilized surface and that in some cases the optimum surface may be less energetically favorable to further adsorptions compared to the sub-optimal surface used. The 1/3 ML coverage surface featured two S atoms in fourfold sites and one S atom in a threefold site. In the calculations treating sulfur-poisoned Ru clusters, the free energy was calculated by performing a normal-mode analysis on all of the adsorbates present, including the sulfur atoms.

6.3 Results and discussion

6.3.1 Catalyst activation

To establish the structure and particle size of an active Ru/C catalyst under process conditions, the catalst activation was monitored by in situ XAS. Figure 6.1 shows the EXAFS and XANES spectra during the stepwise heat-up of a fresh Ru/C catalyst in a stream of 7.5% ethanol in water, recorded at the Ru K-edge. At room temperature, the ruthenium is present in the form of pure RuO_2, represented by a full Ru-O coordination shell at 1.95 Å and the complete absence of metallic Ru-Ru bonds at 2.7 Å. The XANES spectrum shows an absorption edge at 22.129 keV and a single, broad absorption peak at 22.143 keV which are both indicative of RuO_2.

The structure of the RuO_2 particles remains stable up to about 125°C, at which point it suddenly collapses. The lack of any prominent coordination shells in the EXAFS at 125°C suggests a disordered state of the catalyst particles. In the XANES plot, a shift of the absorption edge to lower energies is clearly visible, indicating a reduction of the RuO_2 particles. At this point, the catalyst is composed of both oxidized and metallic Ru species.

Consecutively, the particles are reduced to metallic ruthenium as indicated by a shift of the absorption edge to about 22.117 keV and the formation of a double peak structure in the XANES. The EXAFS spectra show a rapid formation of the first metallic Ru coordination shell at 2.68 Å and, at higher temperatures, the appearance of higher Ru-Ru coordination shells between 3 Å and 5 Å. At a temperature of 374°C, supercritical conditions were reached in the reactor. Even under these conditions, the Ru particles remained in the metallic state and thus represent the active catalyst phase during supercritical water gasification, confirming and substantially extending previously reported data.[46]

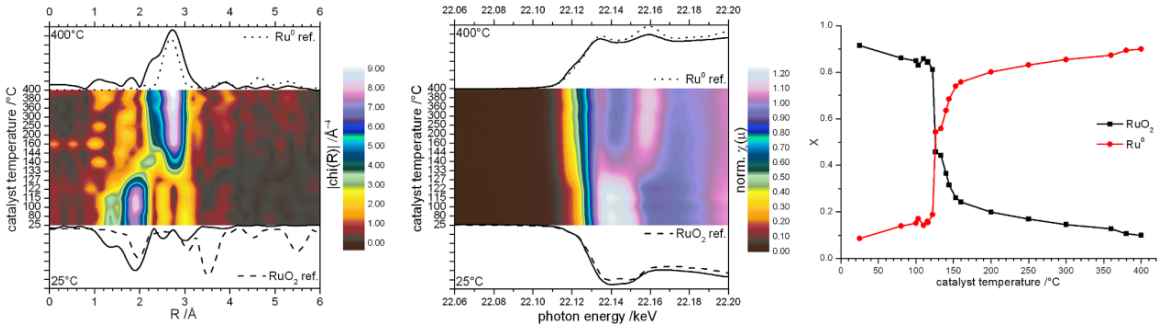

***Figure 6.1**: In situ EXAFS (left) and XANES (center) of a Ru/C catalyst during heat-up in 7.5% ethanol in water at 24.5 MPa (experiment Ci-2). The heating rate between temperature steps was 60 K/min, the dwell time at each temperature step was 10 min before a spectrum was recorded; the acquisition time per spectrum was 180 s. Reference spectra of bulk RuO_2 (dashed line) and bulk Ru^0 (dotted line) are shown in the EXAFS and XANES graphs. The composition of the catalyst, obtained by LCF of the XANES spectra, is shown on the right.*

From the EXAFS spectrum, the ruthenium particle size of the catalyst under process conditions can be calculated via fitting with theoretical standards and comparison with a ruthenium bulk reference, a standard procedure that has been described in detail elsewhere[124] (Figure 6.2). Fit results obtained by fitting the 1st and 2nd Ru coordination shells of the Ru/C catalyst during the continuous gasification of 7.5% ethanol in water at 400°C and 24.5 MPa are presented in Table 6.1. From the calculated coordination numbers (CN), an estimate of the mean particle size can be made. Principally, the CN of the first coordination shell is sufficient for particle size estimation, however, calculating the ratio between 1st and 2nd shell CNs gives more reliable results.[125,126]

	1st Ru-S shell	1st Ru-Ru shell	2nd Ru-Ru shell
CN	*1.0(2)*	**6.7(6)** *5.9(3)*	**2.2(6)** *1.9(4)*
R (Å)	*2.35(2)*	**2.66(1)** *2.66(1)*	**3.78(2)** *3.78(1)*
ΔE_0 (eV)	*10.0(2.7)*	**3.6(7)** *2.4(1.1)*	**3.6(7)** *2.4(1.1)*
σ^2 (Å^2)	*0.006(2)*	**0.0097(5)** *0.0094(3)*	**0.0097(5)** *0.0094(3)*

***Table 6.1**: Structural parameters obtained by fitting the EXAFS spectra of active (bold) and sulfur poisoned (italic) Ru/C catalysts shown in Figure 6.2. Fitting parameters: coordination number CN, bond length R, energy shift ΔE and pseudo Debye-Waller factor σ^2.*

In this case, the CNs of 6.7 and 2.2 for the 1st and 2nd coordination shells, respectively, point to a spherical particle size of around 1.0 nm or about 35 Ru atoms. The magnitude of the 2nd coordination shell indicates that there is no significant amount of Ru clusters thinner than 3 atomic layers, as next-neighbor coordination shells do not exist in single and double layer clusters (disks).[125] These results are in good agreement with scanning tunneling electron microscopy (STEM) images of a fresh and a spent Ru/C catalyst that show a particle size of below 1 nm for the fresh catalyst and around 1.5 nm for the spent catalyst (Figure 6.3).[50]

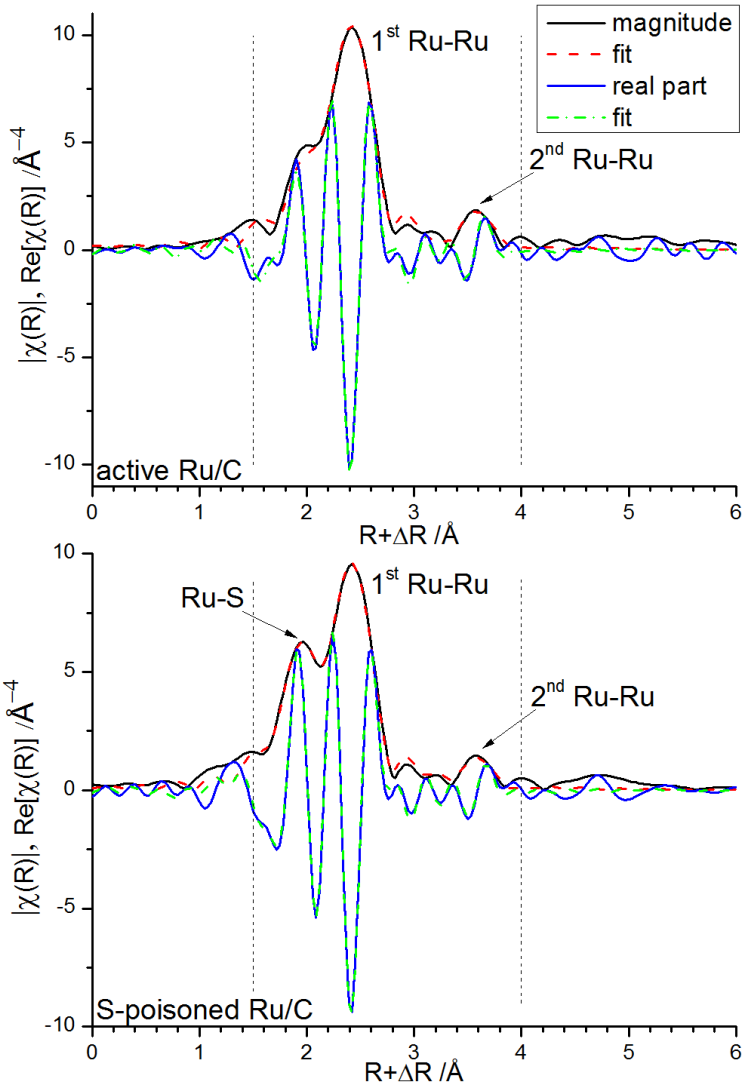

***Figure 6.2**: Magnitude and real part of the Fourier transformed in situ EXAFS spectra of an active and a sulfur poisoned Ru/C catalyst during the continuous gasification of 7.5% ethanol in SCW at 400°C and 24.5 MPa, along with the best fit. Dashed vertical lines indicate the fitting range.*

Hence, the reductive activation of the fresh Ru/C catalyst in the supercritical medium does not seem to cause significant particle growth. However, minor particle growth has been reported for a Ru/C catalyst after 220 hrs of continuous synthetic liquefied wood gasification in SCW, due to sintering.[50] To the best of our knowledge, these results represent the first full structural analysis of a working catalyst based on in situ EXAFS spectroscopy under SCW conditions. Verifying the electronic state, structure and stability of the Ru particles under process conditions proved essential for a quantitative understanding of sulfur poisoning, as explained in the following paragraphs.

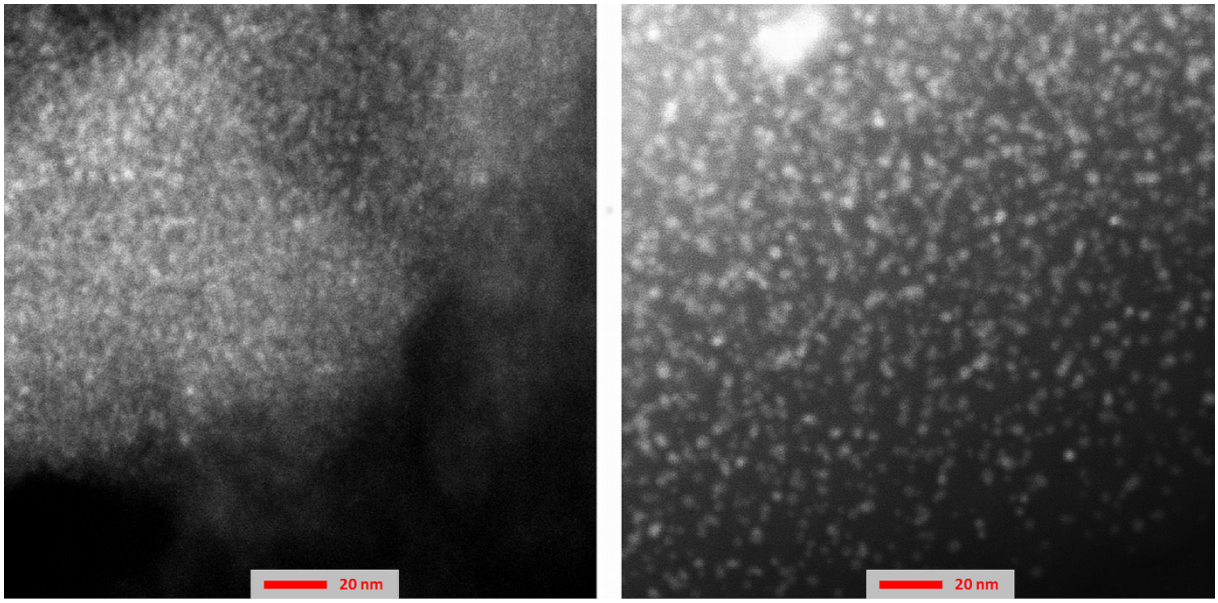

***Figure 6.3**: HAAFD-STEM images of a fresh Ru/C catalyst (left) and a Ru/C catalyst after 24 hrs of continuous glycerol gasification (right). The fresh Ru/C presents Ru particles too small to be properly resolved with an average size below 1 nm. After 24 hrs of glycerol gasification in SCW, a minor particle growth could be observed, with Ru particle sizes between 1 nm and 2 nm. The red scale bar in the images represents 20 nm.*

6.3.2 Catalyst poisoning

The product gas composition during the gasification of 7.5% ethanol in supercritical water is shown in Figure 6.4. Through interaction with SCW and the Ru/C catalyst, ethanol is reformed into a product gas rich in methane and carbon dioxide, with minor amounts of hydrogen and carbon monoxide. Under these reaction conditions, full carbon to gas conversion was achieved and no significant amounts of side or intermediate products were detected in the liquid effluent (see Table 6.2).

		active Ru/C	S-poisoned Ru/C	AC support
7.5% EtOH in water				
conversion	%	99.9	29.8	0.2
product gas	ml/min	46.5	28.6	0.6
CO_2	% *(ml/min)*	21.9 *(10.2)*	3.9 *(1.1)*	12.7 *(0.08)*
H_2	% *(ml/min)*	18.2 *(8.5)*	59.9 *(17.1)*	51.0 *(0.3)*
CH_4	% *(ml/min)*	59.8 *(27.8)*	20 *(5.7)*	29.2 *(0.18)*
CO	% *(ml/min)*	0.15 *(0.07)*	15.7 *(4.5)*	7.2 *(0.04)*
7.0% acetaldehyde in water				
conversion	%	99.8	2.6	-
product gas	ml/min	43.63	1.06	-
CO_2	% *(ml/min)*	33.1 *(14.4)*	12.4 *(0.13)*	-
H_2	% *(ml/min)*	6.0 *(2.6)*	9.9 *(0.1)*	-
CH_4	% *(ml/min)*	60.9 *(26.6)*	50.2 *(0.53)*	-
CO	% *(ml/min)*	0.0	27.5 *(0.29)*	-
10.4 % MeOH in water				
conversion	%	99.9	-	-
product gas	ml/min	46.5	-	-
CO_2	% *(ml/min)*	19.8 *(9.2)*	-	-
H_2	% *(ml/min)*	25.6 *(11.9)*	-	-
CH_4	% *(ml/min)*	54.2 *(25.2)*	-	-
CO	% *(ml/min)*	0.1 *(0.05)*	-	-

***Table 6.2**: Total carbon to gas conversion, product gas flow rates and compositions for the gasification of ethanol, acetaldehyde and methanol over active and S-poisoned Ru/C as well as pure activated carbon (experiments C-2 to C-4). All experiments were run at 400°C and 24.5 MPa, using 200 mg of Ru/C or carbon support. The three different feeds contained the same concentration of carbon (3.8 wt%); hence, the amount of carbon fed to the reactor per unit time was constant (1.6 mmol carbon per minute).*

Approximately 10 minutes after supercritical conditions have been reached at the catalyst bed, the product gas is detected by a mass spectrometer. The product gas was composed of about 60% methane. The gas composition remained stable over more than two hours and thus represents the product gas for ethanol reforming in SCW over an active Ru/C catalyst under these reaction conditions. The methane concentration achieved under these reaction conditions is high but below the theoretical limit of 75%, as shown in equation 6.1. Due to the thermodynamic equilibrium of the methanation reaction, residual hydrogen remains in the product gas, as explained elsewhere.[46]

$$4\ C_nH_{(2n+2)}O + (2n-4)\ H_2O \xrightarrow[Ru/C]{SCW} 3n\ CH_4 + n\ CO_2 \quad (6.1)$$

After a runtime of 180 minutes, sulfur poisoning of the Ru catalyst was initiated by adding 200 ppm of dimethyl sulfoxide to the 7.5 % ethanol feed, resulting in a concentration of 81 ppm sulfur being continuously fed to the catalyst. Upon addition of sulfur, catalyst poisoning readily set in, leading to a severe change in product gas composition, a drop in product gas flow rate by 40% and a decrease in carbon conversion to about 30% (Table 6.2). The observed fluctuations in gas composition are not due to a fluctuating catalyst activity but are a result of the slug flow of gas and liquid in the setup, as discussed in chapter 3. Complete catalyst poisoning, indicated by a stable product gas composition, was achieved after about 45 minutes, corresponding to an atomic S_{fed}/Ru_{total} ratio of 1.7. It needs to be noted that this ratio is an overestimation due to the time lag between complete sulfur poisoning of the catalyst and detection of a stable gas composition at the MS. By then, both the methane and carbon dioxide concentrations in the product gas had dropped significantly whereas the hydrogen and carbon monoxide concentrations strongly increased. Interestingly, the sulfur poisoned catalyst still showed some activity for methanation, however at only 20% of the original methane production whereas the production of hydrogen more than doubled.

A blank experiment, in which ethanol in SCW passed through the reactor filled with pure, Ru-free carbon support (BASF; same carbon support as used for catalyst preparation) gave no significant gas evolution, confirming the activity of the sulfur poisoned Ru/C. In order to investigate whether the observed product gas stems from direct gasification of ethanol over S-Ru/C or from intermediate products, we gasified acetaldehyde (the main intermediate during ethanol steam reforming)[127] over active and S-poisoned Ru/C. However, the carbon conversions and product gas compositions presented in Table 6.2 suggest that direct ethanol gasification is taking place since the gasification of acetaldehyde over S-Ru/C does not lead to a significant gas production (an acetaldehyde conversion of only 2.6% was observed, but 29.8% conversion in the case of ethanol).

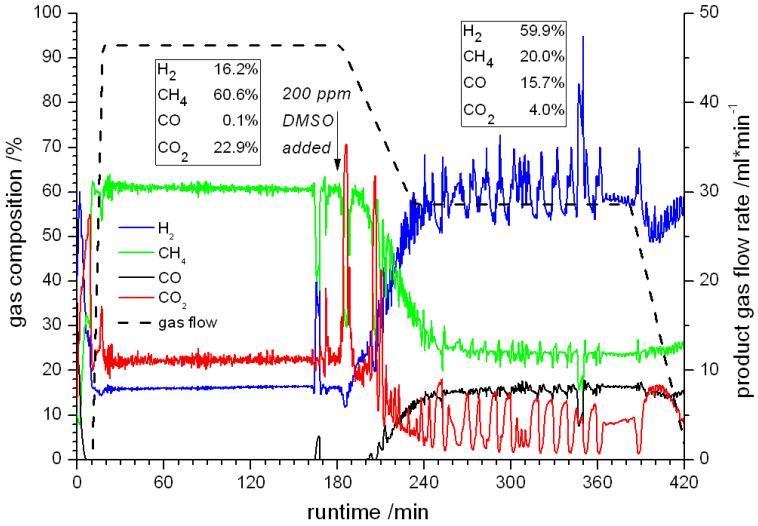

***Figure 6.4**: Composition and flow rate of product gas during the continuous gasification of 7.5% ethanol in SCW at 400°C and 24.5 MPa (experiment C-5). Supercritical conditions at the catalyst bed had been reached at t=0; product gas arrived at the MS after 10 min. Catalyst poisoning was initiated after 180 minutes and deionized water was fed from 370 minutes onwards. Oscillations in gas composition (particularly visible after sulfur poisoning of the catalyst) are due to the slug flow of compressed gas and water in the high pressure setup, as discussed in chapter 3.*

When gasification was continued with sulfur-free 7.5% EtOH in water (not shown in graph) after complete sulfur poisoning, no change in gas composition was observed. Flushing the catalyst with pure SCW also did not lead to an increase in catalytic activity, indicating that sulfur poisoning is an irreversible process. Hence, a more severe treatment seems to be necessary in order to remove sulfur from the Ru surface, presenting a challenge for the development of regeneration protocols.

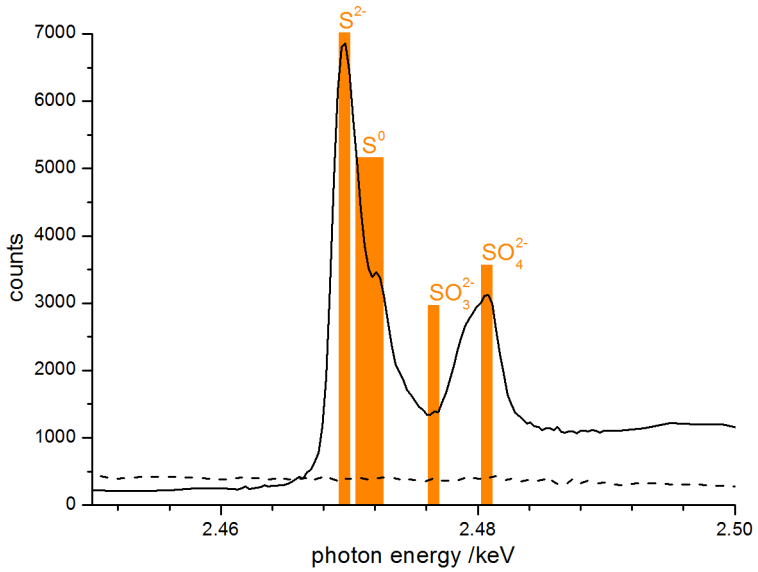

***Figure 6.5**: Ex situ sulfur K-edge XANES spectrum of a sulfur poisoned Ru/C catalyst, extracted from the continuous flow reactor under inert atmosphere (solid line). The orange bars indicate typical absorption peak positions for several sulfur species. As reference, sulfur K-edge XANES of a sample of pure carbon support that was placed in the reactor along with the Ru/C catalyst was measured, showing that no sulfur is present on the carbon support (dashed line).*

When complete catalyst poisoning had been achieved, in situ EXAFS spectra of the sulfur poisoned Ru/C catalyst were taken (Figure 6.2). Compared to the EXAFS spectrum of the active catalyst, a new coordination shell emerged at 2.35 Å, in addition to the shells corresponding to metallic ruthenium. By comparing with a theoretical standard of RuS_2, the new shell was assigned to a Ru-S bond, leading to a good fit of the EXAFS spectrum.[119] The presence of reduced sulfur species on the poisoned catalyst was confirmed by measuring the sulfur K-edge XANES of a catalyst sample which was extracted from the reactor after complete sulfur poisoning and subsequent purging with sulfur free feed at 400°C for one hour (Figure 6.5). After this treatment, only permanently bound sulfur was expected to remain on the catalyst. The samples were handled in a glove box under N_2 atmosphere to avoid oxidation. To verify that the Ru particles of the catalyst had not been oxidized during sample preparation, XANES spectra at the L_3-edge of Ru were also recorded (Figure 6.6). The S-XANES spectrum shows that sulfur predominantly exists as S^{2-} on the catalyst particles with minor contributions from more oxidized species, namely S^0 (possibly bound in organic sulfur compounds) and S^{VI} (as SO_4^{2-}). Since the absorption peak intensity of S^{VI} is about 6 times higher than that of S^{2-}, the magnitudes of the peaks in the spectrum do not represent the

quantitative ratio between S^{II-} and S^{VI} species.[128–130] The amount of S^{VI} species can thus be considered negligible and is most likely due to the brief contact with residual oxygen in the glove box during sample preparation. A sample of pure carbon support (BASF; same carbon support as used for catalyst preparation) that was placed in the reactor along with the Ru/C catalyst showed no significant amounts of adsorbed sulfur, indicating that the observed sulfur species are indeed adsorbed on the ruthenium particles.

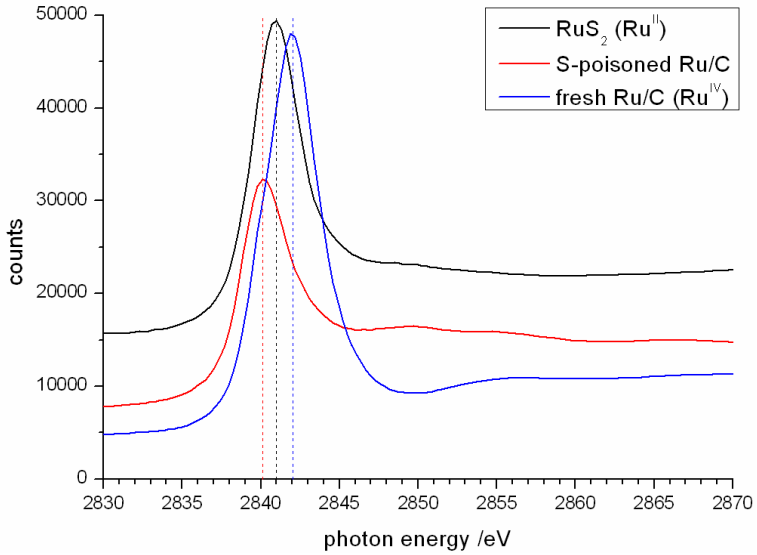

Figure 6.6: Ru L_3-edge XANES spectra of a sulfur poisoned Ru/C catalyst sample along with the spectra obtained from RuS_2 and a fresh Ru/C catalyst as Ru^{II} and Ru^{IV} references, respectively. Dashed lines indicate the positions of the absorption peaks. The spectrum of the S-poisoned catalyst shows that Ru is still in its reduced (metallic) state and has not been oxidized significantly during sample preparation.

Structural results of the EXAFS fit, presented in Table 6.1, suggest a Ru-S CN of 1.0 and thus a mean catalyst composition equivalent to $RuS_{0.33}$, as the bulk RuS_2 standard has a Ru-S CN of 6. Since no bulk sulfidation was observed within 4 hours, it is likely that the sulfur species do not migrate into the Ru particles under these reaction conditions but rather stay exclusively on the surface. Similar results have been obtained when sulfur concentrations of 200 ppm and 500 ppm were used to poison the catalyst, suggesting that $RuS_{0.33}$ represents the sulfur-saturated catalyst phase under these conditions. From the Ru:S stoichiometry of 3:1 a sulfur surface coverage of about 40% can be estimated for a spherical Ru particle of 1 nm in diameter or 35 atoms (hence, a dispersion of about 80%). As a result of the sulfur

adsorption, the Ru-Ru CN decreased slightly. This effect has also been described by Miller and Koningsberger for sulfur poisoning of small Pt particles, which they attributed to a particle flattening due to sulfur poisoning.[131] The qualitative and quantitative structural analysis of the sulfur species on the S-poisoned Ru/C catalyst enabled us to design a DFT model of a sulfur poisoned Ru surface which was used to calculate the free energies of surface adsorbates. In combination with the results from isotope labeling experiments, these calculations unraveled the effect of sulfur poisoning on the methanation reaction pathway, as explained in the following section.

6.3.3 Pathway of the methanation reaction

Chapter 5 outlined how the nature and free energies of hydrocarbon adsorbates that take part in the methanation reaction on a ruthenium surface can be studied by DFT calculations and by reforming methane in supercritical, deuterated water (D_2O) using a Ru/C catalyst. The computational results suggested that CH_4 undergoes rapid scrambling on a Ru surface and that C* and CH* are the most stable and thus most predominant adsorbates on an active Ru catalyst under hydrothermal conditions, resulting in methane carrying three and four deuterium atoms. Figure 6.7 shows the calculated free energy levels of CH_x adsorbates on a stepped, clean Ru surface, presenting B5 surface sites which are considered the active sites for the methanation reaction.[132–134]

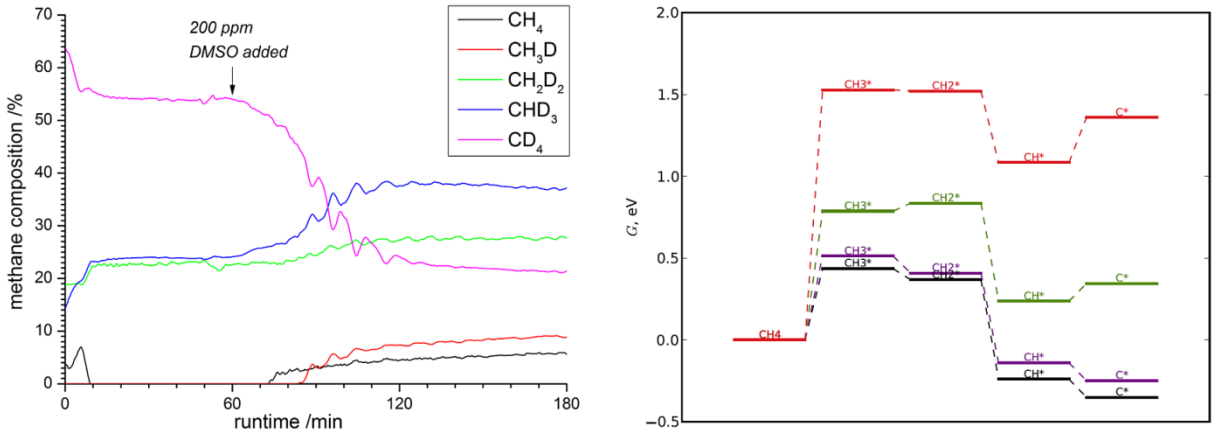

***Figure 6.7**: Left: Composition of methane produced by the continuous, Ru/C catalyzed gasification of 7.5% ethanol in deuterated water at 400°C and 24.5 MPa (experiment Ci-3). Supercritical conditions at the catalyst bed had been reached at t=0. Product gas arrived at the MS after 10 min; catalyst poisoning was initiated after 60 minutes. Right: Free energies of CH_x adsorbates on a 3x3 atoms, (211) fcc Ru surface. The energy levels for adsorbates on the clean (black) Ru surface and the Ru surface poisoned by one (violet), two (green) and three (red) sulfur atoms are shown.*

In order to relate these findings to the reforming of larger organic molecules in SCW, methanol was chosen as a model for oxygenated organics. It behaves similarly to ethanol, forming methane as the main product gas under SCWG conditions along with hydrogen and carbon dioxide, as expected for the SCWG of alcohols (see Table 6.2 and Equation 6.1). Since methanol only bears one carbon atom it is ensured that all carbon atoms interacting with the Ru surface have the same initial chemical surrounding and thus reactivity. Reforming of methanol in SC D_2O in batch reactors showed that the very same hydrocarbon adsorbates – as explained above in the case of methane – were the probable intermediate surface species formed on a Ru surface during the hydrothermal gasification of oxygenated organic molecules (Figure 6.8). Again, adsorbed C* and CH* seemed to be the most abundant surface species that take part in the methanation step, resulting in a product gas mainly composed of CD_4 and CHD_3 via uptake of water-derived deuterium. A similar result was obtained by Park and Tomiyasu for the Ru catalyzed reforming of naphthalene[43] – a much larger and more complex molecule – in SC D_2O, suggesting that the described surface adsorbates are typical intermediate surface species during the reforming of any kind of organics in SCW.

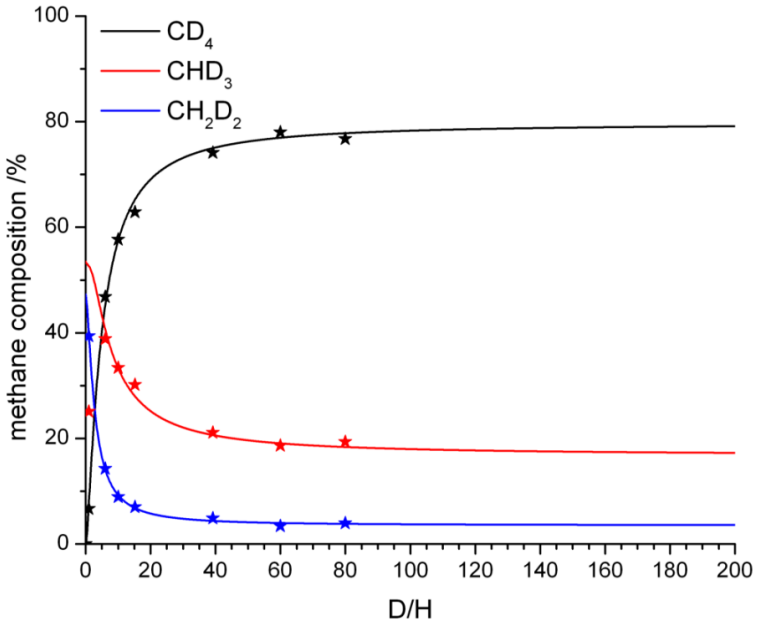

***Figure 6.8**: Composition of methane obtained from batch gasification (398°C, 26 MPa) of MeOH in D_2O, varying the D/H ratio in the mixture (experiments B-4 to B-10). Asterisks represent the experimentally determined values, solid lines the fits by a logistic growth function for D/H>4. CH_3D and CH_4 are omitted as they were not detected for D/H ≥ 4.*

By varying the methanol concentration, and thus the D/H ratio in the reactor, it was possible to study these surface species in a quantitative manner. At low D/H values, hence at high methanol concentrations in the feed, the composition of the produced methane is very sensitive to the ratio between deuterium and hydrogen. In this regime, the catalyst surface is populated by large amounts of both water-derived deuterium and methanol-derived hydrogen, leading to a statistical distribution of D and H in the produced methane (Figure 6.8). Therefore, the ratio between the several possible CH_xD_{4-x} species in the produced methane is not representative of the ratio between the CH_x adsorbates that originated from the adsorption and subsequent degradation of methanol on the Ru surface. However, for high D/H values, the composition of the produced methane becomes independent of the D/H ratio in the feed. The fitted curves in Figure 6.8 essentially show an extrapolation to zero percent methanol, hence infinite D/H, at which point the distribution of hydrogen and deuterium in the produced methane is not governed by statistics anymore. Interestingly, a stable ratio between CD_4, CHD_3 and CH_2D_2 is reached at high D/H, pointing to a 79:17:4 ratio between C*, CH* and CH_2* adsorbates on the catalyst surface which correlates well with the relative levels of their free energies (meaning that the abundance of surface species with

lowest free energies, CH* and C*, is reflected in the favored generation of CHD_3 and CD_4, respectively; see Figure 6.7). These adsorbates then have to undergo hydrogenation by surface-bound deuterium directly in order to lead to the observed composition of methane.

To study the effect of sulfur poisoning on the nature and abundance of these surface intermediates, 7.5 % ethanol in deuterated water (D/H = 9.5) was continuously gasified at 400°C and 24.5 MPa. Similar to the aforementioned batch experiments, the active Ru/C catalyst produced methane with a very high CD_4 content and much smaller, though almost equal, amounts of CHD_3 and CH_2D_2 (Figure 6.7). The more hydrogenated methane species, CH_3D and CH_4, could not be detected, suggesting that no significant amount of CH_3* was present on the Ru surface which would lead to CH_3D and CH_4 via uptake of a surface bound deuterium and hydrogen, respectively. Thus, ethanol is largely dehydrogenated during the process of breaking C-C and C-O bonds and the hydrogen atoms present in the methane originate from surface-bound hydrogen species, not directly from the biomolecule itself.

The degradation of organic molecules on Ru/C, and in particular the fate of the C-O bond in these molecules, was further studied by using ^{13}C labeled ethanol and acetic acid. In both compounds, the functionalized carbon atom (hence, the hydroxylated and carboxylated ones, respectively) were labeled to 99.8% with ^{13}C. Upon hydrothermal gasification of these compounds over Ru/C, several gaseous reaction products, containing either ^{12}C or ^{13}C, are possible as shown in the equations below:

$$CH_3\text{-}{}^{13}CH_2\text{-}OH \xrightarrow[400°C,\ 25\ MPa]{Ru/C,\ H_2O} {}^{12}CH_4 + {}^{13}CH_4 + {}^{12}CO_2 + {}^{13}CO_2\ (+\ {}^{12}CO + {}^{13}CO)$$

$$CH_3\text{-}{}^{13}COOH \rightarrow {}^{12}CH_4 + {}^{13}CH_4 + {}^{12}CO_2 + {}^{13}CO_2\ (+\ {}^{12}CO + {}^{13}CO)$$

$$CH_3\text{-}{}^{13}COOH \dashrightarrow {}^{12}CH_4 + {}^{13}CO_2$$

For an unbiased degradation of these compounds down to C* and CH* adsorbates, independent of the position of the carbon in the original molecule (hence, equivalent behavior for ^{12}C and ^{13}C), one would expect an even distribution of ^{12}C and ^{13}C over the product gases. For example, this would lead to methane with a ^{12}C to ^{13}C ratio of 1. On the

other hand, a preferential formation of carbon oxides from the functionalized carbon in the molecule, due to its C-O bond and higher oxidation state, would lead to e.g. carbon dioxide with a ^{12}C to ^{13}C ratio below 1. Acetic acid also presents a third option, an immediate C-C bond cleavage (direct decarboxylation) that directly leads to the formation of methane and carbon dioxide. This mechanism has often been suggested in literature.[135] This pathway would exclusively lead to the formation of $^{12}CH_4$ and $^{13}CO_2$.

Results from the batch gasification of these ^{13}C labeled compounds are shown in Figure 6.9. On active Ru/C, both compounds behave similarly, forming methane with about 35% ^{13}C and carbon dioxide with around 65% ^{13}C. The results show that acetic acid does not decarboxylate directly but rather follows a pathway similar to ethanol, where the molecule is broken down to C* and CH* adsorbates. However, in both cases there is a slight preference to form carbon dioxide from the ^{13}C labeled, functionalized carbon which might be due to the fact that this carbon is already bound to oxygen. Still, about 35% of carbon atoms going into CO_2 formation originated from the ^{12}C methyl group, supporting the suggested pathway of degradation and methanation of organics on Ru/C.

During the continuous gasification of EtOH in D_2O, the product gas flow rate again dropped by 40% upon sulfur poisoning but more intriguingly the composition of the produced methane changed. The severe drop in CD_4 concentration along with the significantly increased CHD_3 and the slightly increased CH_2D_2 production suggest a decrease in the fraction of carbon atoms that reach the fully dehydrogenated surface state, C*, and an increase in CH* and CH_2* on the Ru surface. Furthermore, sulfur poisoning led to a significant production of CH_3D and CH_4, indicating an increased presence of CH_3* adsorbates on the catalyst surface due to a lower dehydrogenation rate.

This is also reflected in the results obtained by ^{13}C labeling. The gasification of both ethanol and acetic acid over sulfur poisoned Ru/C led to the almost exclusive formation of $^{12}CH_4$ and $^{13}CO_2$, suggesting limited C-H and C-O bond breaking capability of the poisoned catalyst in addition to the lowered C-C bond breaking activity that leads to an overall lower conversion.

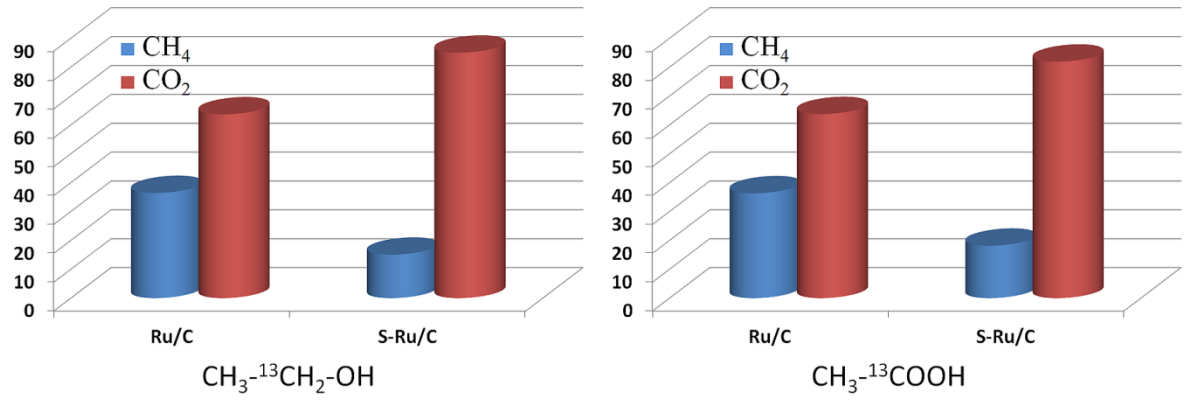

***Figure 6.9**: Concentration of ^{13}C in methane and carbon dioxide that are generated by gasifying ^{13}C labeled ethanol and acetic acid over active Ru/C and sulfur poisoned S-Ru/C, respectively, in a batch reactor (experiments B-11 to B-14). In both organic compounds, the functionalized carbon has been labeled. Carbon monoxide was not detected.*

The decreased dehydrogenation of the hydrocarbon adsorbates is also reflected in a high deuterium concentration of 88% in the produced hydrogen vs. only 63% in the produced methane (see Table 6.3). Since both the flow rate and deuterium content of hydrogen increased upon sulfur poisoning of the Ru/C catalyst, the dissociation of water on the Ru surface seems to be facilitated by sulfur poisoning, in contrast to the dehydrogenation of CH_x species.

	active Ru/C	S-poisoned Ru/C
CH_4	-	7.2%
CH_3D	-	9.3%
CH_2D_2	22.8%	27.1%
CHD_3	23.7%	35.9%
CD_4	53.5%	20.5%
D-content	82.8%	63.3%
H_2	7.5%	2.7%
HD	27.4%	18.0%
D_2	65.1%	79.4%
D-content	78.8%	88.4%

Table 6.3: Composition and deuterium content of methane and hydrogen produced by an active and a sulfur poisoned Ru/C catalyst during the continuous gasification of 7.5% EtOH in deuterated water at 400°C and 24.5 MPa (experiment Ci-3).

To add insight to the experimental results, the free energies of CH_x adsorbates on a sulfur poisoned Ru surface at 400°C and 25 MPa were calculated. A stepped, periodic 3×3 atoms Ru surface was used, poisoned by one, two and three sulfur atoms, corresponding to a sulfur surface coverage of 1/9, 2/9 and 1/3, respectively (Figure 6.7). At low sulfur surface coverage, the free energies of all adsorbates are slightly elevated but remain on similar levels with respect to each other, when compared to the clean Ru surface. This would lead to a decrease in reaction rate, due to a higher energy penalty to form CH_3*, but not to a significant change in the composition of the deuterated methane as C* and CH* are still the most favorable (hydro-) carbon adsorbates. At higher sulfur coverage, however, the adsorbate energy levels start to shift strongly with respect to each other and CH* emerges as the new lowest energy adsorbate. This effect is particularly pronounced at 1/3 sulfur coverage which is in the range of the experimentally determined one of 40%. The free energy of CH_3* adsorbates is now significantly increased, leading to the observed 80% drop in methanation rate, but once CH_3* has been formed it is likely to further dehydrogenate to CH* on the Ru surface. CH* will then be the most predominant hydrocarbon species on the catalyst surface whereby a certain amount of CH* will still be stripped of its last hydrogen atom to form C*. These results are in good agreement with the experimentally observed drop in CD_4 concentration and the emergence of CHD_3 as the most abundant deuterated

methane. The appearance of CH_4 and CH_3D along with the slightly increased CH_2D_2 concentration suggests a higher energy barrier for the dehydrogenation steps necessary to form CH_2* and CH*. This would lead to a decreased dehydrogenation rate on the Ru surface, allowing CH_3* and CH_2* adsorbates to be hydrogenated by surface-bound deuterium or hydrogen before reaching the more stable CH* configuration. As a result, more CH_4, CH_3D and CH_2D_2 would be formed compared to the active (clean) Ru surface where the rate of dehydrogenation is much higher. Thus, S-poisoning of the Ru/C catalyst leads not only to a drop in activity but also to a change in product selectivity.

6.4 Conclusions

This chapter presented the pathway of the reductive activation of a carbon supported Ru catalyst used for the reforming of biomass in supercritical water. For the first time, a full structural analysis of a working catalyst via in situ EXAFS under these severe process conditions was carried out, allowing us to determine particle size as well as the electronic and geometric structure of the catalyst in situ. In the presence of organics, the fresh Ru/C catalyst was reduced to its metallic, active form at around 125°C without a change in particle size.

Under supercritical conditions, sulfur poisoning of the catalyst occurred due to surface adsorption of sulfur atoms instead of bulk sulfidation. For complete sulfur poisoning, a surface coverage of about 40% was determined experimentally by in situ XAS, suggesting that a partial sulfur surface coverage is sufficient to block the active sites of the catalyst. Sulfur poisoning lead to an 80% drop in methane production whereas the hydrogen production doubled. Taking the decrease in CO_2 and the increase in CO formation into account, this suggests that both the methanation and the water gas shift reaction are hindered by sulfur poisoning. It was not possible to restore catalytic activity by flushing the catalyst with sulfur-free feed or pure SCW, indicating that sulfur poisoning of Ru/C is an irreversible process and that possible regeneration procedures will have to include a chemical treatment of the S-poisoned catalyst.

Using a combination of DFT calculations and direct chemical probing via isotope labeling, the pathway of the methanation reaction under hydrothermal conditions was resolved. Under SCW conditions, methanation proceeds via direct hydrogenation of (hydro-) carbon adsorbates on the Ru surface instead of the classic methanation pathway via carbon monoxide and hydrogen. On an active catalyst, organic molecules are predominantly broken down and dehydrogenated to surface bound C* before full hydrogenation to methane occurs. Upon sulfur poisoning, stripping of hydrogen from the hydrocarbon adsorbates proceeds at a much lower rate and leads to the preferential formation of CH* instead of C*. The change in the free energies of the (hydro-) carbon adsorbates on an S-poisoned Ru surface explains both the lower overall activity as well as the change in composition of isotope-labeled methane.

This mechanistic insight and the clarification of the methanation pathway in the SCWG of organics were achieved through combination of in situ XAS under hydrothermal conditions with concurrent chemical probing via isotope labeling and electronic structure calculations. The presented results show the strength of a multidisciplinary, methodical approach and we are confident that they will be useful for understanding S-poisoning on various noble metal catalysts and help in designing sulfur resistant catalysts or effective regeneration procedures.

Chapter 7

A protocol for the regeneration of deactivated Ru catalysts

Abstract

Catalytic processes that employ Ru catalysts in supercritical water have been shown to be capable of converting organics, such as wood waste, into synthetic natural gas (CH_4) with high efficiencies at relatively moderate temperatures of around 400°C. However, Ru catalysts are prone to sulfur poisoning and are quickly deactivated. Since sulfur is ubiquitous in raw biomass and technologies to remove sulfur from hydrothermal biomass feeds are lacking, regeneration protocols that efficiently reactivate sulfur-poisoned catalysts are required to realize efficient conversion processes and long catalyst lifetimes. In this chapter, the hydrothermal gasification of ethanol is studied and a method to remove sulfur from a sulfur poisoned Ru catalyst under hydrothermal conditions through an oxidative treatment in aqueous phase is presented. By using in-situ X-ray absorption spectroscopy under reaction conditions, it is shown that Ru is oxidized by dilute hydrogen peroxide at low temperatures, leading to the removal of adsorbed sulfur species from the Ru surface. By optimizing the regeneration conditions, it was possible to prevent oxidation of the catalyst carbon support. This treatment led to a reactivation of the Ru catalyst with a significant increase in carbon to gas conversion and methane selectivity.

Parts of this chapter were submitted to *CHEMCATCHEM* as a full research article.

7.1 Introduction

Besides the deactivation by sulfur poisoning which has been discussed in detail in chapter 6, catalyst fouling through the deposition of coke and intermediate reaction products on the active metal and in the pores of the catalyst support (pore mouth poisoning/plugging) is another typical pathway of catalyst deactivation.

This has been observed in various noble metal catalysts used in steam reforming[136], liquid phase hydrogenation[137–139] and hydrothermal reforming of organics.[140] Deactivation by coking and fouling is often remedied by treatment with steam or hydrogen at high temperatures which, however, requires sufficiently stable catalyst supports and adequate reactors.[136,138] Activated carbon, a catalyst support often used in hydrothermal reforming of organics due to its stability under these reaction conditions, presents a highly porous structure that is very susceptible to fouling and coking through entrapment of reactants in its micro- and mesopores, leading to coke formation and subsequent plugging of these pores.[140] Vogel and co-workers showed that coke and tar formation can be a major issue during processing of organic feedstocks such as glycerol, glucose or fermentation residues in sub- and supercritical water.[141,142] De Vlieger et al. observed the deactivation of Pt/C catalysts during reforming of ethylene glycol and attributed that to the presence of acetic acid as a reaction intermediate which leads to coke formation.[140] In a consecutive study, they used carbon nanofibers (CNFs) as support for a Pt-catalyst for the continuous reforming of acetic acid in supercritical water.[143] They did not observe loss of activity over several hours of operation and concluded that CNF-supported catalysts are less prone to coking as they only present high external surface area but no pore structure.

A few attempts to regenerate sulfur poisoned Ru catalysts under hydrothermal conditions can be found in literature, published by Osada et al. and by Waldner (see Chapter 1). While the “subcritical water regeneration”, presented by Osada et al., remains questionable due to the experimental conditions they applied, the oxidative catalyst treatment, studied by Waldner, showed promising potential. Waldner studied the gasification of ethanol in supercritical water over a Ru/C catalyst at low space velocities and full carbon to gas conversion.[19] After fully deactivating the catalyst by adding sodium sulfate to the ethanol feed, the sulfur poisoned catalyst was treated with dilute hydrogen peroxide at 90°C and

subsequently, the release of ionic species in the liquid effluent was observed. After this treatment, almost full conversion of ethanol was again observed, but the conversion started to slowly decrease to about 80% within 24 hours. While this oxidative catalyst treatment showed promising results, it remained unknown how the hydrogen peroxide interacts with the catalyst. Since Waldner's experiments were run at full carbon to gas conversion, it was unclear how much of the catalytic activity was regained by his method of regeneration. As a reason for the observed re-deactivation, a slow release of residual sulfur species that are stored in the catalyst support were suggested, leading to anew sulfur poisoning of the catalyst.

To establish a knowledge based approach to catalyst regeneration, in situ studies are necessary to probe the catalyst in its actual state under process conditions. Following the approach by Waldner, the regeneration of a Ru/C catalyst used in hydrothermal processing after its deactivation by sulfur poisoning was studied, using dilute hydrogen peroxide as an oxidizing agent that can potentially remove sulfur from the catalyst surface. The same strategy was used to attempt the regeneration of the Ru/C catalyst after being deactivated by coke formation. The effect of hydrogen peroxide on the structure of the Ru catalyst during and after oxidative treatment was probed via in-situ XAS under realistic process conditions. Structural changes of the catalyst support at different regeneration conditions were studied by ex-situ electron microscopy and nitrogen physisorption.

In this chapter, new strategies for the regeneration of a Ru/C catalyst used in hydrothermal processing after deactivation by sulfur poisoning and fouling are presented. A protocol for a mild, liquid phase oxidation of the poisoned catalyst is presented that removes adsorbed sulfur from the active catalyst phase whilst keeping the catalyst and catalyst support intact. The effect of the catalyst support on coke formation is discussed by comparing the resistance to fouling of Ru catalysts supported on activated carbon and CNFs, respectively.

7.2 Experimental part

Two types of tubular reactors have been used for SCWG experiments. For in situ experiments at the synchrotron, the aluminum nitride reactor – described in detail in Chapter 4 – was used. For bench-top experiments in the laboratory, the tubular stainless steel reactor– described in detail in Chapter 3 – was employed.

The commercial Ru/C catalyst (see chapter 4) and a carbon nanofiber-supported Ru catalyst (Ru/CNF), prepared in-house, were used in the gasification experiments. The as-received Ru/C catalyst was crushed in a mortar and sieved to a grain size of 50 to 200 μm. A fixed catalyst bed (typically 200 mg of Ru/C or 50 mg of Ru/CNF) with a length of about 25 mm was used in both reactor types. All chemicals used during gasification and regeneration experiments were of analytical grade (Sigma Aldrich, Alfa Aesar). Deuterated water (99.8% D) was obtained from ARMAR Chemicals, Switzerland. ^{13}C labeled ethanol and acetic acid (both 99% ^{13}C) were purchased from Cambridge Isotope Laboratories, USA.

Product gas composition was monitored online via a mass spectrometer (OmniStar 310, Pfeiffer, Germany) whereas precise measurements of the gas composition were performed offline via a gas chromatograph (HP 6890 Series with HP 1, AT 5 and PLOT Q columns). The carbon to gas conversion was determined by analyzing the carbon content in the feed and the effluent with a total carbon analyzer (vario TOC cube, Elementar, Germany).

Scanning electron microscopy (SEM) images of catalyst samples were taken with a Carl Zeiss Ultra 55 machine.

The in situ XAS measurements were conducted at the Ru K-edge (22.117 keV) in transmission mode at the SuperXAS beamline of the Swiss Light Source (SLS) at the Paul Scherrer Institute (Villigen, Switzerland). XAS data treatment was performed using the IFEFFIT software suite.[80,82]

All XAS data was energy-calibrated by measuring a Ru reference foil (EXAFS Materials, USA) simultaneously with the samples. Linear combination fitting of XANES spectra was done in the range from -20 to 60 eV with respect to the Ru K-edge. Reference spectra were allowed to shift in energy and were assigned a weight between 0 and 1, without forcing the sum of weights to 1.

Fourier transformations of the normalized and background-subtracted EXAFS spectra were carried out over a k-range from 3.5 to 12.5 $Å^{-1}$. Fitting of the EXAFS data was then realized using scattering paths obtained from theoretical standards for metallic Ru, RuO_2 and RuS_2, respectively.[118,119,144] To extract structural parameters from the EXAFS spectra, the fitting strategy outlined in chapter 6, section 6.2.2 was used.

Preparation of Ru/CNF

Carbon nanofibres (MF-C 150, d = 80 - 150 nm, L > 30 μm) were obtained from YourTool GmbH, Austria. The as-received CNF were cleaned in boiling 30% HCl for 10 h followed by a treatment in 60% HNO_3 at 80°C for 5 h. The specific BET surface area of the cleaned CNF was 90 m^2/g. To deposit metal nanoparticles on the CNF, a method described by Sun et al was followed.[145] For impregnation with Ru, 700 mg of the cleaned CNF were placed in a stainless steel autoclave. After addition of 340 mg $RuCl_3$ monohydrate (99.9%, Alfa Aesar) in 11 ml of water, the autoclave was sealed and heated to 400°C for 5 h. After cooling down to room temperature, Ru/CNF was removed from the autoclave, washed with water and dried at 90°C for 10 h. This resulted in a Ru/CNF catalyst with a Ru loading of about 18 wt%.

7.3 Results and Discussion

7.3.1 On-stream regeneration of sulfur poisoned Ru/C

In-situ XAS combined with isotope labeling was used in order to study the on-stream, oxidative regeneration of a sulfur poisoned Ru catalyst (S-Ru/C), both from a structural and mechanistic point of view, during the SCWG of 7.5 % ethanol in heavy water (D_2O). Figure 7.1 shows the Fourier transformed extended X-ray absorption fine structure (EXAFS) spectra of the catalyst and the composition of the produced D-labeled methane collected during the four steps of a poisoning/regeneration cycle: catalyst activation, sulfur poisoning, oxidative regeneration and reactivation. Under reaction conditions (390°C, 24.5 MPa), the active catalyst is composed of fully reduced Ru^0 particles with an average diameter of 1.5 nm (determined by EXAFS and scanning electron microscopy; see chapter 6). In this state of the catalyst, the EXAFS spectrum only shows metallic Ru-Ru coordination shells (CS), with the first CS at 2.66 Å and a much less pronounced second CS at 3.78 Å (Table 7.1 and Figure 7.1, top left).

The methane produced from ethanol gasification on the active catalyst showed a very high CD_4 content with lower, almost equal amounts of CHD_3 and CH_2D_2 (Figure 7.1, center). This is indicative of an active catalyst that breaks down ethanol to C* and CH* adsorbates, as outlined in chapters 5 and 6. Upon sulfur poisoning (by adding 200 ppm of dimethyl sulfoxide to the feed), sulfide (S^{2-}) species were created on the Ru surface, resulting in the formation of Ru-S bonds that are well resolved in the EXAFS spectra. The adsorption of sulfur was irreversible, leading to a permanently poisoned catalyst (see chapter 6). However, the Ru particles retained their metallic character since the first Ru-Ru CS remained the dominating feature in the spectrum. In addition, a Ru-S CS is visible at 2.35 Å (Table 7.1 and Figure 7.1, top right). Sulfur poisoning led to a drop in carbon to gas conversion and, more intriguingly, to a severe drop in CD_4 concentration while CHD_3, CH_3D and CH_4 production increased (Figure 7.1, center).

active Ru/C		1st Ru-Ru	2nd Ru-Ru
CN		6.7(6)	2.2(6)
R (Å)		2.66(1)	3.78(1)
ΔE_0 (eV)		3.6(7)	3.6(7)
σ^2 (Å^2)		0.0097(5)	0.0097(5)

S-Ru/C	1st Ru-S	1st Ru-Ru	2nd Ru-Ru
CN	1.0(2)	5.9(3)	1.9(4)
R (Å)	2.35(2)	2.66(1)	3.78(1)
ΔE_0 (eV)	10.0 (2.7)	2.4(1.1) *	2.4(1.1) *
σ^2 (Å^2)	0.006(2)	0.0094(3) *	0.0094(3) *

oxidized Ru/C	1st Ru-O	1st Ru-Ru	2nd Ru-O
CN	6.0(4)	5.8(4.9)	3.7(5.6)
R (Å)	1.99(2)	3.11(2)	3.3(1)
ΔE_0 (eV)	-2.3(9)*	-2.3(9) *	-2.3(9) *
σ^2 (Å^2)	0.009(3)	0.0180(6) *	0.0180(6) *

regenerated Ru/C	1st Ru-Ru	2nd Ru-Ru
CN	7.2(7)	2.3(8)
R (Å)	2.65(3)	3.77(2)
ΔE_0 (eV)	3.0(5) *	3.0(5) *
σ^2 (Å^2)	0.0104(6) *	0.0104(6) *

**fixed to be the same during the fit*

Table 7.1*: Structural parameters obtained by fitting the EXAFS spectra of active Ru/C, sulfur poisoned S-Ru/C, oxidized Ru/C and regenerated Ru/C, shown in Figure 1. Fitting parameters: coordination number CN, bond length R, energy shift ΔE and pseudo Debye-Waller factor σ^2.*

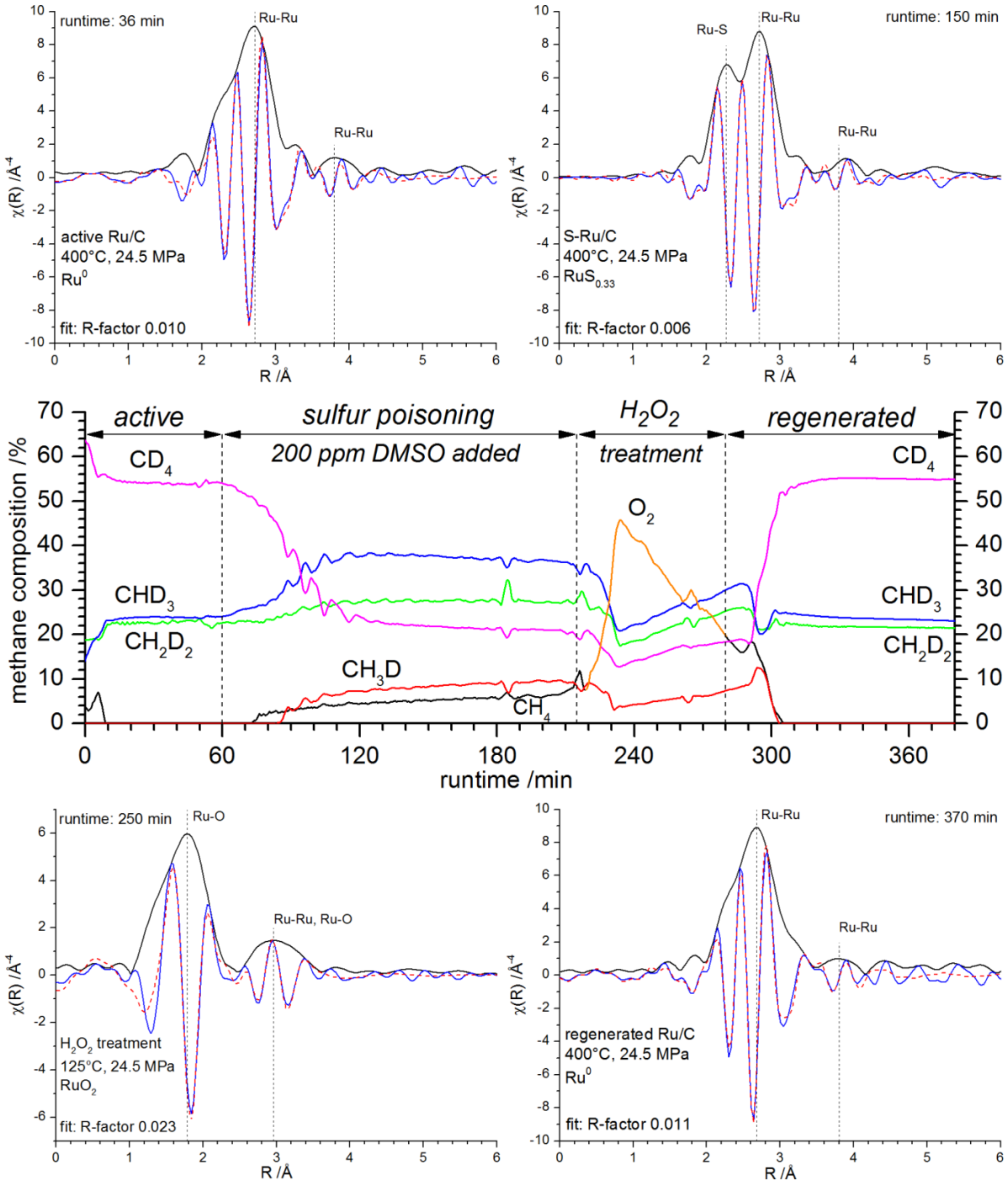

***Figure 7.1**: In-situ FT EXAFS (magnitude: solid black lines, real part: solid blue lines) and fitted spectra (dashed red lines) of a Ru/C catalyst during a full poisoning-regeneration cycle (top and bottom graphs). The observed coordination shells and bond lengths are indicated by dotted vertical lines. The center graph shows the evolution of the D-labeled methane composition during the regeneration cycle. The reactor temperature was generally at 400°C. S-poisoning was initiated at a runtime of 60 min. The regeneration procedure was applied at a reactor temperature of 125°C between 215 and 280 min, during which evolution of oxygen was observed (orange line; oxygen fragment mass 16 interferes with CH_4 measurement). (experiment Ci-3)*

Removal of the adsorbed sulfur was realized via an aqueous phase, oxidative treatment with dilute hydrogen peroxide (H_2O_2). During this oxidative regeneration, the reactor temperature was set to 125°C and the system pressure was maintained at 24.5 MPa. Whilst exposing the sulfur poisoned Ru/C catalyst to 3% H_2O_2 in water, in situ XAS spectra were recorded. Under these conditions, EXAFS measurements showed that S-Ru/C was fully oxidized and converted to RuO_2/C (Figure 7.1, bottom left). After flushing with water, 7.5% EtOH in D_2O was again fed to the reactor, leading to a reduction and thus re-activation of the catalyst. EXAFS analysis of the re-activated catalyst under reaction conditions (390°C, 24.5 MPa) showed metallic Ru as the only quantifiable catalyst phase (Table 7.1 and Figure 7.1, bottom right). The absorption edge step – indicative of the total amount of Ru in the X-ray beam – remained constant, suggesting that no significant leaching of Ru took place during the regeneration process (Figure 7.2).

Furthermore, the comparable magnitudes of the EXAFS spectra of active and re-activated Ru/C show that the oxidative treatment did not lead to an observable particle growth (Ru-Ru coordination numbers remained stable within the margin of analytical error). The D-labeled methane produced by the regenerated catalyst reached the same composition as produced by the active catalyst, suggesting that adsorbed sulfur had been stripped from the Ru surface and that the original distribution of CH_x surface adsorbates had been restored.

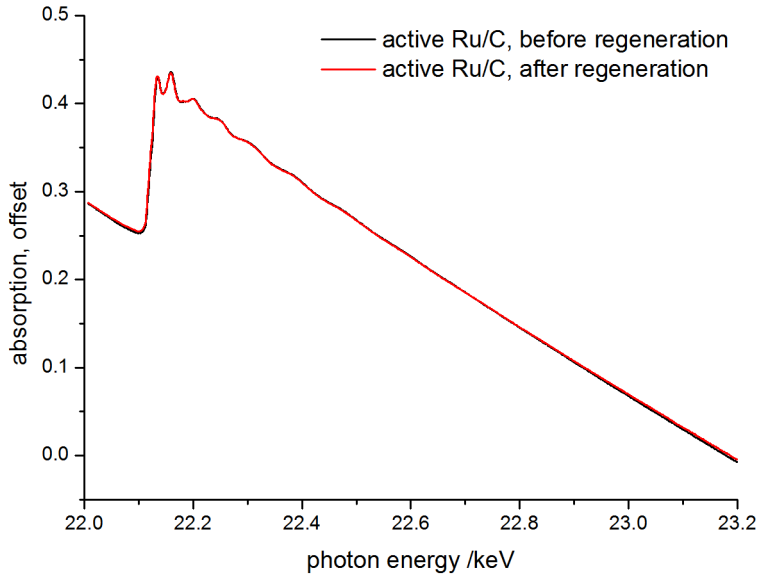

***Figure 7.2**: Raw XAS spectra of the Ru/C catalyst in its active state before sulfur poisoning and oxidative regeneration (black) and afterwards (red). The data shows no significant change in the absorption edge step.*

These results suggest that the adsorbed sulfur can be stripped from S-Ru/C via treatment with dilute H_2O_2 at 125°C. The EXAFS data show that Ru is readily oxidized by H_2O_2, forming RuO_2, whereas it is known from literature that sulfide species can be oxidized to colloidal sulfur, sulfanes and sulfate.[146] These sulfur species can either dissolve in water and be washed off the catalyst (sulfate and sulfane) or are not directly attached to the Ru surface any more (colloidal sulfur). Upon contact with ethanol at temperatures above 125°C, the oxidized Ru catalyst is then reduced to Ru^0 and thus reactivated, concluding the regeneration cycle.

However, the active catalyst phase is only one part of the picture, the other being the catalyst support. For an efficient and reproducible regeneration procedure it is imperative to ensure that the integrity of the catalyst support is not compromised during regeneration.

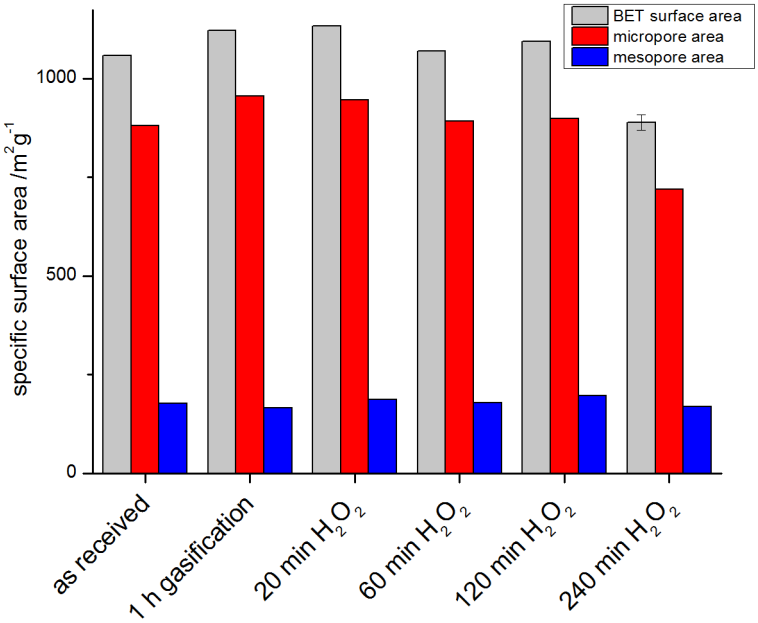

***Figure 7.3**: BET surface area analysis of various Ru/C samples via N_2 physisorption. Treatment with 3% H_2O_2 was performed at 125°C (experiments C-6 to C-10).*

Therefore, the surface area (BET surface) of Ru/C samples that were exposed to H_2O_2 at 125°C for different amounts of time was determined (Figure 7.3). The micro- and mesoporous structure of the carbon support was surprisingly stable under these conditions, showing no significant change in surface area and pore structure for H_2O_2 exposure times of

up to 2 hours. After 4 hours, a drop in the micropore area was observed. However, the macroscopic structure of the carbon particles was severely affected by H_2O_2. Figure 7.4 shows scanning electron microscopy (SEM) images of catalyst grains after exposure to H_2O_2 at 125°C for 4 hours (images A and b). Cracks in the particles are well visible which might have resulted from the mechanical stress that is induced by the evolution of oxygen from H_2O_2 decomposition within the particles. These cracks cut deep into the carbon particles, causing chunks of carbon to flake off of the main particle's surface. Over time, this could lead to total disintegration of the catalyst support. Lowering the temperature had a significant effect on the integrity of the carbon support. After an H_2O_2 exposure time of 4 hours at 75°C, no cracks in the catalyst support were visible (Figure 7.4 C), suggesting that the mechanical stress on the carbon particles had been largely reduced.

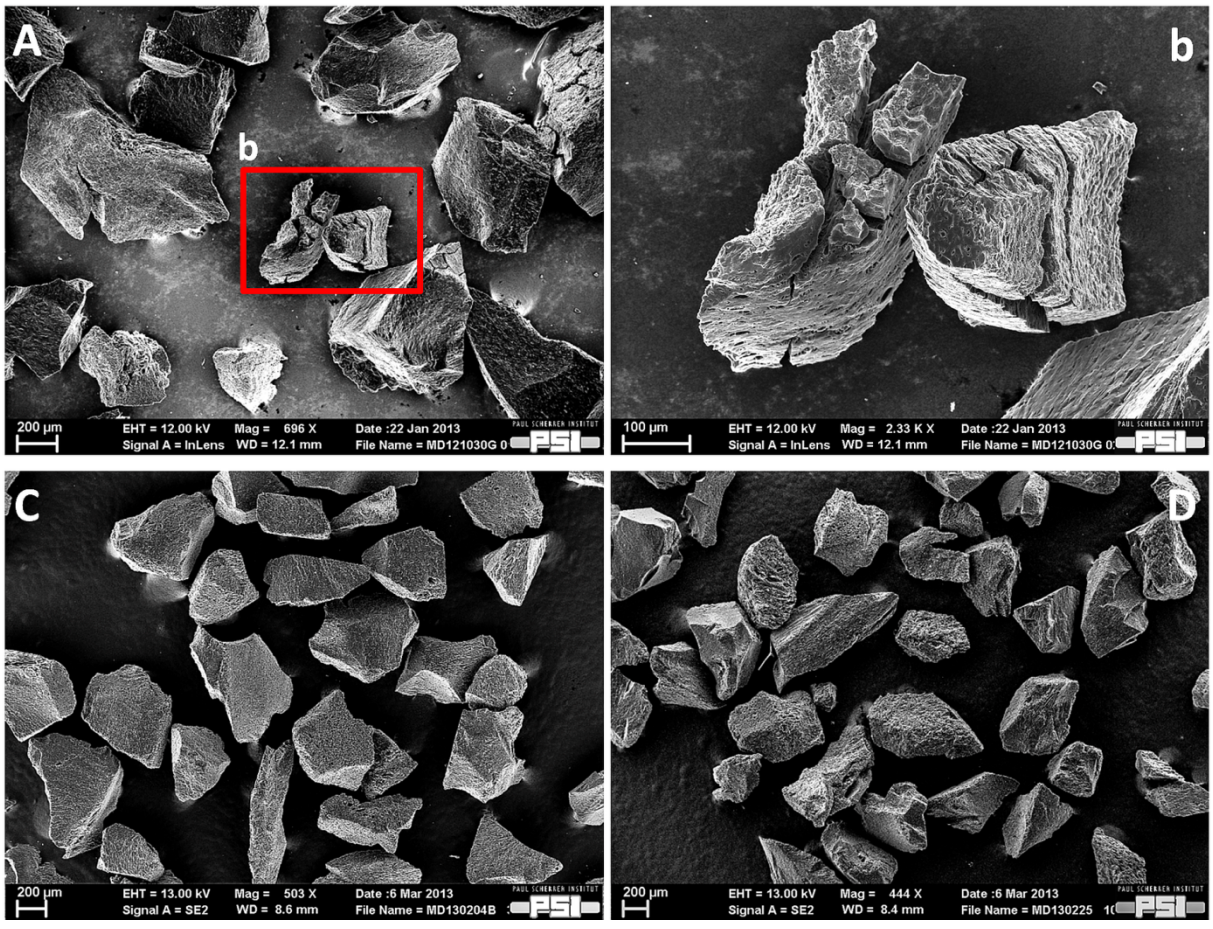

***Figure 7.4**: SEM images of Ru/C samples after oxidative treatment in 3% H_2O_2 at 24.5 MPa. Image A shows Ru/C after treatment at 125°C for 4 h (experiment C-10); the observed cracks in the carbon support are enlarged in image b. Image C shows Ru/C after treatment at 75°C for 4h. Image D shows Ru/C after a 2-step regeneration at 75°C (20 min exposure to H_2O_2 per step) with 60 min of water rinsing at 390°C between the steps (experiments C-11 and C-12). In the two latter cases, no particle corrosion could be observed.*

To determine whether S-Ru/C can be sufficiently oxidized at lower temperatures to remove the adsorbed sulfur, the oxidation of Ru particles during regeneration was followed by in-situ X-ray absorption near edge structure spectroscopy at different temperatures. A sample of S-Ru/C was heated up stepwise in dilute H_2O_2 and XANES spectra were taken after a dwell time of 5 min at each temperature step (Figure 7.5). Upon contact with H_2O_2, Ru was quickly oxidized and above 70°C the spectra closely resembled that of a fresh catalyst which is composed of pure RuO_2. Linear combination fitting of the XANES spectra with fully reduced and fully oxidized Ru/C as standards showed that RuO_2 is the predominant catalyst phase above 50°C while for temperatures above 110°C near complete oxidation to RuO_2 was achieved (Figure 7.5).

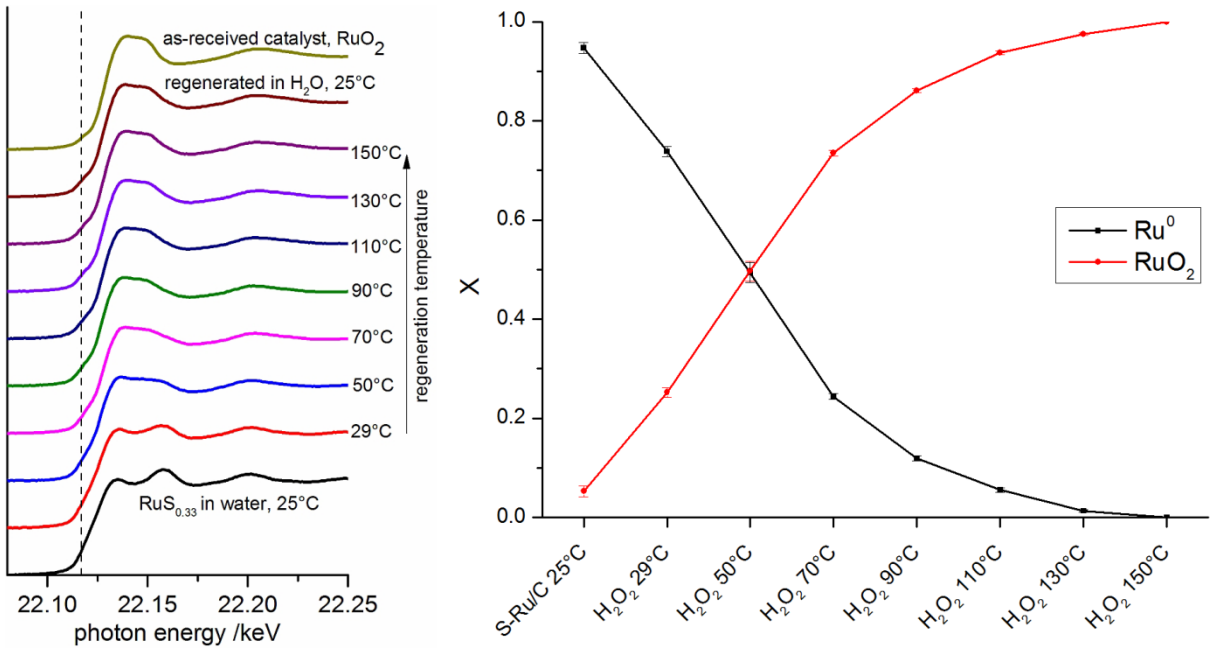

***Figure 7.5**: Left: in-situ XANES spectra of S-Ru/C in 3% H_2O_2. The temperature was increased stepwise; dwell time was 5 min, acquisition time per spectrum was 30 s (experiment Ci-4). The spectrum of an as-received catalyst sample (RuO_2/C) is given as a reference. The dashed vertical line indicates the absorption edge of Ru^0. Right: Linear combination fit of the XANES spectra of S-Ru/C during oxidative treatment, using fully reduced Ru/C (Ru^0) and fully oxidized Ru/C (RuO_2) as standards.*

Based on these results, regeneration of S-Ru/C was attempted at lower temperatures. Even at temperatures as low as 75°C, the H_2O_2 treatment lead to a regeneration of catalytic activity as indicated by the high conversion and methane selectivity of the catalyst after the

oxidative treatment (Table 7.2). However, temperatures below 125°C required a 2-step regeneration procedure in which the catalyst was treated with H_2O_2 at the chosen regeneration temperature and then rinsed with water, followed by another H_2O_2 treatment. Simply doubling the regeneration time at temperatures below 125°C (hence, 40 min instead of 2 × 20 min) did not show the same regeneration efficiency as the 2-step process. The temperature of the water rinsing step also played a role, insofar as higher temperatures facilitated higher regeneration efficiencies, with SCW at 390°C showing the best results. Hence, the data suggest that the (oxidized) sulfur species that are generated at low regeneration temperatures need higher temperatures to be removed from the oxidized Ru/C catalyst. The 2-step regeneration process with intermediate water rinsing at 390°C also did not cause corrosion of the carbon support (Figure 7.4 D).

sample	regeneration steps	% conversion[a]	carbon selectivity	
fresh Ru/C	-	99.9	CH_4	0.75
			CO_2	0.25
			CO	0.01
S-Ru/C	-	29.8	CH_4	0.51
			CO_2	0.11
			CO	0.38
reg. @ 125°C	1 × 20min	99.7	CH_4	0.71
			CO_2	0.28
			CO	0
reg. @ 100°C	2 × 20min	99.7	CH_4	0.75
			CO_2	0.25
			CO	0
reg. @ 100°C	1 × 40min	81.8	CH_4	0.61
			CO_2	0.29
			CO	0.1
reg. @ 75°C	2 × 20min	99.8	CH_4	0.77
			CO_2	0.23
			CO	0

[a] *carbon to gas conversion*

Table 7.2*: Carbon to gas conversion and selectivity of Ru/C after regeneration at different temperatures. The organic feed was 7.5% EtOH in water at 390°C and 25 MPa (experiments C-13 to C-18). Water rinsing between regeneration steps was carried out at 390°C for 60 min.*

Since experiments at full conversion do not show the true (hence, maximal) activity of a catalyst, the Ru/C catalyst was run at partial carbon-to-gas (c-t-g) conversion to assess the efficiency and sustainability of the regeneration procedure. This allows to directly quantify how much of the original catalytic activity can be regained by the oxidative treatment. Figure 7.6 shows the progression of catalytic activity and c-t-g selectivity for a 2-step regeneration at 75°C. While the active catalyst showed high methane selectivity and c-t-g conversion, the conversion dropped to about 9% upon sulfur poisoning. The formation of S-Ru/C was accompanied by a drop in methane selectivity and a strong increase in CO selectivity. The first regeneration step restored about 85% of the original catalytic activity and increased the methane selectivity back to its original value. However, as gasification continued, the conversion and methane selectivity quickly started to drop, indicative of catalyst deactivation. A second regeneration step brought the conversion back to its original value and even improved the methane selectivity of the catalyst. This gain in catalytic activity was again followed by a drop in c-t-g conversion. The methane selectivity, however, remained at a higher level than for the sulfur poisoned catalyst.

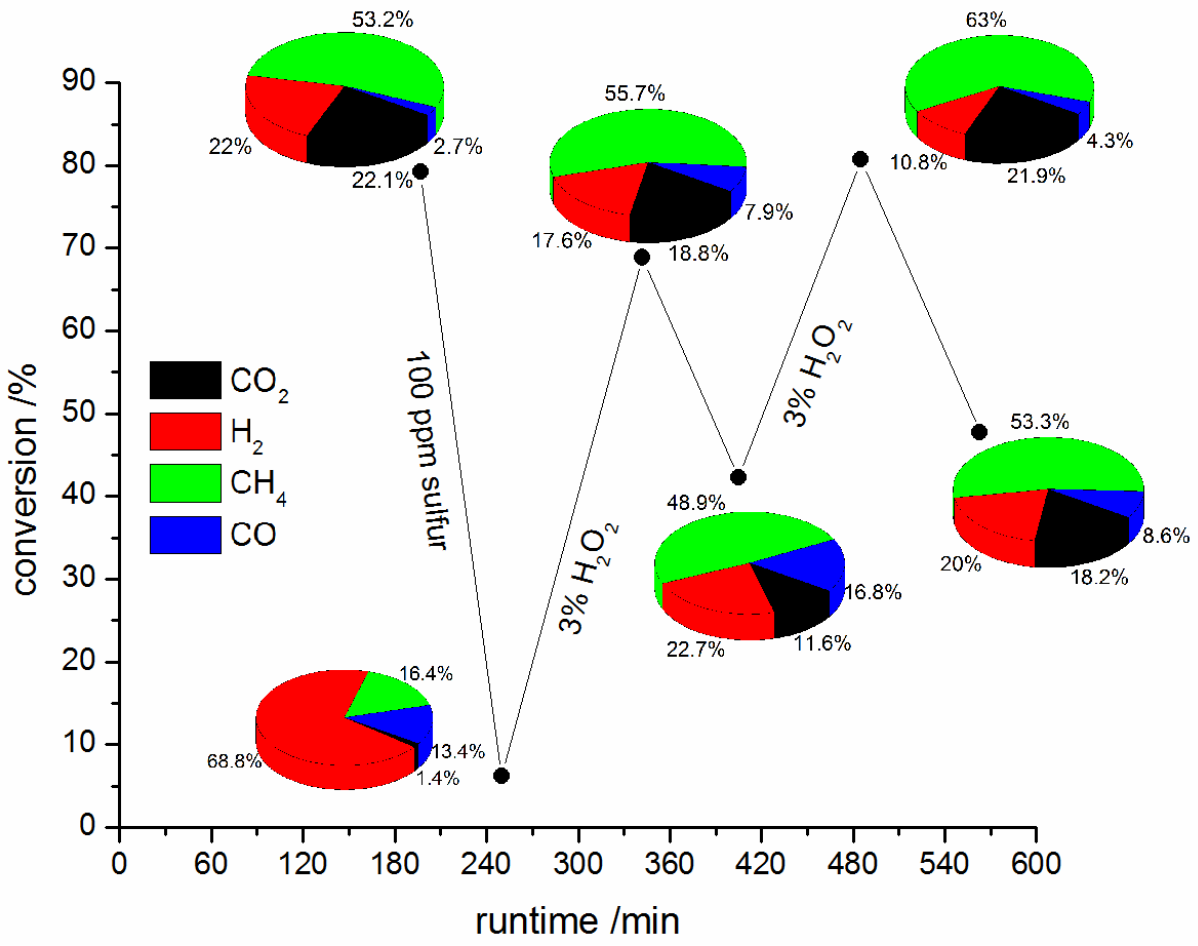

***Figure 7.6**: Carbon to gas conversion and product gas composition during gasification of 15% EtOH over Ru/C at 400°C (experiment C-19). After S-poisoning, a 2-step regeneration at 75°C was applied; to monitor the catalytic activity, EtOH was intermittently gasified for 70 min.*

To exclude sintering or leaching of the Ru particles as a potential reason for catalyst deactivation, a blank experiment was conducted in which ethanol was gasified over a fresh sample of Ru/C, followed by catalyst treatment with H_2O_2 at 75°C. The observed behavior of this catalyst sample was very different compared to S-Ru/C. The catalytic activity and the methane selectivity of the fresh catalyst were initially increased by the oxidative treatment and then leveled off to their original values within a few hours (Figure 7.7, black squares). In contrast, the regenerated catalyst (hence, after oxidative treatment of S-Ru/C) showed a significant decrease in conversion (Figure 7.7, red dots). Since the oxidative treatment of the fresh Ru/C catalyst did not lead to a drop in conversion, effects such as sintering and leaching of the active catalyst phase are unlikely to be the cause of the observed

deactivation after H_2O_2 treatment. Analysis of the reactor effluent after oxidative treatment also showed no quantifiable amount of Ru.

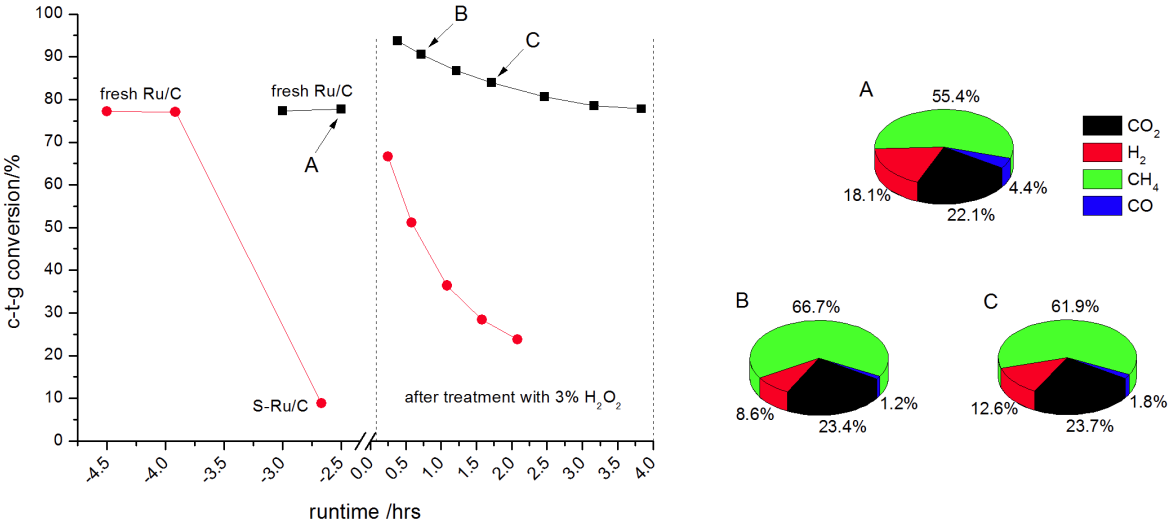

***Figure 7.7**: Carbon to gas conversion of (S-)Ru/C (-●-) and fresh Ru/C (-■-) and product gas composition for fresh Ru/C before and after treatment with H_2O_2 at 75°C. H_2O_2 treatment of the fresh catalyst sample did not lead to catalyst deactivation, whereas a S-Ru/C sample quickly deactivated again after the treatment. Gasification conditions were 15% EtOH, 390°C, 25 MPa (experiments C-20 and C-21).*

An anew sulfur poisoning of the regenerated catalyst is unlikely for two reasons. Firstly, due to the very small Ru particle size of around 1.5 nm, EXAFS is sensitive to chemisorbed sulfur on the Ru surface. However, no Ru-S bonds could be identified in the EXAFS spectra even at a runtime of two hours after regeneration (at which point catalyst deactivation is readily observed, see Figures 7.1 and 7.6). Secondly, the methane selectivity of the catalyst remains high whereas a typical effect of sulfur poisoning is a strong decrease in methane formation (Figure 7.6). Hence, sulfur poisoning does not seem to be the cause for the observed decrease in conversion.

Since Ru leaching could also be excluded via effluent analysis, minor structural changes (such as sintering) of the Ru/C catalyst after sulfur poisoning and subsequent oxidative regeneration remain as a potential reason for the observed deactivation. Whereas no deactivation (and therefore no significant particle sintering) was observed for a fresh sample of Ru/C after treatment with H_2O_2, the presence of sulfur might have an effect on the Ru

particle stability. The observed increase in activity and methane selectivity of a fresh Ru/C sample after treatment with H_2O_2 suggests that structural changes (such as redispersion or particle flatteing) might occur. In the given size range, small changes in particle size and structure can already have a great effect on catalytic activity.[147–150] However, the coordination numbers that are extracted from the EXAFS spectra typically have an error of around 10%. The error in particle size (and shape) that is calculated based on coordination numbers is even greater. For example, in the particle size range of 1.5 nm, a 10% error in coordination number can result in an error in calculated particle size of up to 20%.[125,151] The particle size and structure sensitivity of the methanation reaction is well known.[132–134] Hence, structural changes that are too small to be detected via EXAFS could be the cause of the observed decrease in conversion. Elucidating the underlying mechanisms requires further research, in particular a detailed study of Ru particle size and structure before, during and after oxidative catalyst treatment. Ideally, in-situ methods like XAS should be combined with ex-situ electron microscopy to provide a complete picture of the effect of H_2O_2 on the catalyst.

7.3.2 Coke formation and attempts at catalyst reactivation

Performance of Ru/C

Besides sulfur poisoning, coke deposition on the catalyst is another common pathway for catalyst deactivation.[152–154] Coke can be formed from (mostly unsaturated) reactants and reaction intermediates that polymerize to larger carbon structures which can then plug the pore structure of the catalyst support (fouling) or cover the surface of the active catalyst phase directly.[141,155] Highly porous catalyst supports, micro-porous supports in particular, can facilitate coke formation due to limited diffusion of reactants and reaction intermediates in the pores. As a result, reactants and reaction intermediates can polymerize before reaching the active catalyst phase, thus plugging the catalyst support, or polymerized material can cover the active catalyst phase. If the rate of polymerization of reaction intermediates is larger than the rate of conversion to product gases, the catalyst will be deactivated by coke deposition.[156] Acidic feeds are particularly prone to cause coke

formation since the evolution of unsaturated intermediates through acid catalyzed dehydration is favored under these conditions.[140]

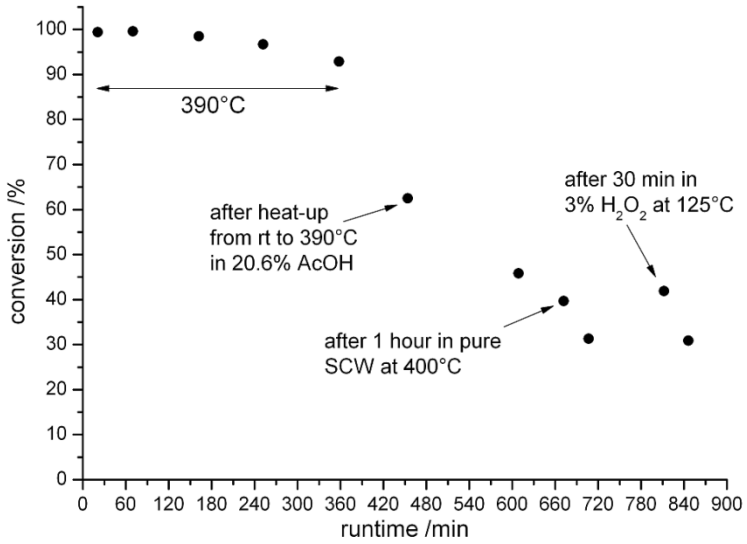

***Figure 7.9**: Conversion of 20.6% AcOH over Ru/C at 390°C (experiment C-22). Throughout a total runtime of 14 hours, reaction conditions were changed and regeneration procedures applied as outlined in the text.*

Aqueous solutions of acetic acid and citric acid were used as model feeds to cause coke formation on Ru/C catalysts and to study possible protocols for coke removal, hence catalyst regeneration. A feed of 20.6% acetic acid in water was gasified over Ru/C at 390°C with an initial conversion of 100% (Figure 7.9). After 3 hours on stream, the conversion started to decrease slowly and dropped to about 92% after 6 hours. This indicates that even full conversion will not prevent coke formation under acidic conditions. Whilst continuously feeding the acetic acid feed, the reactor was then cooled down to room temperature and heated up again to 390°C. This caused a 30% drop in catalyst activity, suggesting that coke formation is favored at subcritical conditions where ionic species and reaction mechanisms might dominate since acetic acid shows a maximum in dissociation at around 100°C in compressed water.[157] Furthermore, it is likely that the rate of coke formation under subcritical conditions is larger than the rate of gasification. During the next 3 hours on stream, a further loss in activity of about 15% was observed, leading to a conversion of only 45%. Compared to the first 6 hours of the experiment, the rate of catalyst deactivation had increased substantially, suggesting that the rate of coke formation is increased at partial

conversion. Figure 7.10 shows SEM images of a Ru/C catalyst after 14 hours of acetic acid gasification. Coke deposition in the shape of cauliflower structures and carbon spheres on the surface of the catalyst support can be readily observed. Furthermore, the BET surface area of the carbon support decreased by about 20% (Figure 7.11).

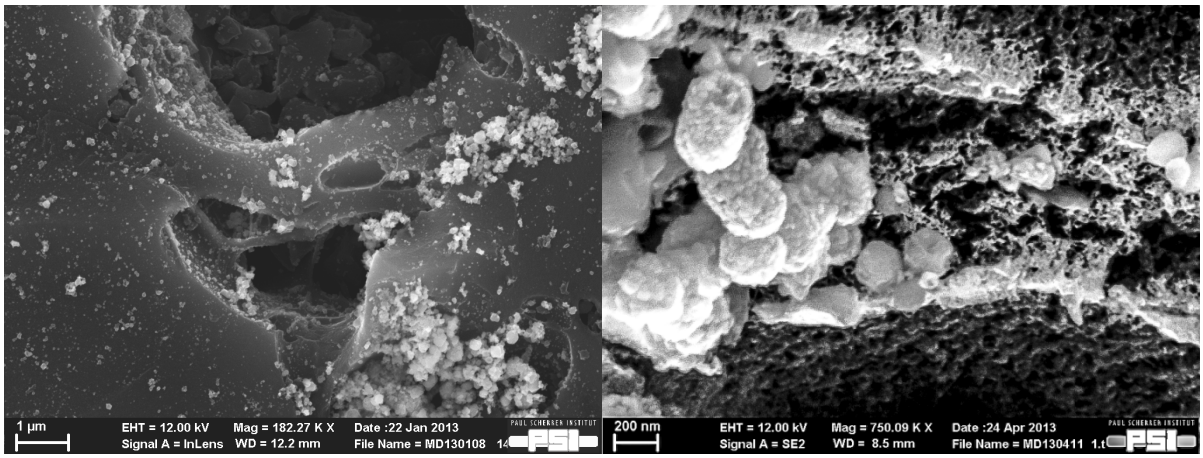

***Figure 7.10**: SEM images of Ru/C after 14 hours of acetic acid gasification. Coke formation in the form of cauliflower and spherical structures is visible.*

A reactivation of the Ru/C catalyst was attempted by exposing the catalyst to pure supercritical water at 400°C for 1 hour (Figure 7.9). This treatment was thought to facilitate the gasification of coke deposits and thus their removal from the active catalyst phase. However, no increase in catalytic activity could be observed and after another hour on stream the conversion dropped to 30%. At this point, an oxidative treatment with hydrogen peroxide, as outlined above in the case of sulfur poisoning, was applied for 30 minutes at 125°C. This led to an increase in catalytic activity by about 10%, showing that a partial reactivation of the catalyst is possible. A prolonged exposure to H_2O_2 might increase the catalytic activity further but would inevitably destroy the catalyst's carbon support in the process.

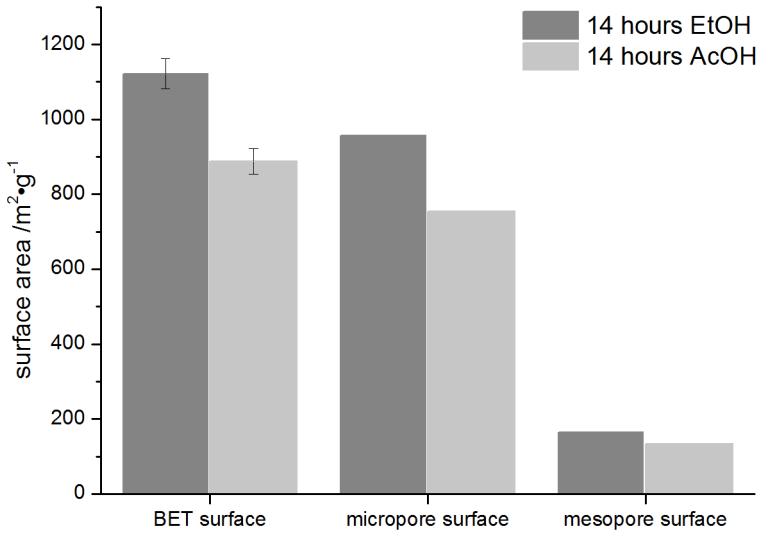

***Figure 7.11**: Comparison of BET surface area and pore structure of Ru/C after 14 hours of acetic acid and ethanol gasification, respectively.*

A procedure to remove coke deposits from catalysts, often used in petro-chemical processes, is the steam gasification with water at high temperatures and relatively low pressures.[158] In this reaction, deposited coke and tars react with water to form carbon monoxide and hydrogen and are hereby removed from the catalyst. Using this procedure, the reactivation of a Ru/C catalyst after coke deposition was attempted. In this experiment, isopropanol was first gasified over a fresh Ru/C catalyst and the feed was then switched to citric acid which quickly deactivated the catalyst (the conversion of isopropanol dropped from 75% to 8%; Figure 7.12). The deactivated catalyst was then treated with steam at 400°C and 1 MPa for 5 hours which resulted in a recovery of about 15% of catalytic activity. Given the long treatment time, the effect is rather marginal and isopropanol conversion started to drop quickly again. Furthermore, the hot steam treatment lead to corrosion of the carbon support which showed a fractured and disintegrating surface (Figure 7.13). A possible reason for this could be the self-gasification of the catalyst under these conditions (hence, the Ru particles start to gasify their own support).

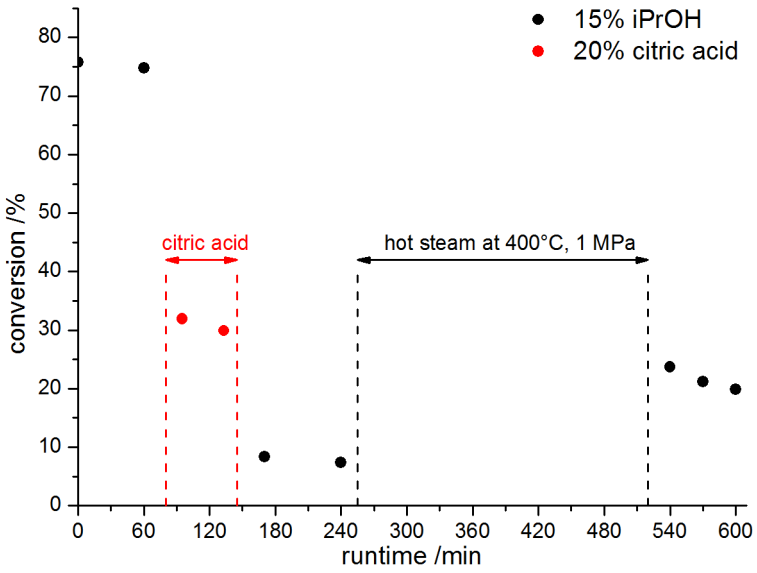

***Figure 7.12**: Conversion of isopropanol and citric acid over Ru/C at 395°C and 25 MPa (experiment C-23). After deactivating with citric acid, the catalyst was treated with hot steam for about 5 hours.*

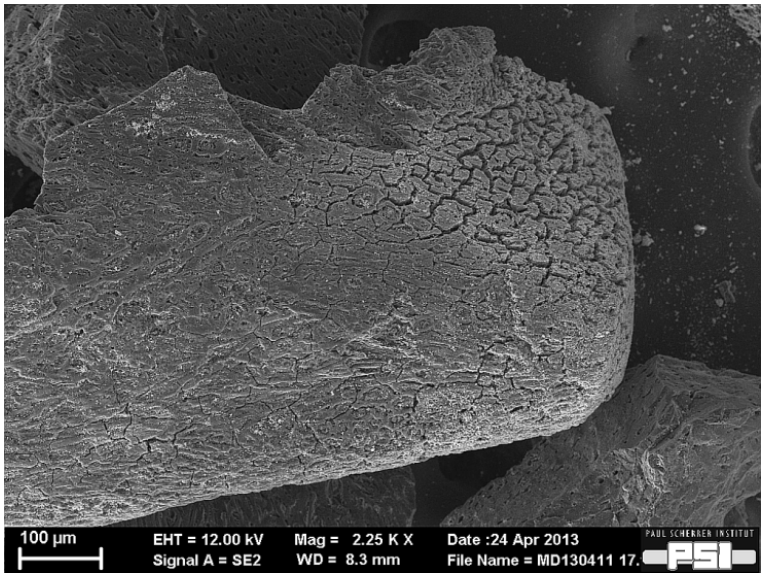

***Figure 7.13**: Ru/C catalyst particle after 5 h of treatment with steam at 400°C and 1 MPa. Fracturing of the carbon surface is well visible.*

Apart from coke formation, acidic feeds cause another severe problem, namely corrosion of the reactor walls. After 14 hours of acetic acid gasification, large amounts of a crystalline material were found on the Ru/C catalyst (Figure 7.14). The material was analyzed with energy dispersive X-ray spectroscopy (EDX) which showed oxygen, iron and nickel as the main constituents (Figure 7.15). The same material was also found in the liquid reactor

effluent. Therefore, iron and nickel are leached from the reactor walls, made of stainless steel, under acidic conditions and partially deposited on the catalyst particles as metal oxides. These metal deposits can further affect the catalyst's activity and might lead to catalyst deactivation, as reported in the case of iron.[139] More importantly, the gasification of acidic feeds under hydrothermal conditions poses a process hazard by slowly corroding and thus destabilizing the reactor walls.

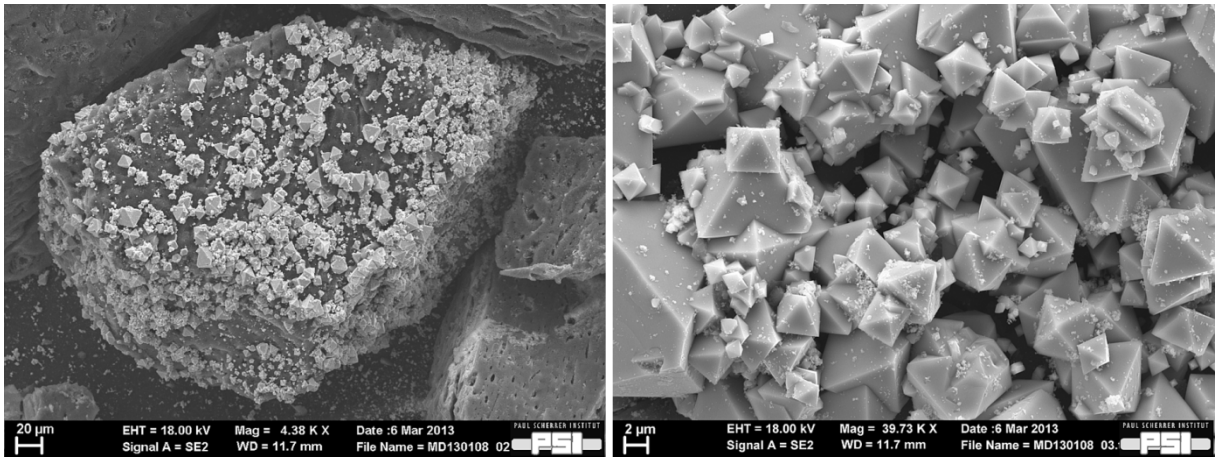

***Figure 7.14**: Crystalline corrosion products from the steel reactor walls, deposited on the Ru/C catalyst particles.*

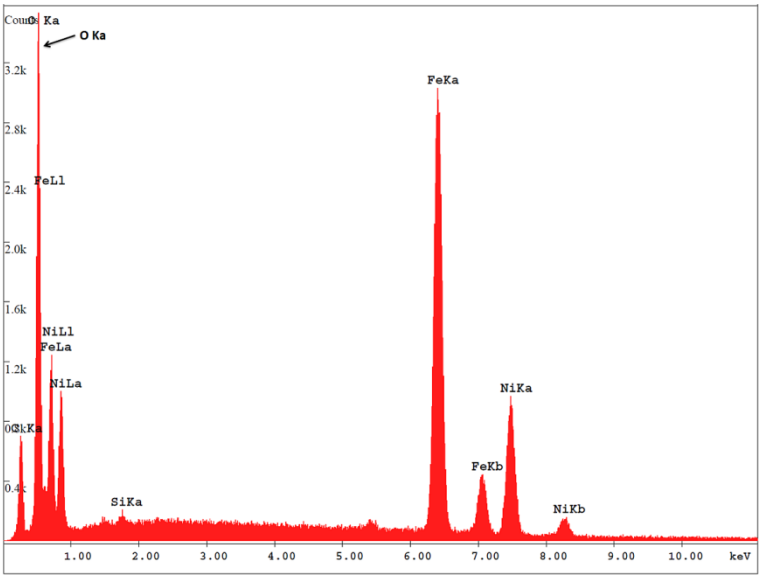

***Figure 7.15**: EDX analysis of the crystalline corrosion products shown in Figure 7.13. The analysis suggests a Fe-Ni oxide.*

Performance of a carbon nanofiber supported Ru catalyst (Ru/CNF)

As mentioned above, a possible reason for coke formation is the highly microporous structure of the carbon support which is known to lead to entrapment of reactants and intermediates inside the pores. De Vlieger et al used a platinum catalyst, supported on carbon nanofibers (CNF), for the reforming of acetic acid under hydrothermal conditions and reported that they did not observe catalyst deactivation in contrast to platinum supported on microporous carbon.[143] To study the effect of support porosity on ruthenium catalysts under SCWG reaction conditions, a Ru catalyst supported on carbon nanofibers (Ru/CNF) was prepared which present a high external surface area (90 m^2/g) without any internal pore structure (Figure 7.16).

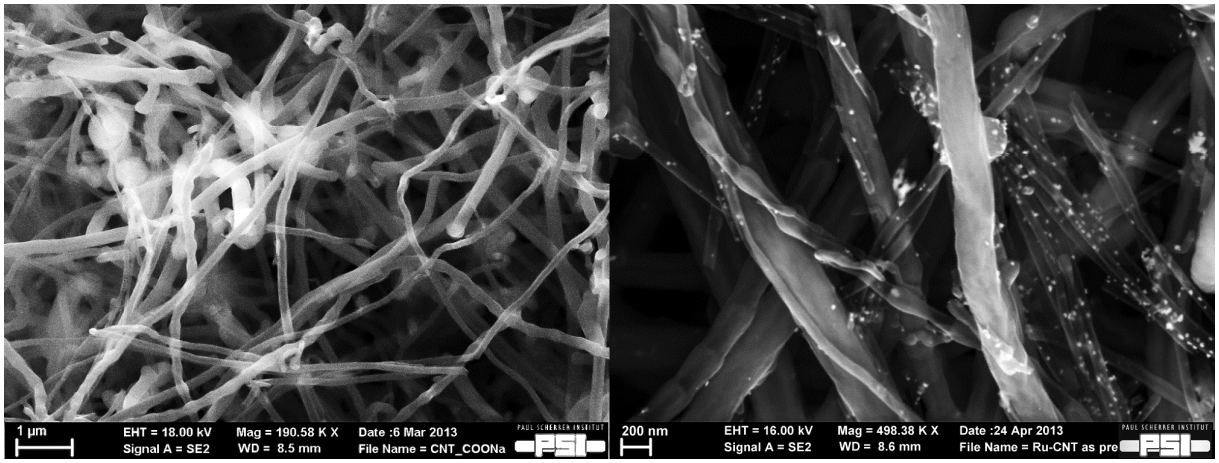

***Figure 7.16**: SEM images of carbon nano fibers: after cleaning in HCl and HNO_3 (left); after hydrothermal impregnation with $RuCl_3$ (right). Ru particles with an average size of 20-40 nm are visible as bright spots.*

An EDX analysis of the as prepared Ru/CNF catalyst, displayed in Figure 7.17, showed Ru and carbon as the only detectable components.

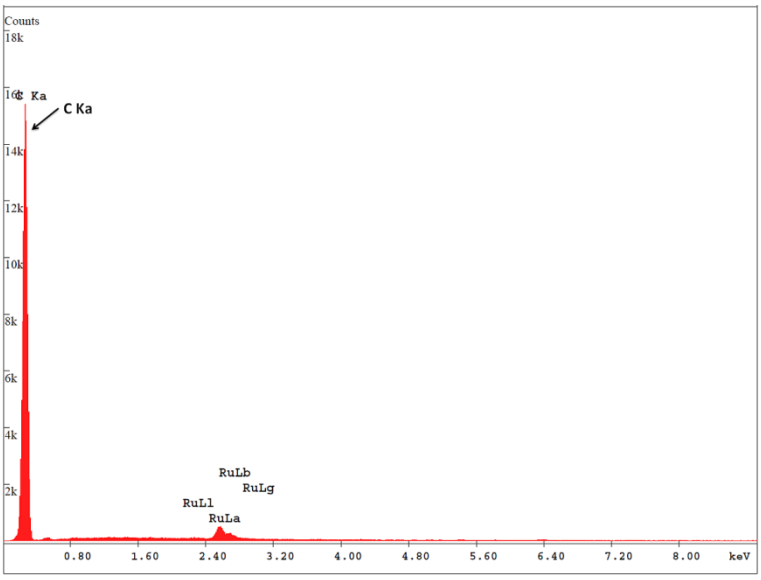

***Figure 7.16**: EDX of an as-prepared Ru/CNF catalyst. Ruthenium and carbon are the only detectable constituents.*

To test the catalyst's susceptibility to coking, the same procedure was applied as for the Ru/C catalyst. Ethanol was gasified over a fresh catalyst sample to determine its initial activity, followed by feeding citric acid as a precursor for coke formation (Figure 7.18). After exposing the catalyst to citric acid, the activity had dropped by about 50%, similar to Ru/C.

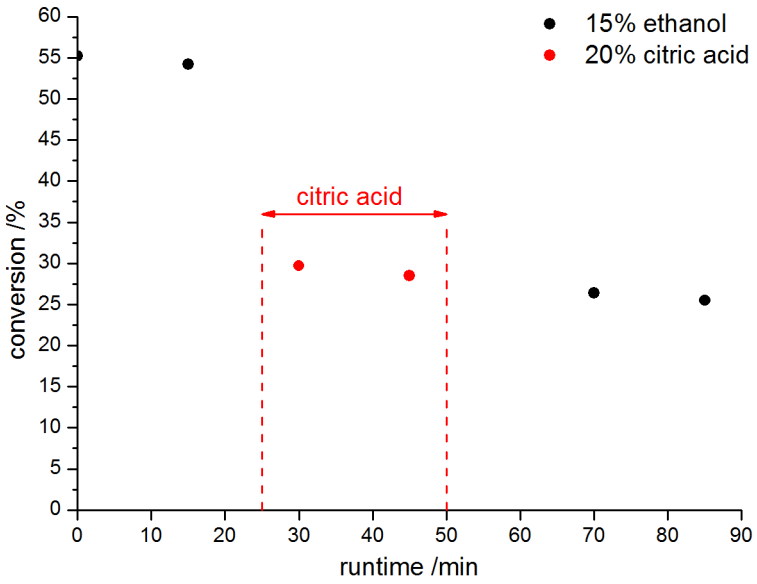

***Figure 7.18**: Gasification of ethanol and citric acid over Ru/CNF at 395°C and 25 MPa (experiment C-24). After 30 min of citric acid gasification, the catalyst had lost about 50% of its original activity.*

Electron microscopy images of Ru/CNF samples after gasification of citric acid showed that the carbon fibers are decorated with the same spherical coke structures that were already observed on Ru/C (Figure 7.19). However, the surface of the CNFs should still remain readily accessible for reactants since the coke particles do not fill up the space between the fibers completely. The large coke particles (around 500 nm in diameter) are therefore unlikely to be the main cause of catalyst deactivation. It is more likely that the Ru particles are covered by a thin layer of coke which cannot be resolved with SEM due to the lack of contrast between carbon nanofiber and the carbon deposited in the form of coke.

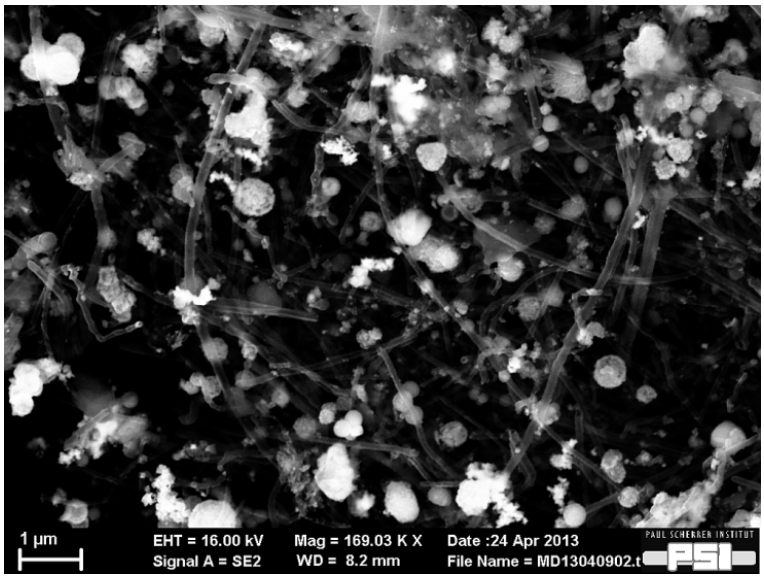

***Figure 7.19**: Coke formation on Ru/CNF after gasification of citric acid.*

In line with the results presented for the Ru/C catalyst, an EDX analysis of the spent Ru/CNF catalyst after citric acid gasification showed the presence of leached steel components (chromium, nickel and iron) on the catalyst which might also influence the catalytic activity (Figure 7.20). Overall, Ru/C and Ru/CNF behaved very similarly under acidic gasification conditions. Coke formation readily took place on both catalysts, leading to a significant drop in catalytic activity. In contrast to deactivation by sulfur poisoning, it does not seem to be possible to properly regenerate a Ru/C catalyst after coke formation and, as a consequence, conditions that lead to catalyst fouling must be avoided as much as possible (e.g. by avoiding acidic feeds and long residence times at subcritical temperatures). Furthermore, feeds

containing large amounts of organic acids can pose a significant operational hazard since they corrode steel under hydrothermal conditions.

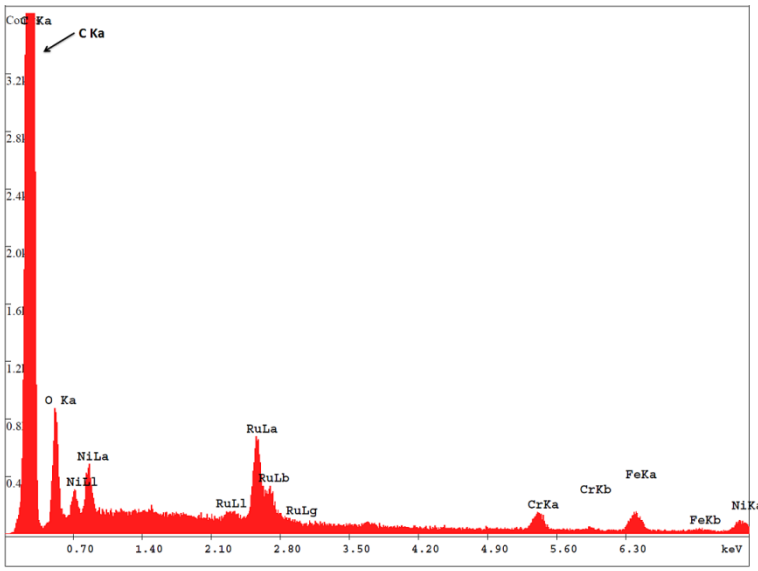

***Figure 7.20**: EDX of the Ru/CNF catalyst shown in Figure 7.18, after gasification of citric acid. Iron, nickel and chromium, which are leached from the reactor walls, can be detected on the catalyst.*

7.4 Conclusions

A protocol for the on-stream regeneration of sulfur poisoned Ru/C under hydrothermal conditions was presented. The regeneration procedure involved treating the catalyst with dilute hydrogen peroxide at low temperature and high pressure. The combined results from in-situ EXAFS and deuterium labeling of product gases during the SCWG of ethanol over Ru/C allow the conclusion that sulfur removal from sulfur-poisoned Ru/C is possible via a liquid phase, oxidative treatment. Treating the catalyst with 3% hydrogen peroxide in water at temperatures as low as 75°C was sufficient to oxidize the Ru catalyst and to remove adsorbed sulfur from the Ru surface. Under these mild conditions, the peroxide treatment did not cause corrosion of the carbon support, preserving its macro- and microstructure. After reactivation of the oxidized catalyst, the catalytic activity was similar to that of a fresh catalyst before sulfur poisoning. After the initial gain in catalytic activity post regeneration, anew deactivation of the catalyst was observed in the absence of sulfur in the feed. Sulfur poisoning and leaching of the active catalyst phase could be excluded as causes and it seems likely that structural changes of the catalyst were responsible for the deactivation. Further research, focusing on Ru particle size and structure, is necessary to shine light on these phenomena.

The coke formation on Ru catalysts was studied via SCWG of acidic feeds which cause rapid catalyst deactivation through catalyst fouling. Ru catalysts supported on micro porous carbon and non-porous carbon nanofibers, respectively, showed a similar deactivation behavior under acidic gasification conditions. Hence, the pore structure of the catalyst support does not seem to play a significant role in coke formation. Both the oxidative treatment with hydrogen peroxide and a hot steam treatment showed very limited potential for regenerating the catalyst after fouling had occurred. Furthermore, treating the Ru/C catalyst with hot steam seemed to lead to gasification of the carbon support. The presented results suggest that reaction conditions which lead to coke formation on the catalyst must be avoided by all means.

Chapter 8

A possible reaction mechanism for the gasification of EtOH on Ru/C

In this chapter, a reaction mechanism for the reaction of EtOH on a Ru surface under SCW conditions is proposed, taking into account the results from ethanol and acetaldehyde gasification over active and S-poisoned Ru/C as well as from ^{13}C and ^{2}H labeling studies (see Chapters 5, 6 and 7). Such a mechanism needs to account for the preferential formation of CO_2 from the functionalized (hence, oxygen bearing) carbon atom in ethanol, for the absence of acetaldehyde as a reaction intermediate and for the poisoning by sulfur.

To approach the formulation of this reaction mechanism, it is worthwhile to take a look into the chemistry of hydrocarbons on transition metal surfaces. Reactions like (de-) hydrogenation, C-C bond cleavage and homologation in these catalytic systems have already been studied in depth, and elementary steps have been proposed to rationalize product selectivity as well as dopant/poison effects.[159–161] Looking at the reactions of alkanes and alkenes on metal surfaces, reaction products similar to the olefin metathesis reactions have been observed. This behavior has been explained by the formation of metallacycles, and in the case of metal surfaces dimetallacyclopentane intermediates, which are formed via a γ-H activation step of surface alkyl species; it thus requires a carbon chain of at least three carbon atoms.[162] This cyclic structure is found in organometallic chemistry in transition metal complexes[163,164] but has also been proposed for the interaction of hydrocarbons on heterogeneous catalysts such as Ru/SiO_2, forming diruthenacyclopentane.[159,161,165] The dimetallacyclopentane intermediate can then decompose through retrocyclization steps via two different pathways of C-C bond cleavage, leading to different reaction products (Figure 8.1).

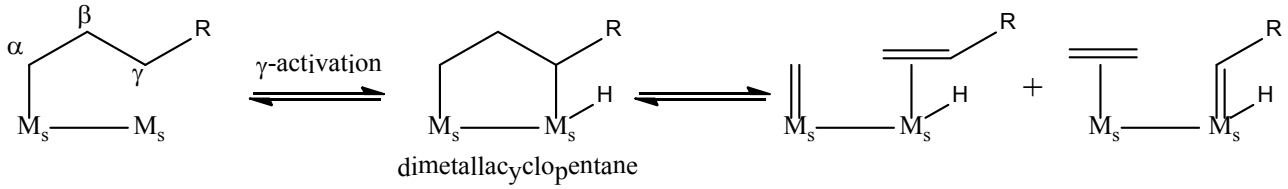

***Figure 8.1**: Formation of a dimetallacyclopentane from an alkyl adsorbate on a metal surface. Disintegration of the 5-membered ring leads to metallocarbenes and olefins.*

A similar mechanism can be proposed for the reaction between a metallic Ru surface and ethanol which contains two carbon and one oxygen in its chain. Following the adsorption of ethanol on the Ru surface and its coordination to Ru via the oxygen atom, an ethoxy species can be formed after proton transfer, as observed for many transition metals including Ni[166], Pd[167] and Pt.[168] From there, several options for further reaction with the metal surface atoms are possible (Figure 8.2); in particular, bond cleavages can be proposed involving a β-H transfer step (pathway A) or γ-H activation (pathway B). The β-H transfer would lead to the formation of coordinated acetaldehyde as a key reaction intermediate. However, it was shown in Chapter 6.3.2 that reforming of acetaldehyde does not lead to the same product as ethanol, and it is thus probably not an intermediate in ethanol reforming according to the principle of microscopic reversibility, making pathway A unlikely.

Since the preferential formation of $^{13}CO_2$ from the $^{13}CH_2$-OH carbon atom was observed, an early cleavage of the C-O bond in the ethanol molecule is also unlikely. Instead, the formation of a dimetallacycle that involves two adjacent Ru surface atoms is possible via a γ-H activation of the chemisorbed ethoxy species (pathway B). This cyclic structure can then decompose in two ways via a retrocyclization mechanism.

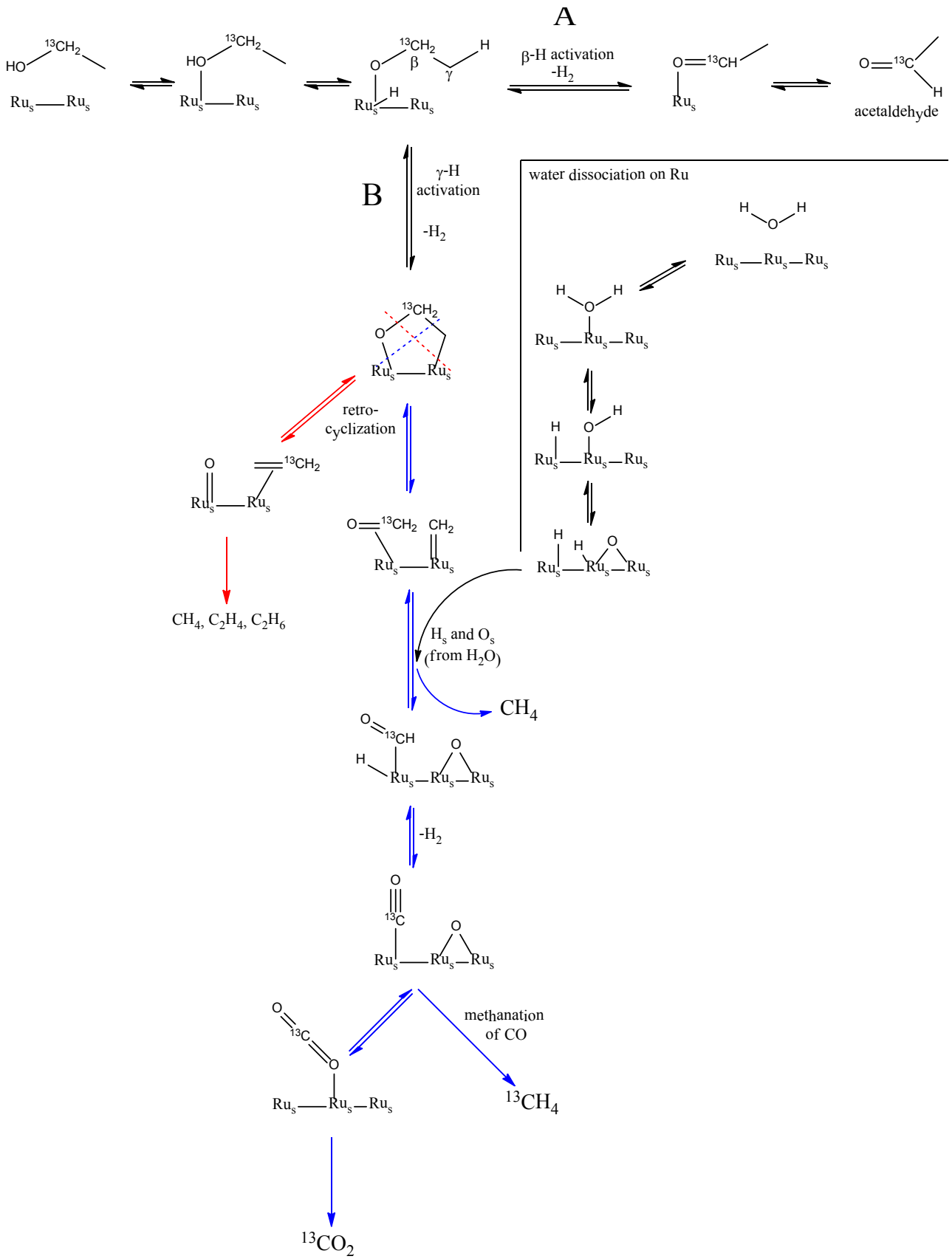

Figure 8.2: Possible reactions of ethanol on Ru/C. The pathway that is compatible with the experimental results is shown in blue.

A first option is a cleavage of the C-O and M-C bonds, yielding an oxygen adatom and coordinated ethylene (red pathway). The latter can desorb from the surface as ethylene or ethane upon further hydrogenation or be further hydrogenolyzed into methane. However, since no significant amounts of C_2 hydrocarbons were found in the product gas from ethanol gasification, it can only be a minor reaction pathway. Furthermore, an oxidation of these C_2 species by surface bound oxygen to form CO_2 would proceed in an unbiased manner, meaning that ^{12}C and ^{13}C would form CO_2 in equal amounts when using 1-carbon-13 labeled ethanol. This is not supported by the experimental results which show that CO_2 is preferentially formed from the labeled carbon.

The second option is the cleavage of the C-C bond to form coordinated formaldehyde and a metallocarbene (Figure 8.2, blue pathway). The metallocarbene is likely to be further dehydrogenated to carbyne and carbide species (as predicted by calculations; see Chapter 5), but is eventually hydrogenated by surface-bound hydrogen (resulting from the dissociative chemisorption of water on Ru) to form ^{12}C-methane. The formaldehyde can be further dehydrogenated to a ^{13}C carbonyl species which then reacts either with an oxygen adatom (arising from the dissociation of water) to form $^{13}CO_2$ or with surface-bound hydrogen to form $^{13}CH_4$ and H_2O (methanation). This mechanism accounts for the preferential formation of ^{13}C-labeled CO_2 (and in turn for the formation of mainly ^{12}C methane with minor amounts of ^{13}C) and does not require acetaldehyde as a reaction intermediate. Since the hydrogen necessary for the methanation is mainly derived from water, high amounts of deuterated methane can be expected when the reaction is performed in D_2O, which is also in good agreement with the experimental findings.

Note that the formation of the dimetallacyclopentane intermediate requires the presence of metal ensembles of the catalyst surface since adjacent metal atoms are involved in the formation and cleavage of the carbon-carbon bonds. In fact, for the corresponding reaction with hydrocarbons, it has been shown that Pt surfaces readily transform isobutane into its lower homologues, probably via the decomposition of the same type of dimetallacyclopentane intermediate, which leads to lower homologues: CH_4, C_2H_6 and C_3H_8, making Pt an excellent cracking catalyst.[169,170] On the other hand, $PtSn_3$ is highly selective towards isobutane to isobutene dehydrogenation (Figure 8.3), which has been rationalized as a positive effect of site isolation.

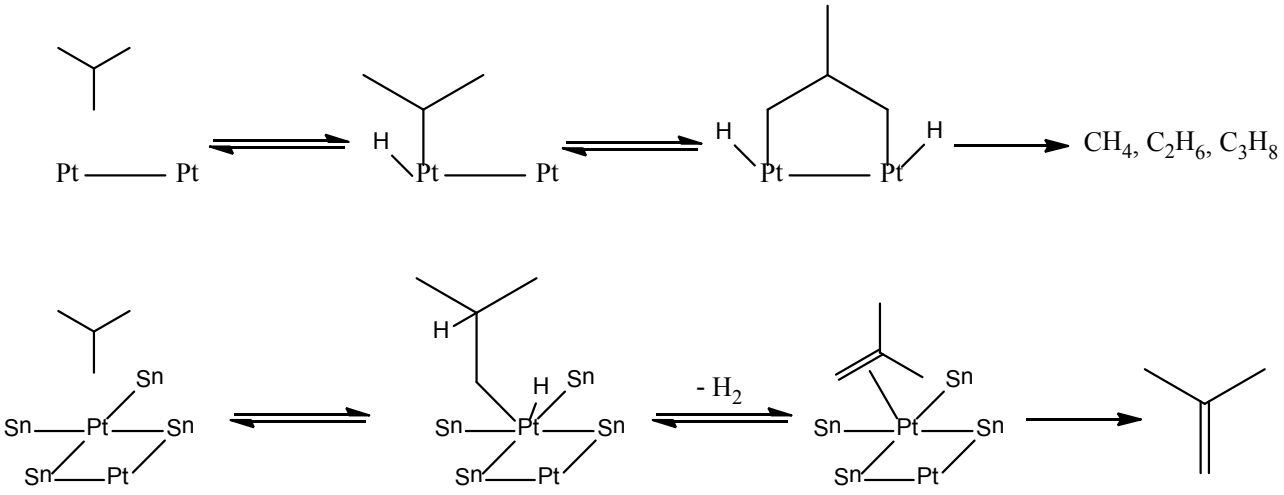

***Figure 8.3**: Effect of site isolation on Pt. On a clean Pt surface, a dimetallacyclopentane is readily formed and isobutane is cracked into smaller hydrocarbons (top). On $PtSn_3$, the now isolated Pt atoms only catalyze the dehydrogenation of isobutane, forming isobutene with high selectivity (bottom).*

In fact, dehydrogenation probably occurs on a single Pt atom instead of an ensemble and is possible on Pt-Sn surfaces (site isolation effect), while cracking requires several adjacent Pt atoms. Similar observations were made for sulfur poisoned metal surfaces, including Ru.[171] Again, sulfur poisoning diminished the number of metal atom ensembles and thus decreased the C-C bond cleavage activity of the catalysts. This site isolation effect, upon sulfur poisoning, observed in our sample by EXAFS, probably explains the loss of activity towards reforming of ethanol over S-Ru/C. Site isolation on the Ru surface upon sulfur poisoning would shut down C-C bond cleavage, which requires adjacent metal atoms, and thereby the methane yield, while maintaining beta-hydrogen transfer and thereby the high hydrogen yield (due to the dehydrogenation reaction). Removal of the adsorbed sulfur via oxidative regeneration of the Ru catalyst then restores the metal ensembles and therefore the catalytic activity for C-C bond cleavage and methanation.

In order to increase the sulfur resistance of Ru catalysts, site isolation due to sulfur adsorption must be avoided. In an improved catalyst, metal ensembles that catalyze C-C bond cleavage and methanation have to be preserved in the presence of sulfur. Ru-S bonds show a medium bond strength compared to other transition metals.[172] An alloy of Ru with a metal that forms stronger metal–sulfur bonds (such as Re, Mo or W) might help to protect Ru against sulfur poisoning. The ratio of the metals would have to be chosen in such a way

that the size of Ru ensembles (hence, neighboring Ru atoms) on the catalyst surface is large enough to still catalyze the decomposition of organic compounds. Besides its role as a sulfur scavenger, the alloyed metal would also change the electronic structure of Ru and therefore probably the Ru-S bond strength. This might in fact be the larger potential of such alloyed or doped Ru catalysts. Norskov et al. performed a computational screening of methanation catalysts, including many bimetallic systems.[173] They showed that Ni-Fe alloys show very different activity for CO dissociation (and therefore activity for methanation), depending on the Ni-Fe ratio. Such a study should be performed for Ru-M alloys regarding their methanation activity and metal-sulfur bond strength to find catalytic systems that show both sufficient activity for C-C bond breaking and methanation and resistance to sulfur poisoning.

Although the proposed mechanism cannot be demonstrated without further experimental and spectroscopic input (e.g. in situ infrared and Raman spectroscopy to directly detect the organic surface intermediates), it allows the rationalization of the results presented in the previous chapters and is thus a possible reaction pathway for the SCWG of ethanol on Ru/C.

Chapter 9

Conclusions and recommendations for further research

9.1 Conclusions

This thesis provides mechanistic insights into the conversion of organic compounds to methane on Ru catalysts in supercritical water (chapters 5 to 7) as well as advancements in experimental infrastructure and methodology to study mechanisms of reactions taking place in supercritical water (chapters 3 to 5). Finally, it provides a knowledge-based, mild regeneration mechanism for a sulfur poisoned Ru catalyst that can be applied in situ (Chapter 7). The acquired knowledge has the potential to make SCW gasification processes more efficient and to further inspire mechanistic studies in the field of supercritical water catalysis.

Chapter 3 critically reviewed the first in-situ XAS study on the hydrothermal gasification of ethanol and the mechanistic insights that were derived thereof. By constructing a similar setup but with different orientation of integral parts such as valves and pipes, it was shown that the supposedly oscillating gasification reaction which was partly the basis for the proposed reaction mechanism was a system-inherent artifact that was caused by the slug flow of gas in liquid in the reactor effluent. However, the validity of the in situ XAS results that show metallic Ru to be the active catalyst persists. Although the slug flow could not be avoided entirely, a versatile setup for gasification experiments in supercritical water was designed that limits the fluctuations in product gas release from the setup and allows for quick experimentation.

This setup was used both for bench-top operation in the laboratory as well as for in-situ XAS studies at a dedicated XAS beamline. An X-ray transparent reactor made from aluminum nitride ceramic was designed to conduct in-situ EXAFS measurements during the gasification of organic model compounds over Ru/C catalysts in supercritical water (Chapter 4). This

resulted in the first EXAFS analysis of a working, heterogeneous catalyst under these conditions which allowed for determination of particle size, oxidation state and structure under various operando conditions, such as gasification, sulfur poisoning or catalyst regeneration (chapters 6 and 7).

Complementarily to in-situ EXAFS as a structural probe, a concept for a direct chemical probe was developed which detects adsorbed species on the catalyst surface (chapters 5 and 6). Isotope labeling of product gases with deuterium as well as of reactants with ^{13}C was used under SCW conditions to study the nature and abundance of hydrocarbon adsorbates on the catalyst surface as well as the catalyst's ability to break C-H, C-C and C-O bonds.

By applying in situ XAS combined with isotope studies it was concluded that the methanation reaction on the active catalyst proceeds via complete degradation of the organic compounds in the feed to CH_x adsorbates on the Ru surface which are then re-hydrogenated by mainly water derived hydrogen to form methane (chapters 5 and 6). Sulfur poisoning of the catalyst was found to proceed via irreversible adsorption of sulfide species on the Ru surface. This changed the amount and distribution of CH_x adsorbates and therefore the activity and selectivity of the methanation reaction. Furthermore, the bond breaking ability of the catalyst for C-H, C-C and C-O strongly decreased upon sulfur poisoning (chapter 6).

Removal of the adsorbed sulfur, hence catalyst regeneration, was realized by treating the sulfur poisoned catalyst with dilute hydrogen peroxide at mild conditions (chapter 7). Based on combined data from in situ XAS and ex situ electron microscopy, a knowledge based regeneration protocol at very mild conditions was developed. In situ EXAFS showed that the Ru particles were quickly oxidized to RuO_2 upon contact with H_2O_2. After this oxidation step, the catalyst could be reduced and therefore reactivated again. Both EXAFS analysis and isotope labeling experiments showed that sulfur was successfully removed from the catalyst surface through this oxidative treatment. Optimization of the process parameters resulted in a regeneration protocol that efficiently removes sulfur from the catalyst whilst keeping the catalyst support intact. After catalyst regeneration, an anew partial deactivation was observed. The reasons for this phenomenon remain unclear at this point. Minute changes in Ru particle size and structure, induced by sulfur poisoning and subsequent H_2O_2 treatment,

that lead to partial catalyst deactivation might the underlying cause. Investigation of these effects requires further research, as outlined in section 8.2.

The formation of coke due to acidic feeds, another pathway of catalyst deactivation, was studied using Ru catalysts with highly porous and non-porous carbon supports (chapter 7). The results showed that the porosity of the support does not have a significant influence on catalyst deactivation under these conditions. Coke deposition readily occurred on both catalyst types and could not be remedied. Attempts at catalyst regeneration using hydrogen peroxide and superheated steam, respectively, not only failed at reactivating the catalysts but lead to corrosion of the carbon support. Therefore, process conditions for catalytic SCWG need to be tuned in such a way that coke formation on the catalyst is prevented as much as possible.

Finally, the results from in situ EXAFS, product gas analysis and isotope labeling were combined to propose a reaction mechanism for the decomposition and gasification of ethanol on a Ru surface under hydrothermal conditions (Chapter 9). This mechanism is based on well established reactions of hydrocarbons on metal surfaces and helps to explain the observed product gas selectivities of the active and S-poisoned Ru catalyst.

9.2 Recommendations for further research

The interaction between hydrogen peroxide and the sulfur species adsorbed on the poisoned Ru catalyst needs to be studied in more detail. It remains unclear which sulfur species are formed from the adsorbed sulfide upon contact with H_2O_2. The chemistry, water solubility and interaction with the carbon support of these oxidized sulfur compounds will probably depend on the reaction temperature. This knowledge can help to further optimize the regeneration procedure and enhance the understanding of sulfur mobility on catalysts under SCW conditions. However, in-situ studies are not straightforward since the photon energy required for in-situ XAS at the sulfur K-edge is too low to penetrate reactors that are able to operate under SCW conditions. Hence, a combination of in-situ XAS at the Ru K-edge and ex-situ XAS at the sulfur K-edge (along with complementary ex situ methods such as IR and Raman spectroscopy) will be necessary to study the evolution of (oxidized) sulfur species

from the adsorbed sulfide upon contact with hydrogen peroxide and during heat-up after the oxidative treatment.

The focus of further investigations into catalyst regeneration, however, should be the observed catalyst deactivation that occurs after the oxidative treatment and subsequent reactivation. As proposed in chapter 7, changes in particle size and structure might be the reason for this phenomenon. An in situ XAS study involving many regeneration cycles might show a trend in particle size evolution that is induced by the oxidative treatment. To enhance the sensitivity of the method, the difference file technique can be used. Since Ru/C samples that have been poisoned by sulfur and samples that have never been in contact with sulfur show a different behavior after oxidative treatment, such a study should include both scenarios to elucidate the role of sulfur on Ru particle size and structure. Ideally, in-situ studies are combined with ex-situ electron microscopy to back up the obtained results.

A regeneration protocol that is able to provide complete and lasting catalyst regeneration will substantially improve the efficiency of the SCWG process by mitigating one of its major obstacles which is catalyst deactivation. However, catalyst regeneration does not offer one single solution to this challenge but needs to be a part of several process improvements, including an efficient salt separation from the hydrothermal biomass feed, prevention of coke formation and the development of sulfur absorbers that are able to remove sulfur from the hydrothermal feed. Each of these tasks is challenging enough in itself but well worth the effort as a process that converts currently un-exploitable types of biomass into a convenient fuel is within reach.

References

1. Vogel, F. in *Handb. Green Chem. Vol.* **2,** 281–324 (Wiley-VCH, 2009).

2. Kruse, A., Funke, A. & Titirici, M.-M. Hydrothermal conversion of biomass to fuels and energetic materials. *Curr. Opin. Chem. Biol.* **17,** 515–521 (2013).

3. Peterson, A. *et al.* Thermochemical biofuel production in hydrothermal media: A review of sub- and supercritical water technologies. *Energy Environ. Sci.* **1,** 32 (2008).

4. Kruse, A. Supercritical water gasification. *Biofuels, Bioprod. Biorefining* **2,** 415–437 (2008).

5. Elliott, D. C. Catalytic hydrothermal gasification of biomass. *Biofuels, Bioprod. Biorefining* **2,** 254–265 (2008).

6. Kruse, A. & Dinjus, E. Hot compressed water as reaction medium and reactant: Properties and synthesis reactions. *J. Supercrit. Fluids* **39,** 362–380 (2007).

7. Kruse, A. & Dinjus, E. Hot compressed water as reaction medium and reactant: Degradation reactions. *J. Supercrit. Fluids* **41,** 361–379 (2007).

8. Guo, Y. *et al.* Review of catalytic supercritical water gasification for hydrogen production from biomass. *Renew. Sustain. Energy Rev.* **14,** 334–343 (2010).

9. Matsumura, Y. *et al.* Biomass gasification in near- and super-critical water: Status and prospects. *Biomass and Bioenergy* **29,** 269–292 (2005).

10. Shen, Z., Jin, F., Zhang, Y. & Wu, B. Effect of alkaline catalysts on hydrothermal conversion of glycerin into lactic acid. *Ind. Eng. Chem. Res.* **48,** 8920–8925 (2009).

11. Ott, L., Bicker, M. & Vogel, H. Catalytic dehydration of glycerol in sub- and supercritical water: a new chemical process for acrolein production. *Green Chem.* **8,** 214 (2006).

12. Lehr, V., Sarlea, M., Ott, L. & Vogel, H. Catalytic dehydration of biomass-derived polyols in sub- and supercritical water. *Catal. Today* **121,** 121–129 (2007).

13. King, J., Holliday, R. & List, G. Hydrolysis of soybean oil in a subcritical water flow reactor. *Green Chem.* **1,** 261–264 (1999).

14. Watanabe, M., Iida, T. & Inomata, H. Decomposition of a long chain saturated fatty acid with some additives in hot compressed water. *Energy Convers. Manag.* **47,** 3344–3350 (2006).

15. Onwudili, J. A. & Williams, P. T. Hydrothermal reforming of bio-diesel plant waste: Products distribution and characterization. *Fuel* **89,** 501–509 (2010).

16. Duan, P. & Savage, P. E. Hydrothermal Liquefaction of a Microalga with Heterogeneous Catalysts. *Ind. Eng. Chem. Res.* **50,** 52–61 (2011).

17. Biller, P. & Ross, A. B. Potential yields and properties of oil from the hydrothermal liquefaction of microalgae with different biochemical content. *Bioresour. Technol.* **102,** 215–25 (2011).

18. Yamaguchi, A. *et al.* Hydrogen production from woody biomass over supported metal catalysts in supercritical water. *Catal. Today* **146,** 192–195 (2009).

19. Waldner, M. H. Catalytic hydrothermal gasification of biomass for the production of synthetic natural gas. *PhD Thesis 17100* **ETH Zürich,** (2007).

20. Kruse, A. Hydrothermal biomass gasification. *J. Supercrit. Fluids* **47,** 391–399 (2009).

21. Kim, K., Son, S. H., Kim, K., Kim, K. & Kim, Y.-C. Environmental effects of supercritical water oxidation (SCWO) process for treating transformer oil contaminated with polychlorinated biphenyls (PCBs). *Chem. Eng. J.* **165,** 170–174 (2010).

22. Kritzer, P. & Dinjus, E. An assessment of supercritical water oxidation (SCWO): existing problems, possible solutions and new reactor concepts. *Chem. Eng. J.* **83,** 207–214 (2001).

23. Schubert, M. Catalytic hydrothermal gasification of biomass - salt recovery and continuous gasification of glycerol solutions. *PhD Thesis 19039* **ETH Zürich,** (2010).

24. Lemmon, E., McLinden, M. & Friend, D. NIST Chemistry Webbook, NIST Standard Reference Database Number 69, Thermophysical Properties of Fluid Systems, National Institute of Standards and Technology, Gaithersburg, MD, USA. (2012). at <http://webbook.nist.gov>

25. Fernandez, D., Goodwin, A., Lemmon, E., Sengers, J. & Williams, R. A formulation for the static permittivity of water and steam at temperatures from 238 K to 873 K at pressures up to 1200 MPa, including derivatives and Debye–Hückel coefficients. *J. Phys. Chem. Ref. Data* **26,** 1125 (1997).

26. Bandura, A. V. The Ionization Constant of Water over Wide Ranges of Temperature and Density. *J. Phys. Chem. Ref. Data* **35,** 15 (2006).

27. Weingärtner, H. & Franck, E. U. Supercritical water as a solvent. *Angew. Chemie (International Ed.)* **44,** 2672–92 (2005).

28. Morimoto, M., Sato, S. & Takanohashi, T. Conditions of supercritical water for good miscibility with heavy oils. *J. Japan Pet. Inst.* **53,** 61–62 (2010).

29. Schubert, M., Regler, J. W. & Vogel, F. Continuous salt precipitation and separation from supercritical water. Part 1: Type 1 salts. *J. Supercrit. Fluids* **52,** 99–112 (2010).

30. Kuhlmann, B., Arnett, E. M. & Siskin, M. Classical Organic Reactions in Pure Superheated Water. *J. Org. Chem.* **59,** 3098–3101 (1994).

31. Bühler, W., Dinjus, E., Ederer, H., Kruse, A. & Mas, C. Ionic reactions and pyrolysis of glycerol as competing reaction pathways in near-and supercritical water. *J. Supercrit. Fluids* **22,** 37–53 (2002).

32. Antal, M., Mok, W., Roy, J. & Raissi, A. Pyrolytic sources of hydrocarbons from biomass. *J. Anal. Appl. Pyrolysis* **8,** 291–303 (1985).

33. Voll, F. A. P. *et al.* Thermodynamic analysis of supercritical water gasification of methanol, ethanol, glycerol, glucose and cellulose. *Int. J. Hydrogen Energy* **34,** 9737–9744 (2009).

34. Lu, Y., Guo, L., Zhang, X. & Yan, Q. Thermodynamic modeling and analysis of biomass gasification for hydrogen production in supercritical water. *Chem. Eng. J.* **131,** 233–244 (2007).

35. Sharma, A., Nakagawa, H. & Miura, K. A novel nickel/carbon catalyst for CH and H production from organic compounds dissolved in wastewater by catalytic hydrothermal gasification. *Fuel* **85,** 179–184 (2006).

36. Vogel, F., Waldner, M. H., Rouff, A. & Rabe, S. Synthetic natural gas from biomass by catalytic conversion in supercritical water. *Green Chem.* **9,** 616 (2007).

37. Elliott, D., Hart, T. R. & Neuenschwander, G. G. Chemical processing in high-pressure aqueous environments. 8. Improved catalysts for hydrothermal gasification. *Ind. Eng. Chem. Res.* **45,** 3776–3781 (2006).

38. Kowalczyk, Z. *et al.* Carbon-supported ruthenium catalyst for the synthesis of ammonia. The effect of the carbon support and barium promoter on the performance. *Appl. Catal. A Gen.* **184,** 95–102 (1999).

39. Zöhrer, H., Schubert, M. & Vogel, F. Regeneration Methods for Sulfur-Poisoned Catalysts in Supercritical Water Gasification. *Chemie Ing. Tech.* **84,** 1305 (2012).

40. Zöhrer, H., Mayr, F. & Vogel, F. Stability and performance of ruthenium catalysts based on refractory oxide supports in supercritical water conditions. *Energy & Fuels* **27,** 4739–4747 (2013).

41. Osada, M., Sato, O., Arai, K. & Shirai, M. Stability of supported ruthenium catalysts for lignin gasification in supercritical water. *Energy & fuels* **20,** 2337–2343 (2006).

42. Yamaguchi, A., Hiyoshi, N., Sato, O., Osada, M. & Shirai, M. Lignin Gasification over Supported Ruthenium Trivalent Salts in Supercritical Water. *Energy & Fuels* **22,** 1485–1492 (2008).

43. Park, K. C. & Tomiyasu, H. Gasification reaction of organic compounds catalyzed by RuO2 in supercritical water. *Chem. Commun.* 694–5 (2003).

44. Ketchie, W., Maris, E. & Davis, R. In-situ X-ray absorption spectroscopy of supported Ru catalysts in the aqueous phase. *Chem. Mater.* **19,** 3406–3411 (2007).

45. Yamaguchi, A., Hiyoshi, N., Sato, O., Osada, M. & Shirai, M. EXAFS Study on Structural Change of Charcoal-supported Ruthenium Catalysts during Lignin Gasification in Supercritical Water. *Catal. Letters* **122,** 188–195 (2007).

46. Rabe, S., Nachtegaal, M., Ulrich, T. & Vogel, F. Towards understanding the catalytic reforming of biomass in supercritical water. *Angew. Chemie (International Ed.)* **49,** 6434–7 (2010).

47. Kudo, K. & Komatsu, K. Reduction of alkali metal carbonate to methane with water in the presence of Raney alloy. *J. Mol. Catal. A Chem.* **145,** 159–167 (1999).

48. Kudo, K. & Komatsu, K. Selective formation of methane in reduction of CO2 with water by Raney alloy catalyst. *J. Mol. Catal. A Chem.* **145,** 257–264 (1999).

49. Rostrup-Nielsen, J. *Steam reforming catalysts: an investigation of catalysts for tubular steam reforming of hydrocarbons*. (Teknisk Forlag, 1975).

50. Waldner, M., Krumeich, F. & Vogel, F. Synthetic natural gas by hydrothermal gasification of biomass. Selection procedure towards a stable catalyst and its sodium sulfate tolerance. *J. Supercrit. Fluids* **43,** 91–105 (2007).

51. Osada, M., Hiyoshi, N., Sato, O., Arai, K. & Shirai, M. Reaction pathway for catalytic gasification of lignin in presence of sulfur in supercritical water. *Energy & Fuels* **21,** 1854–1858 (2007).

52. Osada, M., Hiyoshi, N., Sato, O., Arai, K. & Shirai, M. Effect of sulfur on catalytic gasification of lignin in supercritical water. *Energy & Fuels* **21,** 1400–1405 (2007).

53. Elliott, D. C. *et al.* Effects of trace contaminants on catalytic processing of biomass-derived feedstocks. *Appl. Biochem. Biotechnol.* **113-116,** 807–825 (2004).

54. Osada, M., Hiyoshi, N., Sato, O., Arai, K. & Shirai, M. Subcritical water regeneration of supported ruthenium catalyst poisoned by sulfur. *Energy & Fuels* **22,** 845–849 (2008).

55. Rostrup-Nielsen, J. Some principles relating to the regeneration of sulfur-poisoned nickel catalyst. *J. Catal.* **21,** 171–178 (1971).

56. Solunke, R. D. & Veser, G. Integrating desulfurization with CO2-capture in chemical-looping combustion. *Fuel* **90,** 608–617 (2011).

57. Cheah, S., Olstad, J. L., Jablonski, W. S. & Magrini-Bair, K. A. Regenerable Manganese-Based Sorbent for Cleanup of Simulated Biomass-Derived Syngas. *Energy & Fuels* **25,** 379–387 (2011).

58. König, C. F. J., Schildhauer, T. J. & Nachtegaal, M. Methane synthesis and sulfur removal over a Ru catalyst probed in situ with high sensitivity X-ray absorption spectroscopy. *J. Catal.* **305,** 92–100 (2013).

59. Fitzharris, W., Katzer, J. & Manogue, W. Sulfur deactivation of nickel methanation catalysts. *J. Catal.* **76,** 369–384 (1982).

60. Agrawal, P., Katzer, J. & Manogue, W. Methanation over Transition-Metal Catalysts. *J. Catal.* **74,** 332–342 (1982).

61. Betta, R. D., Piken, A. & Shelef, M. Heterogeneous methanation: Steady-state rate of CO hydrogenation on supported ruthenium, nickel and rhenium. *J. Catal.* **40,** 173–183 (1975).

62. Rangan, M., Yung, M. M. & Medlin, J. W. Experimental and computational investigations of sulfur-resistant bimetallic catalysts for reforming of biomass gasification products. *J. Catal.* **282,** 249–257 (2011).

63. Borg, Ø. *et al.* Effect of biomass-derived synthesis gas impurity elements on cobalt Fischer–Tropsch catalyst performance including in situ sulphur and nitrogen addition. *J. Catal.* **279,** 163–173 (2011).

64. Ogletree, D. *et al.* A differentially pumped electrostatic lens system for photoemission studies in the millibar range. *Rev. Sci. Instrum.* **73,** 3872–3877 (2002).

65. Bluhm, H. & Hävecker, M. Methanol oxidation on a copper catalyst investigated using in situ X-ray photoelectron spectroscopy. *J. Phys. Chem. B* **108,** 14340–14347 (2004).

66. Grass, M. E. *et al.* A reactive oxide overlayer on rhodium nanoparticles during CO oxidation and its size dependence studied by in situ ambient-

pressure X-ray photoelectron spectroscopy. *Angew. Chemie (International Ed.)* **47,** 8893–6 (2008).

67. Scherrer, P. Bestimmung der Grösse und der inneren Struktur von Kolloidteilchen mittels Röntgenstrahlen. *Nachrichten von der Gesellschaft der Wissenschaften* 98–100 (1918).

68. Clausen, B. S., Topsae, H. & Frahm, R. Application of Combined X-Ray Diffraction and Absorption Techniques for in Situ Catalyst Characterization. *Adv. Catal.* **42,** 315–344 (1998).

69. Koningsberger, D. C. & Prins, R. X-ray absorption spectroscopy. *Chem. Anal.* **92,** 3397–3400 (1988).

70. Newton, M. A., Dent, A. J. & Evans, J. Bringing time resolution to EXAFS: recent developments and application to chemical systems. *Chem. Soc. Rev.* **31,** 83–95 (2002).

71. Bouguer, P. *Essai d'optique sur la gradation de la lumière*. (Claude Jombert, 1729).

72. Henke, B. L., Gullikson, E. M. & Davis, J. C. X-Ray Interactions: Photoabsorption, Scattering, Transmission, and Reflection at E = 50-30,000 eV, Z = 1-92. *At. Data Nucl. Data Tables* **54,** 181–342 (1993).

73. Hansel, C. M. *et al.* Secondary mineralization pathways induced by dissimilatory iron reduction of ferrihydrite under advective flow. *Geochim. Cosmochim. Acta* **67,** 2977–2992 (2003).

74. Mustre de Leon, J., Rehr, J., Zabinsky, S. & Albers, R. Ab initio curved-wave x-ray-absorption fine structure. *Phys. Rev. B* **44,** 4146–4156 (1991).

75. Smolentsev, G. & Soldatov, A. V. FitIt: New software to extract structural information on the basis of XANES fitting. *Comput. Mater. Sci.* **39,** 569–574 (2007).

76. Smolentsev, G. & Soldatov, A. Quantitative local structure refinement from XANES: multi-dimensional interpolation approach. *J. Synchrotron Radiat.* **13,** 19–29 (2006).

77. Lee, P., Citrin, P., Eisenberger, P. & Kincaid, B. Extended x-ray absorption fine structure—its strengths and limitations as a structural tool. *Rev. Mod. Phys.* **53,** 769–806 (1981).

78. Sayers, D., Stern, E. & Lytle, F. New Technique for Investigating Noncrystalline Structures: Fourier Analysis of the Extended X-Ray—Absorption Fine Structure. *Phys. Rev. Lett.* **27,** 1204–1207 (1971).

79. Teo, B.-K. & Lee, P. A. Ab initio calculations of amplitude and phase functions for extended x-ray absorption fine structure spectroscopy. *J. Am. Chem. Soc.* **101,** 2815–2832 (1979).

80. Newville, M. IFEFFIT: interactive XAFS analysis and FEFF fitting. *J. Synchrotron Radiat.* **8,** 322–324 (2001).

81. Zabinsky, S., Rehr, J., Ankudinov, A., Albers, R. & Eller, M. Multiple-scattering calculations of X-ray absorption spectra. *Phys. Rev. B* **52,** 2995–3009 (1995).

82. Ravel, B. & Newville, M. ATHENA, ARTEMIS, HEPHAESTUS: data analysis for X-ray absorption spectroscopy using IFEFFIT. *J. Synchrotron Radiat.* **12,** 537–41 (2005).

83. Bergerhoff, G., Hundt, R., Sievers, R. & Brown, I. D. The inorganic crystal structure data base. *J. Chem. Inf. Model.* **23,** 66–69 (1983).

84. Newville, M., Ravel, B. & Haskel, D. Analysis of multiple-scattering XAFS data using theoretical standards. *Phys. B Condens. …* **209,** 154–156 (1995).

85. Stern, E. Number of relevant independent points in x-ray-absorption fine-structure spectra. *Phys. Rev. B* **48,** 9825–9827 (1993).

86. Li, G., Bridges, F. & Booth, C. X-ray-absorption fine-structure standards: A comparison of experiment and theory. *Phys. Rev. B* **52,** 6332–6348 (1995).

87. Rabe, S., Nachtegaal, M., Ulrich, T. & Vogel, F. Corrigendum: Towards Understanding the Catalytic Reforming of Biomass in Supercritical Water. *Angew. Chemie (International Ed.)* **51,** 2533–2533 (2012).

88. Colt, J. *Dissolved Gas Concentration in Water*. (Elsevier B.V., 2012).

89. Dreher, M., De Boni, E., Nachtegaal, M., Wambach, J. & Vogel, F. Design of a continuous-flow reactor for in situ x-ray absorption spectroscopy of solids in supercritical fluids. *Rev. Sci. Instrum.* **83,** 054101 (2012).

90. Koningsberger, D. C. & Prins, R. *X-Ray Absorption: Principles, Applications, Techniques of EXAFS, SEXAFS and XANES*. (Wiley Interscience, 1988).

91. Jensen, H. & Bremholm, M. In Situ High Energy Synchrotron Radiation Study of Sol–Gel Nanoparticle Formation in Supercritical Fluids. *Angew. Chemie (International Ed.)* **46,** 1113–1116 (2007).

92. Grunwaldt, J. & Baiker, A. Time Resolved and Operando XAS Studies on Heterogeneous Catalysts—From the Gas Phase Towards Reactions in Supercritical Fluids. *AIP Conf. Proc.* 577–582 (2007).

93. Kawai, T. *et al.* Design of a high-temperature and high-pressure liquid flow cell for X-ray absorption fine structure measurements under catalytic reaction conditions. *Rev. Sci. Instrum.* **79,** 014101 (2008).

94. Mayanovic, R. & Yan, H. In Situ X-ray Absorption Spectroscopic Study of the Adsorption of Ni2+ on Fe3O4 Nanoparticles in Supercritical Aqueous Fluids. *J. Phys. Chem. C* **116,** 2218–2225 (2012).

95. Yan, H., Mayanovic, R. A., Anderson, A. J. & Meredith, P. R. An in situ X-ray spectroscopic study of Mo6+ speciation in supercritical aqueous solutions. *Nucl. Instruments Methods Phys. Res. Sect. A Accel. Spectrometers, Detect. Assoc. Equip.* **649,** 207–209 (2011).

96. Seward, T. M., Henderson, C. M. B., Charnock, J. M. & Dobson, B. R. An X-ray absorption (EXAFS) spectroscopic study of aquated Ag+ in hydrothermal solutions to 350°C. *Geochim. Cosmochim. Acta* **60,** 2273–2282 (1996).

97. Testemale, D., Argoud, R., Geaymond, O. & Hazemann, J.-L. High pressure/high temperature cell for x-ray absorption and scattering techniques. *Rev. Sci. Instrum.* **76,** 043905 (2005).

98. Ranieri, V. *et al.* In Situ X-ray Absorption Spectroscopy Study of Si1–x Ge x O2 Dissolution and Germanium Aqueous Speciation under Hydrothermal Conditions. *Inorg. Chem.* **51,** 414 – 419 (2012).

99. Testemale, D., Brugger, J., Liu, W., Etschmann, B. & Hazemann, J.-L. In-situ X-ray absorption study of Iron(II) speciation in brines up to supercritical conditions. *Chem. Geol.* **264,** 295–310 (2009).

100. Testemale, D., Pokrovski, G. S. & Hazemann, J.-L. Speciation of As(III) and As(V) in hydrothermal fluids by in situ X-ray absorption spectroscopy. *Eur. J. Mineral.* **23,** 379–390 (2011).

101. Boukis, N., Claussen, N., Ebert, K., Janssen, R. & Schacht, M. Corrosion screening tests of high-performance ceramics in supercritical water containing oxygen and hydrochloric acid. *J. Eur. Ceram. Soc.* **17,** 71–76 (1997).

102. Kritzer, P., Boukis, N. & Dinjus, E. Review of the Corrosion of Nickel-Based Alloys and Stainless Steels in Strongly Oxidizing Pressurized High-Temperature Solutions at Subcritical and Supercritical Temperatures. *Corrosion* **56,** 1093–1104 (2012).

103. Schacht, M., Boukis, N. & Dinjus, E. Corrosion of alumina ceramics in acidic aqueous solutions at high temperatures and pressures. *J. Mater. Sci.* **5,** 6251–6258 (2000).

104. *CRC materials science and engineering handbook*. (CRC Press LLC, 2001).

105. Bremholm, M., Jensen, H., Iversen, S. B. & Iversen, B. B. Reactor design for in situ X-ray scattering studies of nanoparticle formation in supercritical water syntheses. *J. Supercrit. Fluids* **44,** 385–390 (2008).

106. Mussler, B. H. *et al.* Advanced materials & powders. *Am. Ceram. Soc. Bull.* **79,** 45 (2000).

107. Requirements concerning pipes and pressure vessels. *Int. Assoc. Classif. Soc.* (2012). at <http://www.iacs.org.uk/document/public/publications/unified_requirements/pdf/ur_p_pdf157.pdf>

108. Peterson, A. *et al.* Evidence of Scrambling over Ruthenium-based Catalysts in Supercritical-Water Gasification. *ChemCatChem* **4,** 1185–1189 (2012).

109. Wang, S. *et al.* Universal transition state scaling relations for (de)hydrogenation over transition metals. *Phys. Chem. Chem. Phys.* **13,** 20760–20765 (2011).

110. Hoffmann, M. & Conradi, M. Are there hydrogen bonds in supercritical water? *J. Am. Chem. Soc.* **119,** 3811–3817 (1997).

111. Walrafen, G. E., Yang, W.-H. & Chu, Y. C. Raman Spectra from Saturated Water Vapor to the Supercritical Fluid. *J. Phys. Chem. B* **103,** 1332–1338 (1999).

112. Bröll, D. *et al.* Chemistry in Supercritical Water. *Angew. Chemie (International Ed.)* **38,** 2998–3014 (1999).

113. Marcus, Y. Supercritical water: relationships of certain measured properties to the extent of hydrogen bonding obtained from a semi-empirical model. *Phys. Chem. Chem. Phys.* **2,** 1465–1472 (2000).

114. Schissler, D., Thompson, S. & Turkevich, J. Behaviour of paraffin hydrocarbons on electron impact. Synthesis and mass spectra of some deuterated paraffin hydrocarbons. *Discuss. Faraday Soc.* **10,** 46–53 (1951).

115. Jones, G. *et al.* First principles calculations and experimental insight into methane steam reforming over transition metal catalysts. *J. Catal.* **259,** 147–160 (2008).

116. Waldner, M. H. & Vogel, F. Renewable Production of Methane from Woody Biomass by Catalytic Hydrothermal Gasification. *Ind. Eng. Chem. Res.* **44,** 4543–4551 (2005).

117. Dreher, M. *et al.* Catalysis in supercritical water: Pathway of the methanation reaction and sulfur poisoning over a Ru/C catalyst during the reforming of biomolecules. *J. Catal.* **301,** 38–45 (2013).

118. Clendenen, R. & Drickamer, H. The effect of pressure on the volume and lattice parameters of ruthenium and iron. *J. Phys. Chem. Solids* **25,** 865–868 (1964).

119. Lutz, H. D., Müller, B., Schmidt, T. & Stingl, T. Structure refinement of pyrite-type ruthenium disulfide, RuS2, and ruthenium diselenide, RuSe2. *Acta Crystallogr. Sect. C Cryst. Struct. Commun.* **46,** 2003–2005 (1990).

120. Dacapo is a total energy DFT calculator that is freely available from the Department of Physics at the Technical University of Denmark. at <https://wiki.fysik.dtu.dk/dacapo>

121. ASE is an open-source code that is freely available from the Department of Physics at the Technical University of Denmark. at <https://wiki.fysik.dtu.dk/ase>

122. Hammer, B., Hansen, L. & Nørskov, J. Improved adsorption energetics within density-functional theory using revised Perdew-Burke-Ernzerhof functionals. *Phys. Rev. B* **59,** 7413–7421 (1999).

123. Broyden, C. G. The Convergence of Single-Rank Quasi-Newton Methods. *Math. Comput.* **24,** 365 (1970).

124. Koningsberger, D. C., Mojet, B. L., Dorssen, G. E. & Ramaker, D. E. XAFS spectroscopy; fundamental principles and data analysis. *Top. Catal.* **10,** 143–155 (2000).

125. Greegor, R. & Lytle, F. Morphology of supported metal clusters: Determination by EXAFS and chemisorption. *J. Catal.* **63,** 476–486 (1980).

126. Frenkel, A. I., Yevick, A., Cooper, C. & Vasic, R. Modeling the structure and composition of nanoparticles by extended X-ray absorption fine-structure spectroscopy. *Annu. Rev. Anal. Chem. (Palo Alto. Calif).* **4,** 23–39 (2011).

127. Lu, P.-J., Chen, T.-S. & Chern, J.-M. Reaction network and kinetic analysis of ethanol steam reforming over a Ru/Al2O3 catalyst. *Catal. Today* **174,** 17–24 (2011).

128. Almkvist, G., Boye, K. & Persson, I. K-edge XANES analysis of sulfur compounds: an investigation of the relative intensities using internal calibration. *J. Synchrotron Radiat.* **17,** 683–688 (2010).

129. Vairavamurthy, A. Using X-ray absorption to probe sulfur oxidation states in complex molecules. *Spectrochim. Acta Part A Mol. Biomol. Spectrosc.* **54,** 2009–2017 (1998).

130. Struis, R. P. W. J. *et al.* Sulphur poisoning of Ni catalysts in the SNG production from biomass: A TPO/XPS/XAS study. *Appl. Catal. A Gen.* **362,** 121–128 (2009).

131. Koningsberger, D. & Miller, J. The Origin of Sulfur Tolerance in Supported Platinum Catalysts: The Relationship between Structural and Catalytic Properties in Acidic and Alkaline Pt/LTL. *J. Catal.* **162,** 209–219 (1996).

132. Vendelbo, S. B., Johansson, M., Nielsen, J. H. & Chorkendorff, I. Is the methanation reaction over Ru single crystals structure dependent? *Phys. Chem. Chem. Phys.* **13,** 4486–93 (2011).

133. Van Hardeveld, R. & van Montfoort, A. The influence of crystallite size on the adsorption of molecular nitrogen on nickel, palladium and platinum: An infrared and electron-microscopic study. *Surf. Sci.* **4,** 396 (1966).

134. García-García, F. R., Guerrero-Ruiz, a. & Rodríguez-Ramos, I. Role of B5-Type Sites in Ru Catalysts used for the NH3 Decomposition Reaction. *Top. Catal.* **52,** 758–764 (2009).

135. McCollom, T. M. & Seewald, J. S. Experimental study of the hydrothermal reactivity of organic acids and acid anions: II. Acetic acid, acetate, and valeric acid. *Geochim. Cosmochim. Acta* **67,** 3645–3664 (2003).

136. Bartholomew, C. Carbon deposition in steam reforming and methanation. *Catal. Rev. Sci. Eng.* **24,** 67–112 (1982).

137. Kruse, W. & Wright, L. Regeneration of supported ruthenium catalyst. *US Pat. 4,072,628* (1978).

138. Rueter, M. Acetone hydrogenation using a supported ruthenium catalyst. *US Pat. 5,495,055* (1996).

139. Besson, M. & Gallezot, P. Deactivation of metal catalysts in liquid phase organic reactions. *Catal. Today* **81,** 547–559 (2003).

140. De Vlieger, D. J. M., Mojet, B. L., Lefferts, L. & Seshan, K. Aqueous Phase Reforming of ethylene glycol – Role of intermediates in catalyst performance. *J. Catal.* **292,** 239–245 (2012).

141. Müller, J. B. & Vogel, F. Tar and coke formation during hydrothermal processing of glycerol and glucose. Influence of temperature, residence time and feed concentration. *J. Supercrit. Fluids* **70,** 126–136 (2012).

142. Zöhrer, H. & Vogel, F. Hydrothermal catalytic gasification of fermentation residues from a biogas plant. *Biomass and Bioenergy* **53,** 138–148 (2013).

143. de Vlieger, D. J. M., Thakur, D. B., Lefferts, L. & Seshan, K. Carbon Nanotubes: A Promising Catalyst Support Material for Supercritical Water Gasification of Biomass Waste. *ChemCatChem* **4,** 2068–2074 (2012).

144. Bolzan, A. A., Fong, C., Kennedy, B. J. & Howard, C. J. Structural Studies of Rutile-Type Metal Dioxides. *Acta Crystallogr. Sect. B* **53,** 373–380 (1997).

145. Sun, Z. *et al.* Fabrication of Ruthenium-Carbon Nanotube Nanocomposites in Supercritical Water. *Adv. Mater.* **17,** 928–932 (2005).

146. Hoffmann, M. Kinetics and mechanism of oxidation of hydrogen sulfide by hydrogen peroxide in acidic solution. *Environ. Sci. Technol.* **11,** 61–66 (1977).

147. Joo, S. H. *et al.* Size effect of ruthenium nanoparticles in catalytic carbon monoxide oxidation. *Nano Lett.* **10,** 2709–2713 (2010).

148. Abrevaya, H., Cohn, M., Targos, W. & Robota, H. Structure sensitive reactions over supported ruthenium catalysts during Fischer-Tropsch synthesis. *Catal. Letters* **7,** 183–196 (1990).

149. He, Y. B., Knapp, M., Lundgren, E. & Over, H. Ru(0001) model catalyst under oxidizing and reducing reaction conditions: in-situ high-pressure surface X-ray diffraction study. *J. Phys. Chem. B* **109,** 21825–30 (2005).

150. Grasselli, R. K. & Sleight, A. W. *Structure-Activity and Selectivity Relationships in Heterogeneous Catalysis*. (Elsevier B.V., 1991).

151. Calvin, S. *et al.* Determination of crystallite size in a magnetic nanocomposite using extended x-ray absorption fine structure. *J. Appl. Phys.* **94,** 778 (2003).

152. Forzatti, P. & Lietti, L. Catalyst deactivation. *Catal. Today* **52,** 165–181 (1999).

153. Absi-Halabi, M., Stanislaus, a. & Trimm, D. L. Coke formation on catalysts during the hydroprocessing of heavy oils. *Appl. Catal.* **72,** 193–215 (1991).

154. Karayıldırım, T., Sınağ, a. & Kruse, a. Char and Coke Formation as Unwanted Side Reaction of the Hydrothermal Biomass Gasification. *Chem. Eng. Technol.* **31,** 1561–1568 (2008).

155. Guisnet, M. & Magnoux, P. Organic chemistry of coke formation. *Appl. Catal. A Gen.* **212,** 83–96 (2001).

156. Coll, R., Salvado, J., Farriol, X. & Montané, D. Steam reforming model compounds of biomass gasification tars: conversion at different operating conditions and tendency towards coke formation. *Fuel Process. Technol.* **74,** 19–31 (2001).

157. Lown, D., Thirsk, H. & Wynne-Jones, L. Temperature and pressure dependence of the volume of ionization of acetic acid in water from 25 to 225 °C and 1 to 3000 bars. *Trans. Faraday Soc.* **66,** 51–73 (1970).

158. Trimm, D. The regeneration or disposal of deactivated heterogeneous catalysts. *Appl. Catal. A Gen.* **212,** 153–160 (2001).

159. Leconte, M. An approach to the mechanisms of C-C bond formation and cleavage on metal surfaces using model elementary reaction steps of organometallic chemistry. *J. Mol. Catal.* **86,** 205–220 (1994).

160. Zaera, F. An Organometallic Guide to the Chemistry of Hydrocarbon Moieties on Transition Metal Surfaces. *Chem. Rev.* **95,** 2651–2693 (1995).

161. Candy, J., Copéret, C. & Basset, J. Analogy between Surface and Molecular Organometallic Chemistry. *Top. Organomet. Chem.* **16,** 151–210 (2005).

162. Leconte, M., Theolier, A. & Basset, J. Catalytic homologation of olefins to higher and lower olefins: a metathesis related reaction. *J. Mol. Catal.* **28,** 217–231 (1985).

163. Cooke, M., Forrow, N. J. & Knox, S. a. R. Generation of hydrocarbons from oligo-methylene chains linking two metal centres. *J. Organomet. Chem.* **222,** c21–c24 (1981).

164. Cooke, M., Forrow, N. & Knox, S. chemistry of dinuclear metal centres. Part 5. Generation of hydrocarbons from methylene chains linking two metal centres. Evidence for a dimetallacycle intermediate. *J. Chem. Soc., Dalt. Trans.* 2435 (1983).

165. Rodriguez, E., Leconte, M., Basset, J. M., Tanaka, K. & Tanaka, K.-I. Hydrogenolysis and Homologation of Linear and Branched Pentenes on Ru/Si02 Catalysts: Implication in the Mechanism of C-C Bond Formation and Cleavage on Metal Surfaces. *J. Am. Chem. Soc.* **110,** 275–278 (1988).

166. Liberatori, J. W. C., Ribeiro, R. U., Zanchet, D., Noronha, F. B. & Bueno, J. M. C. Steam reforming of ethanol on supported nickel catalysts. *Appl. Catal. A Gen.* **327,** 197–204 (2007).

167. Yee, A., Morrison, S. J. & Idriss, H. A Study of the Reactions of Ethanol on CeO2 and Pd/CeO2 by Steady State Reactions , Temperature Programmed Desorption , and In Situ FT-IR. *J. Catal.* **186,** 279–295 (1999).

168. Yee, A., Morrison, S. J. & Idriss, H. A Study of Ethanol Reactions over Pt/CeO2 by Temperature-Programmed Desorption and in Situ FT-IR Spectroscopy: Evidence of Benzene Formation. *J. Catal.* **191,** 30–45 (2000).

169. Cortright, R. & Dumesic, J. Microcalorimetric, spectroscopic, and kinetic studies of silica supported Pt and Pt/Sn catalysts for isobutane dehydrogenation. *J. Catal.* **148,** 771–778 (1994).

170. Humblot, F., Candy, J. P., Peltier, F. Le, Didillon, B. & Basset, J. M. Surface Organometallic Chemistry on Metals : Selective Dehydrogenation of Isobutane into Isobutene on Bimetallic Catalysts Prepared by Reaction of Tetra n-Butyltin on Silica-Supported Platinum Catalyst. *J. Catal.* **179,** 459–468 (1998).

171. Heise, W. & Tatarchuk, B. Thiophene adsorption on clean and sulfur precovered Ru (0001). *Surf. Sci.* **207,** 297–322 (1989).

172. Toulhoat, H., Raybaud, P., Kasztelan, S., Kresse, G. & Hafner, J. Transition metals to sulfur binding energies relationship to catalytic activities in HDS: back to Sabatier with first principle calculations. *Catal. Today* **50,** 629–636 (1999).

173. Nørskov, J. K., Bligaard, T., Rossmeisl, J. & Christensen, C. H. Towards the computational design of solid catalysts. *Nat. Chem.* **1,** 37–46 (2009).

Appendix

List of experiments and experimental parameters

Legend:

B-x	→ *batch experiment*
C-x	→ *experiment in continuous mode in stainless steel reactor*
Ci-x	→ *experiment in continuous mode in AlN in situ XAS reactor*
Ru/C	→ *commercial 2 wt% Ru on coconut carbon catalyst (BASF, Germany)*
Ru/CNF	→ *18 wt% Ru deposited on carbon nanofibers (prepared in-house)*
TOC	→ *total organic carbon content*
WHSV	→ *weight hourly space velocity*
c-t-g	→ *carbon to gas*
AC	→ *activated carbon*
EtOH	→ *ethanol*
AcOH	→ *acetic acid*
DMSO	→ *dimethyl sulfoxide*

Chapter 3

Figure 3.4	experiment C-1

Chapter 4

Figure 4.12	experiment Ci-1

Chapter 5

Figure 5.3	experiments B-1 to B-3

Chapter 6

Figure 6.1	experiment Ci-2
Table 6.2	experiments C-2 to C-4
Figure 6.4	experiment C-5
Figure 6.7/Table 6.3	experiment Ci-3
Figure 6.8	experiments B-4 to B-10
Figure 6.9	experiments B-11 to B-14

Chapter 7

Figure 7.1	experiment Ci-3
Figure 7.3	experiments C-6 to C-10
Figure 7.4	experiments C-11 to C-12
Figure 7.5	experiment Ci-4
Table 7.2	experiments C-13 to C-18
Figure 7.6	experiment C-19
Figure 7.7	experiments C-20 to C-21
Figure 7.9	experiment C-22
Figure 7.12	experiment C-23
Figure 7.18	experiment C-24

Chapter 3

Figure 3.4

# of exp.	catalyst	feed	TOC_{feed} [ppm]	flow rate [ml/min]	temp. [°C]	pressure [Mpa]	WHSV [$mol/mol_{Ru}·h$]	c-t-g conversion
C-1	Ru/C; 200 mg	4.8% EtOH in H_2O	25'040	0.5	400	25	796	full

Chapter 4

Figure 4.12

# of exp.	catalyst	feed	TOC_{feed} [ppm]	flow rate [ml/min]	temp. [°C]	pressure [Mpa]	WHSV [$mol/mol_{Ru}·h$]	c-t-g conversion
Ci-1	Ru/C; 150 mg	7.5% EtOH in H_2O	39'130	0.5	25 - 400	24.5	1660	full

Chapter 5

Figure 5.3

# of exp.	catalyst	reactor volume [ml]	reactant 1	reactant 2	temp. [°C]	pressure [Mpa]	time [h]
B-1	Ru/C; 1040 mg	54	D_2O; 8.5 ml	CH_4; 4 Mpa	395	28.5	24
B-2	RuO_2; 150 mg AC; 1040 mg	54	D_2O; 8.5 ml	CH_4; 4 Mpa	395	28.5	24
B-3	blank	54	D_2O; 8.5 ml	CH_4; 4 Mpa	395	28.5	24

Chapter 6

Figure 6.1

# of exp.	catalyst	feed	TOC_{feed} [ppm]	flow rate [ml/min]	temp. [°C]	pressure [Mpa]	WHSV [$mol/mol_{Ru}·h$]	c-t-g conversion
Ci-2	Ru/C; 200 mg	7.5% EtOH in H_2O	39'130	0.5	25 - 400	24.5	1244	full

Table 6.2

# of exp.	catalyst	feed	TOC_{feed} [ppm]	flow rate [ml/min]	temp. [°C]	pressure [Mpa]	WHSV [$mol/mol_{Ru}·h$]	c-t-g conversion
C-2	Ru/C; 200 mg	7.5% EtOH in H_2O *(+ 200 ppm DMSO)*	39'130	0.5	400	24.5	1244	full *(29.8%)*
C-3	Ru/C; 200 mg	7.0% acetaldehyde in H_2O *(+ 200 ppm DMSO)*	38'180	0.5	400	24.5	1214	full *(2.6%)*
C-4	Ru/C; 200 mg	10.4% MeOH in H_2O	39'000	0.5	400	24.5	2480	full

Figure 6.4

# of exp.	catalyst	feed	TOC_{feed} [ppm]	flow rate [ml/min]	temp. [°C]	pressure [Mpa]	WHSV [mol/mol_{Ru}·h]	c-t-g conversion
C-5	Ru/C; 200 mg	7.5% EtOH in H_2O *(+ 200 ppm DMSO)*	39'130	0.5	400	24.5	1244	full *(28.0%)*

Figure 6.7 and Table 6.3

# of exp.	catalyst	feed	TOC_{feed} [ppm]	flow rate [ml/min]	temp. [°C]	pressure [Mpa]	WHSV [mol/mol_{Ru}·h]	c-t-g conversion
Ci-3	Ru/C; 200 mg	7.5% EtOH in D_2O *(+ 200 ppm DMSO)*	39'130	0.5	400	24.5	1244	full *(26.0%)*

Figure 6.8

# of exp.	catalyst	reactor volume [ml]	pressuri-sation	reactant 1	reactant 2	D/H	temp. °C	pressure MPa	time [min]
B-4	Ru/C; 1050 mg	54	N_2; 4.2 Mpa	D_2O; 5.0 ml	MeOH; 4.0 g	1	398	31.2	25
B-5	Ru/C; 1050 mg	54	N_2; 4.2 Mpa	D_2O; 7.9 ml	MeOH; 1.1 g	6	398	30.7	15
B-6	Ru/C; 1050 mg	54	N_2; 4.2 Mpa	D_2O; 8.3 ml	MeOH; 0.7 g	10	398	29.5	10
B-7	Ru/C; 1050 mg	54	N_2; 4.2 Mpa	D_2O; 8.6 ml	MeOH; 0.5 g	15.2	398	29.0	10
B-8	Ru/C; 1050 mg	54	N_2; 4.2 Mpa	D_2O; 8.8 ml	MeOH; 0.2 g	39	398	27.5	5
B-9	Ru/C; 1050 mg	54	N_2; 4.2 Mpa	D_2O; 8.88 ml	MeOH; 0.12 g	60	398	27.0	5
B-10	Ru/C; 1050 mg	54	N_2; 4.2 Mpa	D_2O; 8.91 ml	MeOH; 0.09 g	80	398	27.0	5

Figure 6.9

# of exp.	catalyst	reactor volume [ml]	pressuri-sation	reactant 1	reactant 2	temp. [°C]	pressure [Mpa]	time [min]
B-11	Ru/C; 1050 mg	54	Ar; 3.12 Mpa	H_2O; 9.5 ml	^{13}C EtOH; 0.5 g	398	31.2	6
B-12	Ru/C; 1050 mg	54	Ar; 3.10 Mpa	H_2O; 9.5 ml	^{13}C AcOH; 0.5 g	398	31.2	6
B-13	S-Ru/C; 1050 mg	54	Ar; 3.05 Mpa	H_2O; 9.5 ml	^{13}C EtOH; 0.5 g	398	30.5	20
B-14	S-Ru/C; 1050 mg	54	Ar; 3.05 Mpa	H_2O; 9.5 ml	^{13}C AcOH; 0.5 g	398	30.5	20

Chapter 7

Figure 7.1

# of exp.	catalyst	feed	TOC_{feed} [ppm]	flow rate [ml/min]	temp. [°C]	pressure [Mpa]	WHSV [mol/mol_{Ru}·h]	c-t-g conversion
Ci-3	Ru/C; 200 mg	7.5% EtOH in D_2O	39'130	0.5	400	24.5	1244	full
		7.5% EtOH in D_2O + 200 ppm DMSO	39'190	0.5	400	24.5	1244	26%
		3% H_2O_2 in D_2O; 15 ml	-	1	125	24.5	-	-
		7.5% EtOH in D_2O	39'130	0.5	400	24.5	1244	full

Figure 7.3

# of exp.	catalyst	feed	flow rate [ml/min]	time [min]	temp. [°C]	pressure [Mpa]
C-6	Ru/C; 200 mg	7.5% EtOH in H_2O	0.5	60	390	24.5
C-7	Ru/C; 200 mg	3% H_2O_2 in H_2O	0.5	20	125	24.5
C-8	Ru/C; 200 mg	3% H_2O_2 in H_2O	0.5	60	125	24.5
C-9	Ru/C; 200 mg	3% H_2O_2 in H_2O	0.5	120	125	24.5
C-10	Ru/C; 200 mg	3% H_2O_2 in H_2O	0.5	240	125	24.5

Figure 7.4

# of exp.	catalyst	feed	flow rate [ml/min]	time [min]	temp. [°C]	pressure [Mpa]
C-11	Ru/C; 200 mg	3% H_2O_2 in H_2O	0.5	240	75	24.5
		3% H_2O_2 in H_2O	0.5	20	75	24.5
C-12	Ru/C; 200 mg	H_2O	0.5	60	390	24.5
		3% H_2O_2 in H_2O	0.5	20	75	24.5

Figure 7.5

# of exp.	catalyst	feed	flow rate [ml/min]	temp. [°C]	pressure [Mpa]
Ci-4	Ru/C; 200 mg	3% H_2O_2 in H_2O	0.5	25-150	24.5

Table 7.2

# of exp.	catalyst	feed	time [min]	flow rate [ml/min]	TOC_{feed} [ppm]	temp. [°C]	pressure [Mpa]	WHSV [mol/mol$_{Ru}$·h]	c-t-g conversion
C-13	Ru/C; 200 mg	7.5% EtOH in H_2O	-	0.5	39'130	390	25	1244	full
C-14	Ru/C; 200 mg	7.5% EtOH in D_2O + 200 ppm DMSO	-	0.5	39'190	390	25	1244	29.8%
(C-13,14→) **C-15**	Ru/C; 200 mg	3% H_2O_2 in H_2O	20	0.5	-	125	25	-	-
		7.5% EtOH in H_2O	-	0.5	39'130	390	25	1244	full
(C-13,14→) **C-16**	Ru/C; 200 mg	3% H_2O_2 in H_2O	20	0.5	-	100	25	-	-
		H_2O	60	0.5	-	390	25	-	-
		3% H_2O_2 in H_2O	20	0.5	-	100	25	-	-
		7.5% EtOH in H_2O	-	0.5	39'130	390	25	1244	full
(C-13,14→) **C-17**	Ru/C; 200 mg	3% H_2O_2 in H_2O	40	0.5	-	100	25	-	-
		7.5% EtOH in H_2O	-	0.5	39'130	390	25	1244	81.8%
(C-13,14→) **C-18**	Ru/C; 200 mg	3% H_2O_2 in H_2O	20	0.5	-	75	25	-	-
		H_2O	60	0.5	-	390	25	-	-
		3% H_2O_2 in H_2O	20	0.5	-	75	25	-	-
		7.5% EtOH in H_2O	-	0.5	39'130	390	25	1244	full

Figure 7.6

# of exp.	catalyst	feed	time [min]	TOC_{feed} [ppm]	flow rate [ml/min]	temp. [°C]	pressure [Mpa]	WHSV [mol/mol$_{Ru}$·h]	c-t-g conversion
C-19	Ru/C; 200 mg	15% EtOH in H_2O	120	78'260	1	400	24.5	4975	79.5%
		15% EtOH in H_2O + 200 ppm DMSO	60	78'320	1	400	24.5	4975	9%
		3% H_2O_2 in H_2O	20	-	1	75	24.5	-	-
		15% EtOH in H_2O	70	78'260	1	400	24.5	4975	68%→42%
		3% H_2O_2 in H_2O	20	-	1	75	24.5	-	-
		15% EtOH in H_2O	90	78'260	1	400	24.5	4975	80.5%→47%

Figure 7.7

# of exp.	catalyst	feed	time [min]	TOC_{feed} [ppm]	flow rate [ml/min]	temp. [°C]	pressure [Mpa]	WHSV [mol/mol$_{Ru}$·h]	c-t-g conversion
C-20	Ru/C; 200 mg	15% EtOH in H_2O	45	78'260	1	390	25	4975	77.2%
		15% EtOH in H_2O + 200 ppm DMSO	60	78'320	1	390	25	4975	9%
		3% H_2O_2 in H_2O	20	-	1	75	25	-	-
		H_2O	60	-	1	390	25	-	-
		3% H_2O_2 in H_2O	20	-	1	75	25	-	-
		15% EtOH in H_2O	120	78'260	1	390	25	4975	66.2%→23.1%
C-21	Ru/C; 200 mg	15% EtOH in H_2O	30	78'260	1	390	25	4975	77.4%
		3% H_2O_2 in H_2O	20	-	1	75	25	-	-
		H_2O	60	-	1	390	25	-	-
		3% H_2O_2 in H_2O	20	-	1	75	25	-	-
		15% EtOH in H_2O	240	78'260	1	390	25	4975	93%→77.2%

Figure 7.9

# of exp.	catalyst	feed	time [min]	TOC_{feed} [ppm]	flow rate [ml/min]	temp. [°C]	pressure [Mpa]	WHSV [mol/mol_{Ru}·h]	c-t-g conversion
		20.6% AcOH in H_2O	360	82'400	1	390	25.2	5240	full→92%
		20.6% AcOH in H_2O	10	82'400	1	25→390	25.2	5240	-
		20.6% AcOH in H_2O	180	82'400	1	390	25.2	5240	62%→45%
C-22	Ru/C; 200 mg	H_2O	60	-	1	400	25.2	-	-
		20.6% AcOH in H_2O	60	82'400	1	390	25.2	5240	40%→30%
		3% H_2O_2 in H_2O	30	-	1	125	25.2	-	-
		20.6% AcOH in H_2O	60	82'400	1	390	25.2	5240	42%→29%

Figure 7.12

# of exp.	catalyst	feed	time [min]	TOC_{feed} [ppm]	flow rate [ml/min]	temp. [°C]	pressure [Mpa]	WHSV [mol/mol$_{Ru}$·h]	c-t-g conversion
		15% iPrOH in H_2O	60	90'000	1	395	25	3815	75%
		20% citric acid in H_2O	60	74'960	1	395	25	1590	32%→30%
C-23	Ru/C; 200 mg	15% iPrOH in H_2O	90	90'000	1	395	25	3815	8.5%
		H_2O	280	-	1	400	1	-	-
		15% iPrOH in H_2O	70	90'000	1	395	25	3815	24%→20%

Figure 7.18

# of exp.	catalyst	feed	time [min]	TOC_{feed} [ppm]	flow rate [ml/min]	temp. [°C]	pressure [Mpa]	WHSV [mol/mol$_{Ru}$·h]	c-t-g conversion
		15% EtOH in H_2O	20	78'260	1	395	25	1105	55%
C-24	Ru/CNF; 50 mg	20% citric acid in H_2O	30	74'960	1	395	25	705	29%
		15% EtOH in H_2O	40	78'260	1	395	25	1105	26%